

NAG1-1424

NOZZLE FLOW
WITH VIBRATIONAL NONEQUILIBRIUM

IN-34-CR
6856
p. 109

by

John Gary Landry

B.S., Lawrence Institute of Technology, 1988
B.S., Lawrence Technological University, 1989
M.A., University of Detroit, 1991

A Dissertation Submitted to the Faculty of Old Dominion University
in Partial Fulfillment of the Requirements for the Degree of

DOCTOR OF PHILOSOPHY
in
COMPUTATIONAL AND APPLIED MATHEMATICS

OLD DOMINION UNIVERSITY
December 1995

(NASA-CR-199948) NOZZLE FLOW WITH
VIBRATIONAL NONEQUILIBRIUM Ph.D.
Thesis (Old Dominion Univ.) 109 p
N96-16280
Unclas
G3/34 0086517

Approved by:

John H. Heinbockel
John H. Heinbockel (Director)

Willard E. Meador
Willard E. Meador, NASA

John Swetits
John Swetits, ODU

John Tweed
John Tweed, ODU

NOZZLE FLOW
WITH VIBRATIONAL NONEQUILIBRIUM

by

John Gary Landry


B.S., Lawrence Institute of Technology, 1988
B.S., Lawrence Technological University, 1989
M.A., University of Detroit, 1991

A Dissertation Submitted to the Faculty of Old Dominion University
in Partial Fulfillment of the Requirements for the Degree of

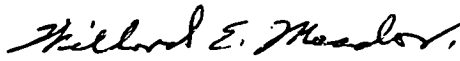
DOCTOR OF PHILOSOPHY
in
COMPUTATIONAL AND APPLIED MATHEMATICS

OLD DOMINION UNIVERSITY
December 1995

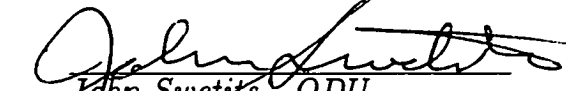
Approved by:



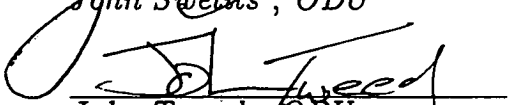
John H. Heinbockel (Director)



Willard E. Meador, NASA



John Swetits, ODU



John Tweed, ODU

ABSTRACT

NOZZLE FLOW WITH VIBRATIONAL NONEQUILIBRIUM

John Gary Landry

Old Dominion University, 1995

Director: Dr. John H. Heinbockel

Flow of nitrogen gas through a converging-diverging nozzle is simulated. The flow is modeled using the Navier-Stokes equations that have been modified for vibrational nonequilibrium. The energy equation is replaced by two equations. One equation accounts for energy effects due to the translational and rotational degrees of freedom, and the other accounts for the effects due to the vibrational degree of freedom. The energy equations are coupled by a relaxation time which measures the time required for the vibrational energy component to equilibrate with the translational and rotational energy components. An improved relaxation time is used in this thesis. The equations are solved numerically using the Steger-Warming flux vector splitting method and the Implicit MacCormack method. The results show that uniform flow is produced outside of the boundary layer. Nonequilibrium exists in both the converging and diverging nozzle sections. The boundary layer region is characterized by a marked increase in translational-rotational temperature. The vibrational temperature remains frozen downstream of the nozzle, except in the boundary layer.

ACKNOWLEDGEMENTS

This research was funded by NASA research grant NAG-1-1424. I would like to thank the researchers and contractors of the High Energy Science Branch at NASA Langley Research center for their support. Specifically, I would like to thank Ed Conway, Bill Meador, and Francis Badavi for their advice and assistance throughout the course of my research.

I would also like to thank the faculty of Old Dominion University for their support. I would like to thank John Tweed for allowing me the time to complete my research.

But mostly, I would like to thank John Heinbockel not only for his seemingly unlimited supply of assistance, but for much good advice on things technical and mundane.

CONTENTS

	Page
List of Figures	v
 Chapter	
1 Introduction	1
1.1 Background and Motivation	1
1.2 Current Objectives	5
 2 Governing Equations	7
2.1 Governing Equations in General Form	7
2.2 Governing Equations in Computational Form	17
2.3 Boundary Conditions	23
2.4 Initial Conditions	25
 3 Numerical Methods	30
3.1 Introduction	30
3.2 Beam and Warming Method	35
3.3 Steger-Warming Flux Vector Splitting Method	38
3.4 Implicit MacCormack Method	45
3.5 Numerical Implementation of Boundary Conditions	46
3.6 Conclusion	49

4 Numerical Results	50
4.1 Introduction.....	50
4.2 Validity of the Navier-Stokes Equations.....	50
4.3 Boundary Layer and Turbulence.....	54
4.4 Numerical Solutions.....	56
5 Conclusions	88
Bibliography	91
Appendix A: List of Symbols	94
Appendix B: Nozzle Design	97

LIST OF FIGURES

FIGURE	PAGE
2.1. Relaxation Times of Meador et al. and Millikan-White.....	16
2.2. Three-dimensional Physical Domain.....	18
2.3. a) Physical Domain: $0 \leq z \leq b, 0 \leq r \leq f(z)$	22
2.3. b) Computational Domain: $0 \leq x \leq 1, 0 \leq y \leq 1$	22
2.4. One-dimensional Model: Velocity vs Distance.....	27
2.5. One-dimensional Model: Temperature vs Distance.....	27
2.6. One-dimensional Model: Density vs Distance.....	28
2.7. One-dimensional Model: Pressure vs Distance.....	28
3.1. Generalized Grid Structure.....	32
3.2. Lengths for Irregular Grid Spacings.....	34
3.3. a) Pattern of Non-zero Elements of Matrix [C1].....	44
3.3. b) Pattern of Non-zero Elements of Matrix [C2].....	44
3.4. a) Pattern of Non-zero Elements of Leading Matrix in Predictor Step ...	47
3.4. b) Pattern of Non-zero Elements of Leading Matrix in Corrector Step ...	47
4.1. Maximum Mean Free Path for Nitrogen vs Distance from Inlet.....	52
4.2. Local Knudsen Number vs Distance from Inlet.....	53
4.3. Boundary Layer Width vs Distance from Inlet.....	55
4.4. Case One: Logarithm of Density Contours.....	63

4.5. Case One: Logarithm of Density Contours (throat region)	64
4.6. Case One: Pressure Contours	65
4.7. Case One: Pressure Contours (throat region)	66
4.8. Case One: Radial Velocity Contours	67
4.9. Case One: Radial Velocity Contours (throat region).....	68
4.10. Case One: Axial Velocity Contours	69
4.11. Case One: Axial Velocity Contours (throat region).....	70
4.12. Case One: Translational-rotational Temperature Contours	71
4.13. Case One: Translational-rotational Temperature Contours (throat region)	72
4.14. Case One: Vibrational Temperature Contours	73
4.15. Case One: Vibrational Temperature Contours (throat region).....	74
4.16. Case Two: Logarithm of Density Contours.....	75
4.17. Case Two: Pressure Contours	76
4.18. Case Two: Radial Velocity Contours.....	77
4.19. Case Two: Axial Velocity Contours.....	78
4.20. Case Two: Translational-rotational Temperature Contours.....	79
4.21. Case Two: Vibrational Temperature Contours (throat region).....	80
4.22. Case Three: Logarithm of Density Contours	81
4.23. Case Three: Pressure Contours	82
4.24. Case Three: Radial Velocity Contours (throat region).....	83
4.25. Case Three: Axial Velocity Contours	84

4.26. Case Three: Translational-rotational Temperature Contours	85
4.27. Case Three: Vibrational Temperature Contours	86
4.28. Centerline Equilibrium and Nonequilibrium Temperatures.....	87
B1. Nozzle Design	99

CHAPTER 1

INTRODUCTION

1.1 Background and Motivation

Wind tunnels are perhaps the most important tools in aerothermodynamic research. Their usefulness depends on their ability to produce uniform flow quality. Wind tunnel flow is usually represented by three-dimensional flow through a high expansion converging-diverging nozzle. The construction of wind tunnels is costly. For design purposes, there is a need for computer codes which can accurately predict flow behavior. The prime motivation in this study will be to determine the flow quality of pure nitrogen gas at low pressure through a converging diverging nozzle.

A useful property of these nozzles is the symmetry which exists in the azimuthal direction and allows the numerical problem to be reduced to two-dimensions. The fluid dynamics can be modeled using the Navier-Stokes equations. These equations can then be solved discretely over a finite grid. Still, with a wide variety of possible nozzle shapes, numerical methods, boundary conditions, and representations of thermal properties, this problem could be modeled in many ways. Unfortunately, these differences may also produce much different results. Hence there is a need for a sound physical modeling and good numerical technique in solving problems involving these flows.

Most physical flow models are based on the Navier-Stokes equations for fluid flow. The conservation of energy equation of the Navier-Stokes equations does not fully describe energy transfer for diatomic molecules, like nitrogen. The Navier-Stokes equations are used to model gases in thermal equilibrium. That is, energy fluctuations in the system redistribute equally among the degrees of freedom in the molecules. In an expanding nozzle, the temperature decreases rapidly as the gas travels past the throat. This drop is reflected in the drop in the energy associated with the translational and rotational degrees of freedom. The energy associated with the vibrational degree of freedom remains at a higher temperature that is closer to the stagnation temperature. Thus the system is in nonequilibrium. The vibrational component of the energy requires more time to lose its energy and fall to a temperature comparable to that associated with the translational and rotational energy. This finite time is the relaxation time. The 'vibrational relaxation' may be significant and therefore should be included in the physical development and the mathematical modeling. This is achieved by examining the energy based upon the translational and rotational degrees of freedom and the vibrational degree of freedom separately. The translational-rotational energy is assumed to be a function of a translational-rotational temperature. Likewise, the vibrational energy is assumed to be a function of a vibrational temperature. The Navier-Stokes equations are then modified to include an equation for the conservation of translational and rotational energy and an equation for the conservation of vibrational energy.

For equilibrium flow, the relaxation time is essentially zero and both temperatures are the same. Conversely, if the relaxation time is infinite, relaxation does not occur and the vibrational temperature remains 'frozen' at some vibrational temperature. For a wind tunnel the relaxation time is finite and non-zero, so the actual behavior lies somewhere between these two extremes [1]. The question then becomes, "What is the behavior of the vibrational temperature, and how does it affect the flow"?

Many investigators have included vibrational nonequilibrium in their models of nozzle flow, as in references [2], [3], and [4]. Both Gnoffo [2] and Göçken [4] modeled $N_2 - O_2$ gas mixtures in thermo-chemical nonequilibrium, in which they noted thermal equilibrium before the throat and that the vibrational temperature was 'frozen' downstream of the throat. For a test case with a very low stagnation pressure, Göçken noted vibrational freezing at the nozzle throat [4]. Also, the Mach number profiles displayed by Gnoffo showed reasonable uniformity [2]. Canupp et al. noted freezing at the throat for low pressure, pure nitrogen flow [3]. Their comparison between equilibrium and nonequilibrium models showed that Mach numbers increased slightly for the nonequilibrium modeling. The flow quality they achieved, however, was poor. This was assumed to be due to boundary layer behavior. Waves were created which reflected off the nozzle wall and affected the flow outside of the normal 'boundary-layer' region [3]. Thus, the actual effect of the vibrational nonequilibrium on the flow quality is not clear. In order to avoid this

problem, flow conditions should be chosen which minimize the size of the boundary layer.

These variations in results can be expected since they represent completely different models. Thus, their use in prediction is very limited. The only way to insure that the results will represent the behavior of a specific nozzle flow is to base one's model on that specific flow. To ensure meaningful results, a rigorous physical development is also necessary. Testing low pressure flow would best display the effects of vibrational nonequilibrium. The Reynolds number should also be low so that boundary layer effects are minimal.

Proper modeling of vibrational nonequilibrium requires an accurate estimation of the relaxation time. The relaxation times most often used are based on the Millikan-White model [5], which has been shown to be accurate in the temperature range of $2000 \leq T \leq 5000^\circ K$. Unfortunately, in high expansion nozzles, the temperatures downstream of the throat fall well below this temperature range. Therefore a model is needed which describes the vibration phenomenon for low temperatures. To this end, the model of Meador et al. [6] is used, which accounts for a greater number of collision possibilities and a rigorous handling of second order collision effects. This improvement in relaxation time should make the nonequilibrium modeling more meaningful.

Another problem in the literature is the use of the Mach number and sound speed in the description of the nonequilibrium flow. Mach number is calculated from the sound speed which is a function of the sound frequency, in nonequilibrium

gases. Since the sound speed is dispersive, this sound frequency is unknown. Some investigators use a frozen sound speed [7], which ignores the contribution of vibrational energy to the internal energy. This is only an approximation and therefore may undermine the integrity of the model. If the sound speed is only used to calculate Mach number contour plots to represent the results, this error may be small. However, if the sound speed is used in the numerical method [3] [7], the error may be significant. Also, since the behavior of the radial velocity component is dwarfed by the behavior of the axial velocity, contour plots of each velocity component would be more informative than a single Mach number plot.

A wide variety of numerical methods are in use in solving flow problems [8]. The choice of a method depends on: 1) the ease of numerically modeling the physical problem, 2) the stability of the method, and 3) the rate of convergence to a solution. Most of the methods currently in use differ only in the last point. Thus, any of these methods would be suitable unless one required a specific amount of efficiency. Then one would be required to choose a method with a sufficiently large Courant-Friedrichs-Lewy (CFL) number. Still, no numerical method is suitable unless it properly models the physical equations and boundary conditions.

1.2 Current Objectives

The current objective is to properly simulate nozzle flow using the Navier-Stokes equations with the modifications for vibrational nonequilibrium. The test cases simulate flow with a stagnation temperature of $3000 \text{ }^\circ K$ and a stagnation

pressure of 50 psi. The improved relaxation time is used to better model the nonequilibrium mechanism.

The two-dimensional equations are solved implicitly using both the implicit MacCormack method [8] and the Steger-Warming flux vector splitting method [9]. Boundary conditions are treated explicitly. The equations are solved discretely over an unequally spaced grid.

The contours of the primitive variables of each case are plotted and compared. These results were also compared to the results obtained under the assumption of equilibrium flow. Special attention is given to the quality of the flow and how it is affected by vibrational nonequilibrium.

CHAPTER 2

GOVERNING EQUATIONS

2.1 Governing Equations in General Form

A set of governing equations are needed to relate the set of primitive flow variables, $\{\rho, \vec{V}, T, P\}$, representing density, the velocity vector, temperature, and pressure, respectively. For continuum gas flow, the Navier-Stokes equations of motion are the basic mathematical model. A list of symbols appears in Appendix A.

Conservation of mass:

For a compressible gas the conservation of mass equation has the vector form:

$$\frac{D\rho}{Dt} + \rho \nabla \cdot \vec{V} = 0, \quad (2.1)$$

where $\frac{D}{Dt}$ is the material derivative such that,

$$\frac{D}{Dt} = \frac{\partial}{\partial t} + \vec{V} \cdot \nabla. \quad (2.2)$$

Conservation of momentum:

Each component of velocity, V_i , has a corresponding equation,

$$\rho \frac{DV_i}{Dt} = \sigma_{ij,j}, \quad (2.3)$$

where σ_{ij} is the stress tensor, satisfying

$$\sigma_{ij} = -P\delta_{ij} + \tau_{ij}. \quad (2.4)$$

The shear stress, τ_{ij} , is a function of velocity:

$$\tau_{ij} = \eta(V_{i,j} + V_{j,i}) + \lambda V_{k,k}\delta_{ij}, \quad (2.5)$$

where η and λ are the coefficients of viscosity and δ_{ij} is the Kronecker delta. The first coefficient of viscosity is calculated using Sutherland's formula. For N_2 ,

$$\eta = \frac{2.16 \times 10^{-8} g T^{\frac{3}{2}}}{T + 184}, \quad (2.6)$$

where g is the gravitational constant and T is in $^{\circ}R$ [10], and the second coefficient from the Stokes' hypothesis,

$$\lambda = -\frac{2}{3}\eta. \quad (2.7)$$

Conservation of Energy, one temperature:

The change in the total energy of a fluid in motion equals the sum of the changes in the internal energy, kinetic energy, work done, and heat from conduction and radiation. For the flow investigated, radiation effects are assumed to be small and are neglected. The internal energy, $e(T)$, is a function of temperature and

$$\frac{\partial e(T)}{\partial T} = C_v \quad (2.8)$$

where C_v is the specific heat at constant volume.

The first law of thermodynamics is used to obtain the equation:

$$\frac{D(\rho e)}{Dt} = -P\nabla \cdot \vec{V} + \nabla \cdot \vec{q} - \Phi, \quad (2.9)$$

where $-P\nabla \cdot \vec{V}$ represents the work done due to the velocity change. The second term, $\nabla \cdot \vec{q}$, is the heat loss due to convection with

$$\vec{q} = -K\nabla T \quad (2.10)$$

from Fourier's law. The coefficient K represents the coefficient of thermal conductivity of the gas and is assumed to be a function of temperature. The final term of equation (2.9) is the viscous dissipation function which has the tensor form

$$\Phi = \nabla(\tau_{ij}V_j) - \vec{V} \cdot \nabla(\tau_{ij}). \quad (2.11)$$

Conservation of Energy, two temperatures:

When vibrational relaxation occurs, the energy distribution is changed as the system returns to a state of equilibrium. In order to model this behavior, the energy generated from the molecules' vibrational degrees of freedom is treated separately from the energy generated from the translational and rotational degrees of freedom. Then, the total internal energy is written as

$$e = e_{rt} + e_v, \quad (2.12)$$

which represents the sum of the translational-rotational internal energy and the vibrational internal energy. The molecules are assumed to be linear harmonic oscillators and are excited to energy states, ϵ_i , such that

$$\epsilon_i = (i + \frac{1}{2})h\nu \quad (i = 0, 1, 2, \dots), \quad (2.13)$$

where h is Planck's constant and ν is the collision frequency. Each energy state is populated by a density of molecules, N_i . Due to the speed of the resonant V-V collisions, the populations are assumed to be Boltzmann distributions,

$$N_i = \frac{N e^{-\frac{\epsilon_i}{kT}}}{\sum_i e^{-\frac{\epsilon_i}{kT}}}, \quad (2.14)$$

where N is the total number of excited molecules. It is also assumed, that for each collision, the molecules can be excited only to the next energy state. The total vibrational energy per unit volume can be written as

$$\rho e_v = \sum_i \epsilon_i N_i. \quad (2.15)$$

The total rate of change in vibrational energy equals the rate of heat transfer due to vibration or

$$\frac{\partial}{\partial t} \int_v \sum_i N_i \epsilon_i dv + \int_s \sum_i N_i \epsilon_i \vec{V}_i \cdot d\vec{s} = \int_v \sum_i \frac{\partial N_i}{\partial t} \epsilon_i dv \quad (2.16)$$

where dv is an element of volume and $d\vec{s}$ is an element of surface area. By implementing the Gauss divergence theorem, the differential equation is obtained:

$$\frac{\partial}{\partial t} (\sum_i N_i \epsilon_i) + \sum_i \nabla \cdot (N_i \epsilon_i \vec{V}_i) = \sum_i \frac{\partial N_i}{\partial t} \epsilon_i, \quad (2.17)$$

where \vec{V}_i is the average velocity of the molecules in energy state ϵ_i . The diffusion velocity of a species, \vec{U}_i , is defined to relate the individual velocities and the mean velocity, such that $\vec{U}_i = \vec{V}_i - \vec{V}$. Substituting this into equation (2.17) yields

$$\frac{\partial}{\partial t} (\sum_i N_i \epsilon_i) + \nabla \cdot (\sum_i N_i \epsilon_i \vec{U}_i) + \nabla \cdot (\sum_i N_i \epsilon_i \vec{V}) = \sum_i \frac{\partial N_i}{\partial t} \epsilon_i. \quad (2.18)$$

Using equation (2.15), the vibrational energy equation becomes

$$\frac{\partial(\rho e_v)}{\partial t} + \nabla \cdot (\rho e_v \vec{V}) = -\nabla \cdot \left(\sum_i N_i \epsilon_i \vec{U}_i \right) + \sum_i \frac{\partial N_i}{\partial t} \epsilon_i. \quad (2.19)$$

The vibrational heat flux, \vec{q}_v , is defined by

$$\vec{q}_v = \sum_i N_i \epsilon_i \vec{U}_i, \quad (2.20)$$

and is substituted into equation (2.19) to give the result

$$\frac{\partial(\rho e_v)}{\partial t} + \nabla \cdot \rho e_v \vec{V} = \sum_i \frac{\partial N_i}{\partial t} \epsilon_i - \nabla \cdot \vec{q}_v. \quad (2.21)$$

By applying the continuity equation (2.1), equation (2.21) simplifies to

$$\rho \frac{D(e_v)}{Dt} = \sum_i \frac{\partial N_i}{\partial t} \epsilon_i - \nabla \cdot \vec{q}_v. \quad (2.22)$$

The sum, $\sum_i \frac{\partial N_i}{\partial t} \epsilon_i$, is the rate of change of the vibrational energy, $\frac{\partial(\rho e_v)}{\partial t}$, which can be defined as

$$\sum_i \epsilon_i \frac{\partial N_i}{\partial t} = \rho \left(\frac{e_v(T) - e_v(T_v)}{\tau} \right), \quad (2.23)$$

where T_v is the vibrational temperature associated with e_v , and T is the equilibrium temperature associated with e_{rt} [6]. When $T_v = T$, the system is considered to be in thermal equilibrium. The relaxation time, τ , represents the time required for excited molecules to reach equilibrium. As with the internal energies, the specific heat can be written as a sum

$$C_v = C_{vrt} + C_{vv}, \quad (2.24)$$

where C_{vrt} and C_{vv} are the specific heats at constant volume for the translational-rotational and vibrational degrees of freedom, respectively. For simplicity, define the quantity X such that

$$C_{vv}X = \frac{e_v(T) - e_v(T_v)}{\tau}. \quad (2.25)$$

Then the final form of the vibrational energy equation can be written as

$$\rho \frac{D(e_v)}{Dt} = \rho C_{vv}X - \nabla \cdot \vec{q}_v. \quad (2.26)$$

To obtain an equation for the translational-rotational energy using the vibrational energy equation, equation(2.26), the elements of the one-temperature energy equation, equation (2.9), are split into translational-rotational and vibrational components:

$$\rho \frac{D(e_{rt} + e_v)}{Dt} + P \nabla \cdot \vec{V} + \nabla \cdot (\vec{q}_{rt} + \vec{q}_v) - \Phi = 0. \quad (2.27)$$

Subtracting equation (2.26) from equation (2.27) yields the translational-rotational energy equation:

$$\rho \frac{D(e_{rt})}{Dt} + P \nabla \cdot \vec{V} + \nabla \cdot \vec{q}_{rt} + \rho C_{vv}X - \Phi = 0. \quad (2.28)$$

Each energy is related to its respective temperature by a separate specific heat. From the equipartition of energy principle, each degree of freedom contributes $\frac{1}{2}RT$ to the total energy [11]. Each diatomic molecule has three translational, two rotational, and one vibrational degree of freedom. Even for low temperatures, the translational and rotational modes are fully activated, so a good approximation to

the specific heat at constant volume, C_{vrt} , is $\frac{5}{2}R$, so that the translational-rotational energy has the form

$$e_{rt} = \frac{5}{2}RT, \quad (2.29)$$

where R is the ideal gas constant. Since the vibrational mode is not fully activated, the equipartition principle does not provide a good value for the vibrational specific heat, C_{vv} . Substituting equations (2.13) and (2.14) into the basic definition of vibrational energy, equation (2.15), yields

$$\rho e_v = \frac{Nh\nu \sum_i i e^{-\frac{(i+\frac{1}{2})h\nu}{kT_v}}}{\sum_j e^{-\frac{(j+\frac{1}{2})h\nu}{kT_v}}}. \quad (2.30)$$

This simplifies to

$$\rho e_v = \frac{Nh\nu \sum_i i e^{-\frac{ih\nu}{kT_v}}}{\sum_j e^{-\frac{jh\nu}{kT_v}}} + \frac{1}{2}Nh\nu. \quad (2.31)$$

This equation can be simplified by utilizing the sums

$$\sum_i i e^{-\frac{ih\nu}{kT_v}} = \frac{e^{-\frac{h\nu}{kT_v}}}{(1 - e^{-\frac{h\nu}{kT_v}})^2} \quad (2.32)$$

and

$$\sum_j e^{-\frac{jh\nu}{kT_v}} = \frac{1}{(1 - e^{-\frac{h\nu}{kT_v}})}. \quad (2.33)$$

Furthermore, a characteristic vibrational temperature, ϕ , is defined such that

$\phi = \frac{h\nu}{k}$. Thus, equation (2.31) becomes

$$\rho e_v = \frac{N\phi k e^{-\frac{\phi}{T_v}}}{(1 - e^{-\frac{\phi}{T_v}})} + \frac{1}{2}Nk\phi = \frac{N\phi k}{e^{\frac{\phi}{T_v}} - 1} + \frac{1}{2}Nk\phi. \quad (2.34)$$

Since $Nk = \rho R$,

$$e_v = \frac{R\phi}{e^{\frac{\phi}{T_v}} - 1} + \frac{1}{2}R\phi. \quad (2.35)$$

The specific heat at constant volume for the vibrational mode becomes

$$C_{vv} = \frac{\partial e_v}{\partial T_v} = R \left(\frac{\phi}{T_v} \right)^2 \frac{e^{\frac{\phi}{T_v}}}{(e^{\frac{\phi}{T_v}} - 1)^2}. \quad (2.36)$$

From equation (2.25), equation (2.35) and equation (2.36) the quantity X is found to be

$$X = \frac{T_v^2 (1 - e^{-\frac{\phi}{T_v}})}{\phi \tau (1 - e^{-\frac{\phi}{T}})} (e^{\phi(\frac{1}{T_v} - \frac{1}{T})} - 1). \quad (2.37)$$

Note that when the system is in equilibrium, $T_v = T$, and consequentially X equals zero.

The heat fluxes are functions of temperature having the form

$$q_{rt} = -K_{rt} \nabla T, \quad q_v = -K_v \nabla T_v, \quad (2.38)$$

where K_{rt} and K_v are the translational-rotational and vibrational thermal conductivities, respectively. The Prandtl number, Pr , is defined as $Pr = \frac{\eta(C_{vrt} + R)}{K_{rt}}$ so $K_{rt} = \frac{7}{2} \frac{R\eta}{Pr}$. For N_2 at $0^\circ C$, $Pr = 0.71$, so $K_{rt} = 4.93\eta R$ [12]. The vibrational heat flux is determined from equation (2.20). For a pure gas $N_i \vec{U}_i = -ND \nabla (\frac{N_i}{N})$, where D is the diffusion coefficient, or in this case, the self-diffusion coefficient. Then

$$\vec{q}_v = -ND \sum_i \epsilon_i \nabla \left(\frac{N_i}{N} \right) = -ND \nabla \left(\frac{1}{N} \sum_i N_i \epsilon_i \right) = -\rho D \nabla \left(\frac{1}{\rho} \sum_i N_i \epsilon_i \right). \quad (2.39)$$

Substituting equation (2.15) into equation (2.39),

$$\vec{q}_v = -\rho D \nabla e_v = -\rho D C_{vv} \nabla T. \quad (2.40)$$

The Schmidt number, Sc , is defined as $Sc = \frac{\eta}{\rho D}$, and for N_2 at $0^\circ C$, Sc equals 0.74, reference [12]. Thus, from equation (2.38),

$$K_v = \rho D C_{vv} = \frac{\eta}{Sc} C_{vv} = 1.35\eta C_{vv}. \quad (2.41)$$

The vibrational thermal conductivity is a function of both T and T_v since viscosity is a function of T and specific heat is a function of T_v .

For N_2 , the relaxation time is taken from Meador, Williams and Miner [6]:

$$P_{(atm)}\tau = \frac{3.2188 \times 10^{-12}}{I(T) \sinh(\frac{\phi}{2T})} \left(\frac{T}{\theta}\right)^{\frac{1}{2}} e^{-\frac{\xi}{T}} \quad (2.42)$$

where

$$\phi = 3395K, \theta = 3.2324 \times 10^7 K, \xi = 95.9K \quad (2.43)$$

represent characteristic temperatures, and

$$I(T) = \int_{\frac{\phi+2\xi}{2T}}^{\infty} \left(1 + \left(1 + \frac{Tx}{\xi}\right)^{\frac{1}{2}}\right)^{-\frac{1}{2}} (1 - e^{-2\zeta_-}) e^{-(x+\zeta_+-\zeta_-)} dx, \quad (2.44)$$

with

$$\zeta_{\pm} = \left(\frac{16\theta T x}{27\phi^2} \left(1 \pm \frac{\phi}{2Tx}\right)\right)^{\frac{1}{2}}. \quad (2.45)$$

Figure 2.1 shows the relaxation time τ derived from equation (2.42) as it compares to the relaxation time developed by Millikan-White [5].

Equation of State:

The final equation is simply the ideal gas law:

$$P = \rho RT. \quad (2.46)$$

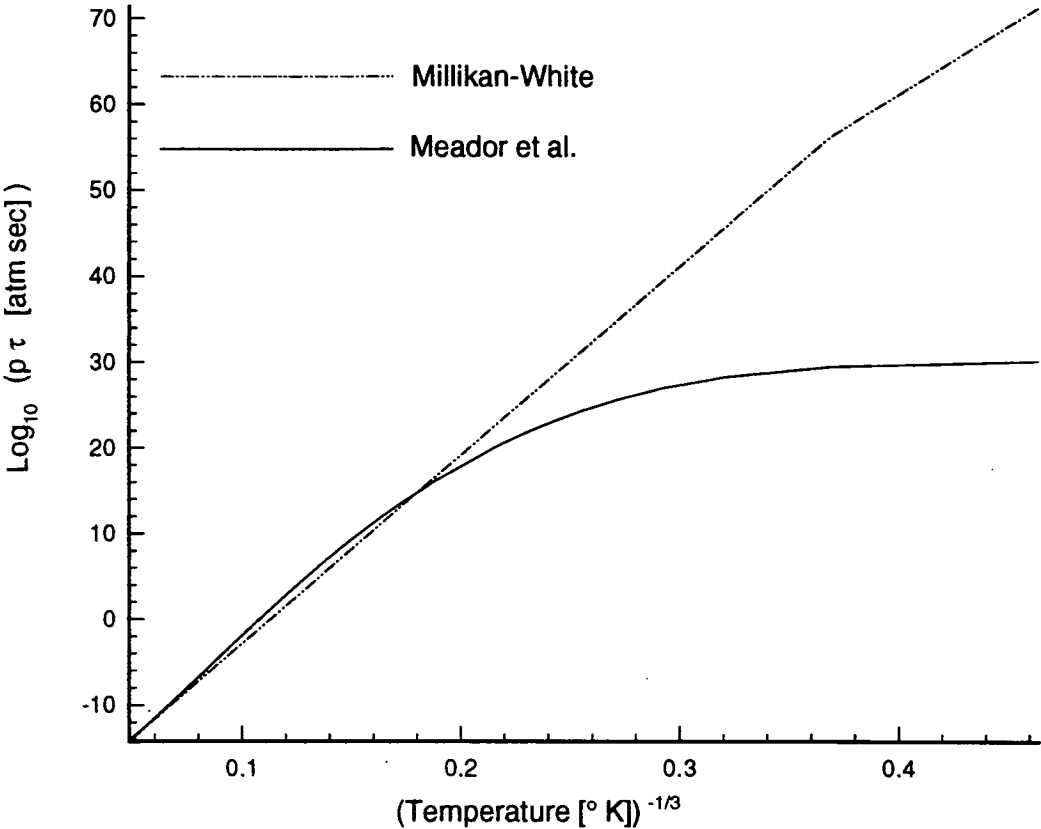


Figure 2.1. Relaxation Times of Meador et al. and Millikan-White

This equation does not always hold for gases at high pressures, but these departures from non-ideality are assumed to be negligible.

2.2 Governing Equations in Computational Form

The nozzle studied is defined in 3-dimensional cylindrical coordinates, (r, θ, z) [figure 2.2]. However, there exists a symmetry in the θ direction, which means that the variables do not change in the θ direction. Thus, the θ -component of velocity, V_θ , is assumed to be zero, and the momentum equation in the θ direction can be neglected. Furthermore, the derivatives with respect to θ in the remaining equations are zero and can be neglected. This reduces the system of equations to six, and the problem to two-dimensions, (r, z) .

Symmetry about the centerline (z -axis) allows the flow to be determined from a single half cross-section, where $0 \leq r \leq f(z)$ and $0 \leq z \leq b$. The function $f(z)$ describes the shape of the nozzle and b denotes the length of the nozzle. The nozzle shape is defined in appendix B.

To facilitate the numerical method, the each equation is written in the weak conservative form

$$\frac{\partial U_i}{\partial t} + \frac{1}{r} \frac{\partial(rF_i)}{\partial r} + \frac{\partial G_i}{\partial z} + \frac{1}{r} H_i = 0. \quad (2.47)$$

Equations (2.1), (2.3), (2.26), and (2.28) become

$$\frac{\partial \rho}{\partial t} + \frac{1}{r} \frac{\partial(r\rho V_r)}{\partial r} + \frac{\partial(\rho V_z)}{\partial z} = 0 \quad (2.48)$$

$$\frac{\partial(\rho V_r)}{\partial t} + \frac{1}{r} \frac{\partial}{\partial r}(r(\rho V_r^2 + P - \tau_{rr})) + \frac{\partial}{\partial z}(\rho V_r V_z - \tau_{rz}) - \frac{1}{r}(P + \tau_{\theta\theta}) = 0 \quad (2.49)$$

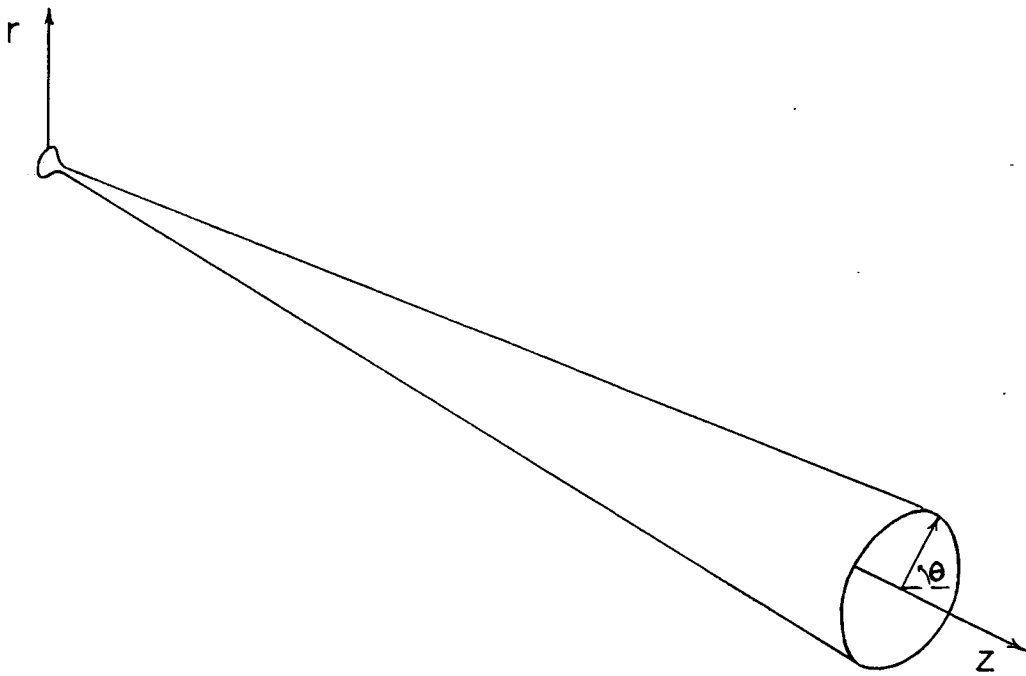


Figure 2.2. Three-dimensional Physical Domain.

$$\frac{\partial(\rho V_z)}{\partial t} + \frac{1}{r} \frac{\partial}{\partial r}(r(\rho V_r V_z - \tau_{rz})) + \frac{\partial}{\partial z}(\rho V_z^2 + P - \tau_{zz}) = 0 \quad (2.50)$$

$$\begin{aligned} & \frac{\partial}{\partial t}(\rho e_{rt} + \frac{\rho}{2}(V_r^2 + V_z^2)) + \frac{1}{r} \frac{\partial}{\partial r}(r((\rho e_{rt} + \frac{\rho}{2}(V_r^2 + V_z^2))V_r - V_z \tau_{rz} + q_{rtr})) + \\ & + \frac{\partial}{\partial z}((\rho e_{rt} + \frac{\rho}{2}(V_r^2 + V_z^2))V_z - V_r \tau_{rz} - V_z \tau_{zz} + q_{rtz}) + \rho C_{vv} X = 0 \end{aligned} \quad (2.51)$$

$$\frac{\partial(\rho e_v)}{\partial t} + \frac{1}{r} \frac{\partial}{\partial r}(r(\rho e_v V_r + q_{vr})) + \frac{\partial}{\partial z}(\rho e_v V_z + q_{vz}) - \rho C_{vv} X = 0. \quad (2.52)$$

The total translational-rotational energy, E_{rt} , is defined by

$$E_{rt} = \rho e_{rt} + \frac{\rho}{2}(V_r^2 + V_z^2), \quad (2.53)$$

and the total vibrational energy, E_v , by

$$E_v = \rho e_v. \quad (2.54)$$

The set of equations can be represented as a vector equation

$$\frac{\partial U}{\partial t} + \frac{1}{r} \frac{\partial(rF)}{\partial r} + \frac{\partial G}{\partial z} + \frac{1}{r} H = 0, \quad (2.55)$$

where U , F , G , and H are vectors. The vector $U = \text{col}(\rho, \rho V_r, \rho V_z, E_{rt}, E_v)$, is the set of conservative variables.

The equations are scaled by introducing the dimensionless variables defined by

$$\begin{aligned} r^* &= \frac{r}{\delta}, & \rho^* &= \frac{\rho}{\rho_0}, & e_{rt}^* &= \frac{e_{rt}}{V_0^2}, \\ z^* &= \frac{z}{L}, & V_r^* &= \frac{V_r}{\frac{V_0 \delta}{L}}, & e_v^* &= \frac{e_v}{V_0^2}, \\ t^* &= \frac{t}{\frac{L}{V_0}}, & V_z^* &= \frac{V_z}{V_0}, & P^* &= \frac{P}{\rho_0 V_0^2}, \\ & & T^* &= \frac{T}{T_0}, & \eta^* &= \frac{\eta}{\eta_0}. \end{aligned}$$

where δ and L are characteristic lengths, V_0 is the characteristic velocity, ρ_0 is the characteristic density, and T_0 is a characteristic temperature. The characteristic viscosity, η_0 , is the viscosity calculated at T_0 . The Reynolds number, Re , is defined as the combination $Re = \frac{\rho_0 V_0 L}{\eta_0}$. The nozzle domain becomes $0 \leq r^* \leq \frac{f(Lz^*)}{\delta}$ and $0 \leq z^* \leq \frac{b}{L}$. The system of equations has the final scaled conservative form

$$\frac{\partial U^*}{\partial t^*} + \frac{1}{r^*} \frac{\partial(r^* F^*)}{\partial r^*} + \frac{\partial G^*}{\partial z^*} + \frac{1}{r^*} H^* = 0, \quad (2.56)$$

where U^* , F^* , G^* , and H^* are the column vectors

$$U^* = \begin{bmatrix} \rho^* \\ \rho^* V_r^* \\ \rho^* V_z^* \\ E_{rt}^* \\ E_v^* \end{bmatrix} \quad (2.57)$$

$$F^* = \begin{bmatrix} \rho^* V_r^* \\ \rho^* V_r^* V_r^* + \frac{L^2}{\delta^2} P^* - \frac{L^2}{\delta^2} \frac{1}{Re} \tau_{rr}^* \\ \rho^* V_r^* V_z^* - \frac{L^2}{\delta^2} \frac{1}{Re} \tau_{rz}^* \\ (E_{rt}^* + P^*) V_r^* - V_r^* \frac{1}{Re} \tau_{rr}^* - \frac{L^2}{\delta^2} V_z^* \frac{1}{Re} \tau_{rz}^* + q_{rtr}^* \\ E_v^* V_r^* + q_{vr}^* \end{bmatrix} \quad (2.58)$$

$$G^* = \begin{bmatrix} \rho^* V_z^* \\ \rho^* V_r^* V_z^* - \frac{L^2}{\delta^2} \frac{1}{Re} \tau_{rz}^* \\ \rho^* V_z^* V_z^* + P^* - \frac{1}{Re} \tau_{zz}^* \\ (E_{rt}^* + P^*) V_z^* - V_r^* \frac{1}{Re} \tau_{rz}^* - V_z^* \frac{1}{Re} \tau_{zz}^* + q_{rtz}^* \\ E_v^* V_z^* + q_{vz}^* \end{bmatrix} \quad (2.59)$$

$$H^* = \begin{bmatrix} 0 \\ -\frac{L^2}{\delta^2} P^* + \frac{L^2}{\delta^2} \frac{1}{Re} \tau_{\theta\theta}^* \\ 0 \\ \frac{rL^* \rho^* C_{vv}^* X^*}{V_0^3} \\ -\frac{rL^* \rho^* C_{vv}^* X^*}{V_0^3} \end{bmatrix} \quad (2.60)$$

The scaled equation of state is

$$P^* = \rho^* RT^* \left(\frac{T_0}{V_0^2} \right). \quad (2.61)$$

Finally, the nozzle is mapped to the computational domain. By employing the change of variables,

$$x = \frac{z^*}{b/L}, \quad y = \frac{r^*}{f(Lz^*)/\delta}, \quad (2.62)$$

the nozzle is mapped to a square with domain $0 \leq x \leq 1$ and $0 \leq y \leq 1$, [figure 2.3]. The system of equations in equation (2.56) is converted to

$$\frac{\partial U}{\partial t^*} + \frac{\partial F}{\partial x} + \frac{\partial G}{\partial y} + H = 0 \quad (2.63)$$

by

$$F = \frac{L}{b} G^*, \quad G = \frac{\delta}{f(bx)} F^* - \frac{Lyf'(bx)}{f(bx)} G^*, \quad (2.64)$$

$$H = \frac{Lf'(bx)}{f(bx)} G^* + \frac{\delta}{yf(bx)} (F^* + H^*), \quad U = U^*.$$

When y approaches zero, $\frac{\delta}{yf(bx)}$ approaches infinity, hence the necessary limit,

$$\lim_{y \rightarrow 0} \frac{\delta}{yf(bx)} (F^* + H^*) = \left[\begin{array}{c} 0 \\ -\frac{L^2}{\delta^2} \frac{\delta^2 \eta}{\rho f^2 Re} \frac{\partial^2 (\rho V_r)}{\partial y^2} \\ -\frac{L^2}{\delta^2} \frac{\delta}{f Re} \frac{\partial (\tau_{rz})}{\partial y} \\ -\frac{L^2}{\delta^2} \frac{\delta V_x}{f Re} \frac{\partial (\tau_{rz})}{\partial y} - \frac{L^2}{\delta^2} \frac{K_{rt} q_0 \delta^2}{f^2} \frac{\partial^2 T}{\partial y^2} + \rho C_{vv} X \\ -\frac{L^2}{\delta^2} \frac{K_v q_0 \delta^2}{f^2} \frac{\partial^2 T_v}{\partial y^2} - \rho C_{vv} X \end{array} \right], \quad (2.65)$$

is obtained from L'Hospital's rule.

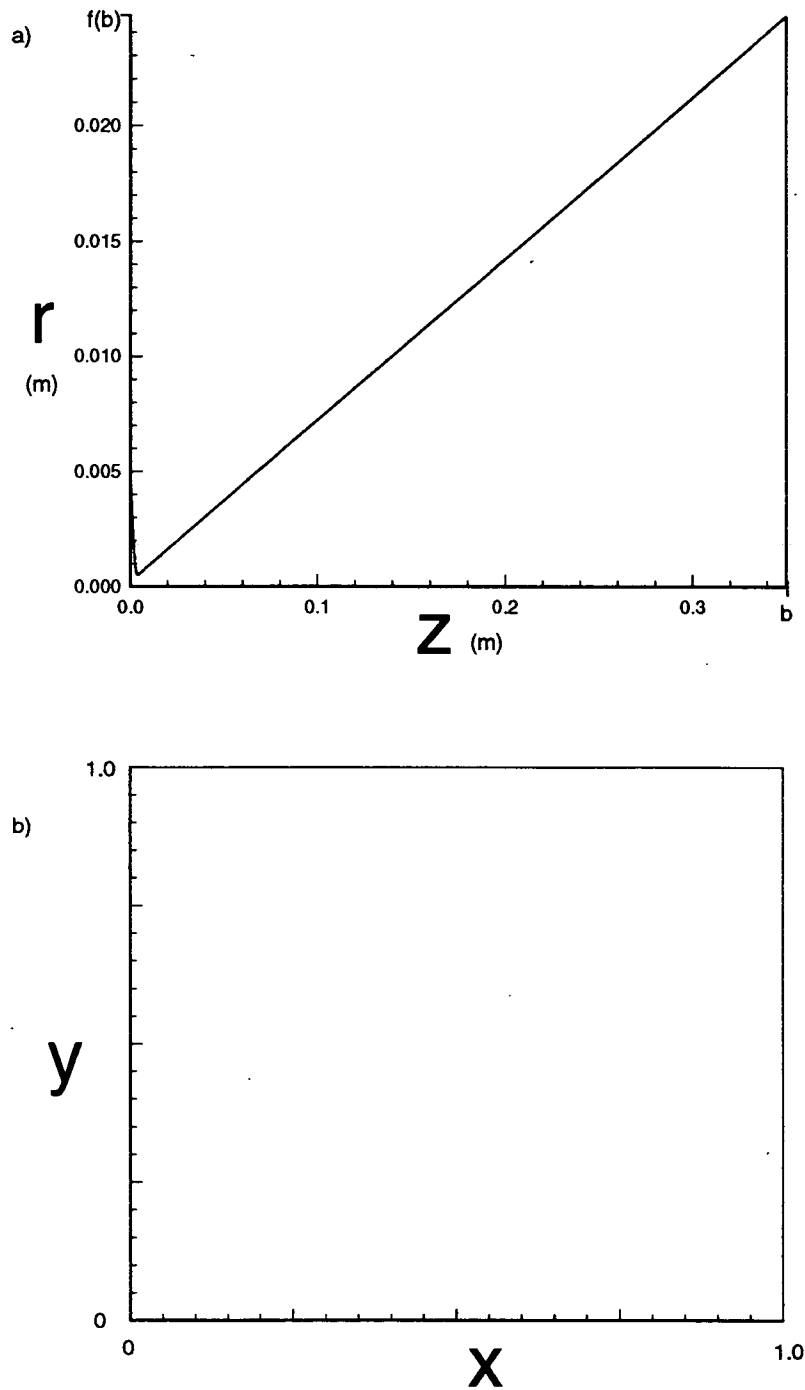


Figure 2.3. a) Physical Domain: $0 \leq z \leq b, 0 \leq r \leq f(z)$.

b) Computational Domain: $0 \leq x \leq 1, 0 \leq y \leq 1$.

2.3 Boundary Conditions

The steady solution of the equations is uniquely defined by the boundary conditions. In order to obtain a meaningful solution, boundary conditions must be applied that are not only applied correctly but are physically meaningful [13]. The conditions are expressed in terms of the primitive variables $\{\rho, V_r, V_z, T_{rt}, T_v, P\}$ and are converted to conservative variables when implemented numerically.

At the inflow boundary, the translational-rotational temperature is held fixed at some initial value T_0 . The vibrational temperature is assumed to be in equilibrium with the translational-rotational temperature and is also held constant at T_0 . In computational coordinates, the gas is assumed to enter the nozzle parallel to the centerline, so the radial velocity is assumed to be zero. The axial velocity is held fixed at an initial velocity, V_0 . Finally, since the flow is subsonic inflow and supersonic outflow, an analysis of the flow characteristics of Euler's equations suggests that one boundary condition must be left free to change with the solution of the interior flow [14], [15]. To this end, the density values are extrapolated from interior data. In the computational domain, this represents the condition $\frac{\partial \rho}{\partial x} = 0$. This is equivalent to the conditions $\frac{\partial \rho}{\partial z} = 0$ and $\frac{\partial \rho}{\partial r} = 0$ in the solution domain.

At the far-field boundary, the flow is supersonic. All variables are extrapolated,
or

$$\frac{\partial \rho}{\partial x} = \frac{\partial V_z}{\partial x} = \frac{\partial V_r}{\partial x} = \frac{\partial T_{rt}}{\partial x} = \frac{\partial T_v}{\partial x} = 0. \quad (2.66)$$

Since

$$\frac{\partial P}{\partial x} = \rho R \frac{\partial T_{rt}}{\partial x} + RT_{rt} \frac{\partial \rho}{\partial x} = 0, \quad (2.67)$$

the pressure is also extrapolated.

The symmetry of the nozzle is used to specify the conditions on the centerline. Assuming that the quantities above the center axis are mirrored by those below,

$$\frac{\partial \rho}{\partial r} = \frac{\partial V_r}{\partial r} = \frac{\partial V_z}{\partial r} = \frac{\partial T_{rt}}{\partial r} = \frac{\partial T_v}{\partial r} = \frac{\partial P}{\partial r} = 0. \quad (2.68)$$

In the computational coordinates these conditions are simply

$$\frac{\partial \rho}{\partial y} = \frac{\partial V_r}{\partial y} = \frac{\partial V_z}{\partial y} = \frac{\partial T_{rt}}{\partial y} = \frac{\partial T_v}{\partial y} = \frac{\partial P}{\partial y} = 0. \quad (2.69)$$

Furthermore, along $y = 0$,

$$V_r = 0 \quad (2.70),$$

since the radial velocity at the centerline must flow equally in the positive and negative directions.

Lastly, boundary conditions on the nozzle wall are governed by the nozzle shape and the viscosity. Due to the assumed roughness of the nozzle surface, no-slip conditions are applied to the velocities,

$$V_r = V_z = 0. \quad (2.71)$$

The translational-rotational as well as the vibrational temperatures are extrapolated such that

$$\frac{\partial T_{rt}}{\partial y} = \frac{\partial T_v}{\partial y} = 0. \quad (2.72)$$

The pressure gradient normal to the wall is assumed to be zero,

$$\frac{\partial P}{\partial n} = 0. \quad (2.73)$$

In computational coordinates this condition becomes

$$\frac{\partial P}{\partial n} = \frac{\partial P}{\partial x} - \frac{b}{f(xb)f'(xb)}(1 + (f')^2)\frac{\partial P}{\partial y} = 0. \quad (2.74)$$

The density on the boundary is then calculated using the ideal gas law evaluated on the boundary.

2.4 Initial Conditions

The choice of initial conditions is also important. Values that are too far from the steady solution can make the numerical solution unstable. Also, the closer the initial conditions are to the steady solution, the less time is required for convergence. To minimize the convergence time, we approximate the steady state solution with the steady solution of the corresponding one-dimensional inviscid problem. The flow is assumed to be in thermal equilibrium and also isentropic. Since it is isentropic, there is no change in entropy, so $ds = 0$, where s is the entropy. Entropy is related to enthalpy by $\rho T ds = \rho dh - dP$, where h is the enthalpy and $h = e + RT$. Therefore $ds = 0$ implies

$$\frac{\rho dh - dP}{T} = 0. \quad (2.75)$$

Using the ideal gas law and the fact that $dh = C_p dT$,

$$\frac{1}{T}C_p dT - R\frac{dP}{P} = 0, \quad (2.76)$$

where C_p is the specific heat at constant pressure. Integration of this equation leads to

$$\frac{P}{P_0} = \left(\frac{T}{T_0}\right)^{\frac{\gamma}{2}} \left(\frac{1 - e^{-\frac{\phi}{T_0}}}{1 - e^{-\frac{\phi}{T}}}\right) e\left(\frac{\frac{\phi}{T}}{e^{\frac{\phi}{T}} - 1} - \frac{\frac{\phi}{T_0}}{e^{\frac{\phi}{T_0}} - 1}\right)$$

or

$$\frac{\rho}{\rho_0} = \left(\frac{T}{T_0} \frac{\phi}{\phi_0} \right)^{\frac{1}{2}} \left(\frac{1 - e^{-\frac{\phi}{T_0}}}{1 - e^{-\frac{\phi}{T}}} \right) e \left(\frac{\frac{\phi}{T}}{e^{\frac{\phi}{T}} - 1} - \frac{\frac{\phi}{T_0}}{e^{\frac{\phi}{T_0}} - 1} \right), \quad (2.77)$$

where T_0 is the inlet temperature. The one-dimensional energy equation is written as

$$C_p dT + V_z dV_z = 0. \quad (2.78)$$

Integration of this equation yields

$$V_z^2 - V_{z_0}^2 = 7R(T_0 - T) + 2R\phi \left(\frac{1}{e^{\frac{\phi}{T_0}} - 1} - \frac{1}{e^{\frac{\phi}{T}} - 1} \right), \quad (2.79)$$

where V_{z_0} is the initial axial velocity. The local one-dimensional Mach number, M , is calculated by the formula $M = V_z/a$ where a is the local sound speed which is defined as $a = (\gamma RT)^{\frac{1}{2}}$. Note that thermal equilibrium is assumed, so sound speed can be defined. Dividing equation (2.78) by a^2 yields

$$M^2 = \frac{V_{z_0}^2}{\gamma RT} + \frac{7}{\gamma} \left(\frac{T}{T_0} - 1 \right) + \frac{2\phi}{\gamma T} \left(\frac{1}{e^{\frac{\phi}{T_0}} - 1} - \frac{1}{e^{\frac{\phi}{T}} - 1} \right). \quad (2.80)$$

The continuity of momentum is expressed by $AV_z\rho = A^*V_z^*\rho^*$, where A is the area of the nozzle and the starred quantities represent the values at the throat. At the nozzle throat, $M^* = 1$. From equation (2.77) and (2.80), the solution variables at the throat can be completely determined. From these values the solution variables throughout the nozzle are determined. Figures 2.4-2.7 represent the solution to the one-dimensional model for the stagnation conditions specified for the test case considered in chapter 4.

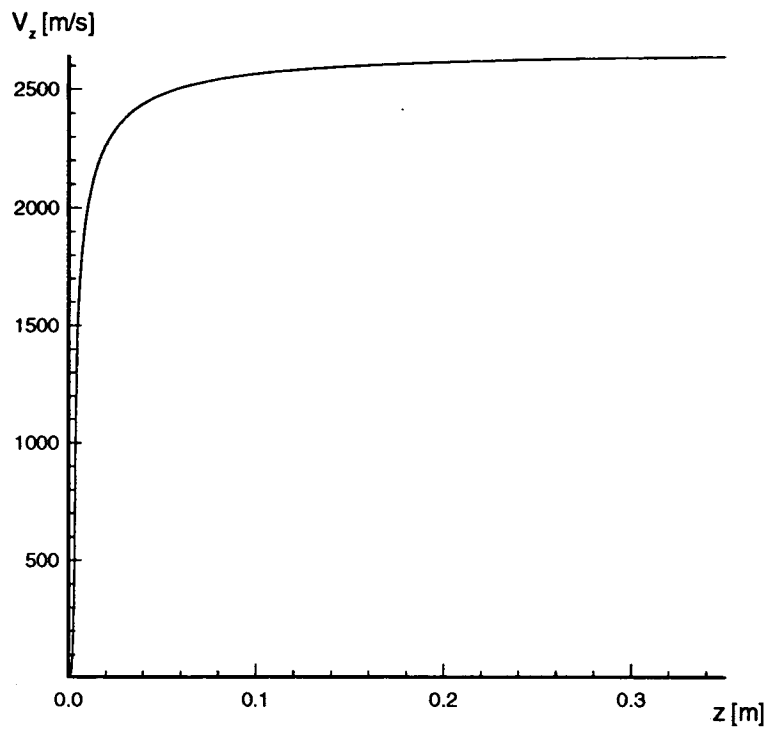


Figure 2.4. One-dimensional Model: Velocity vs Distance.

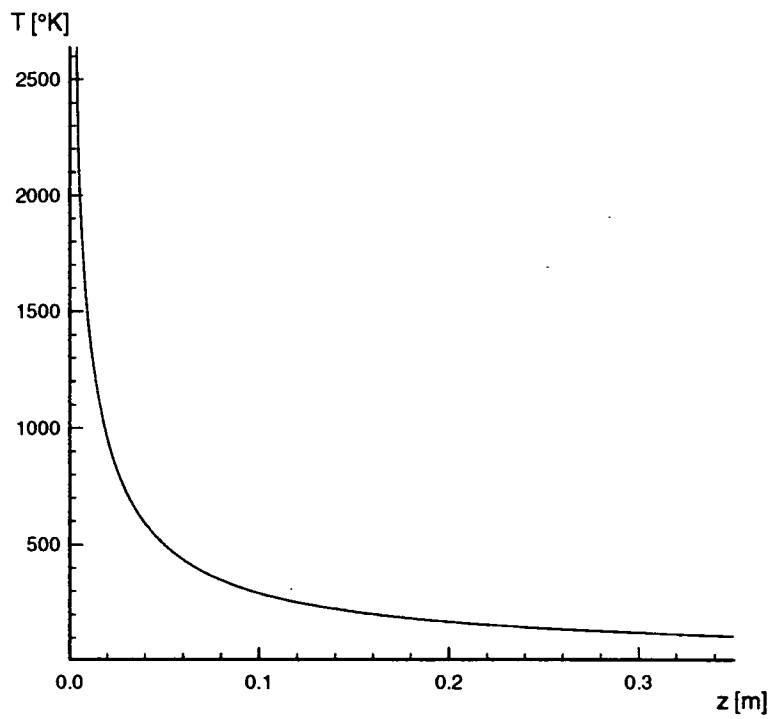


Figure 2.5. One-dimensional Model: Temperature vs Distance.

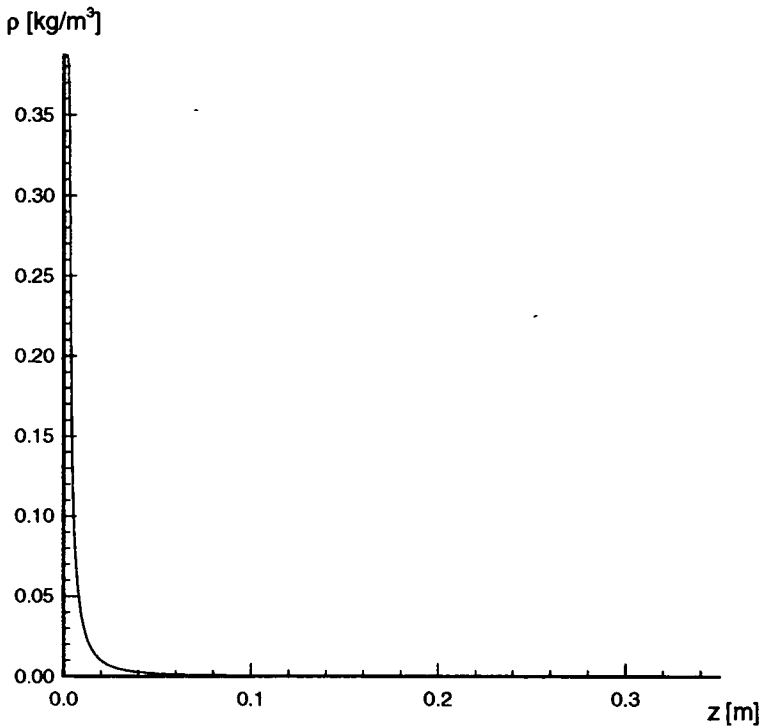


Figure 2.6. One-dimensional Model: Density vs Distance.

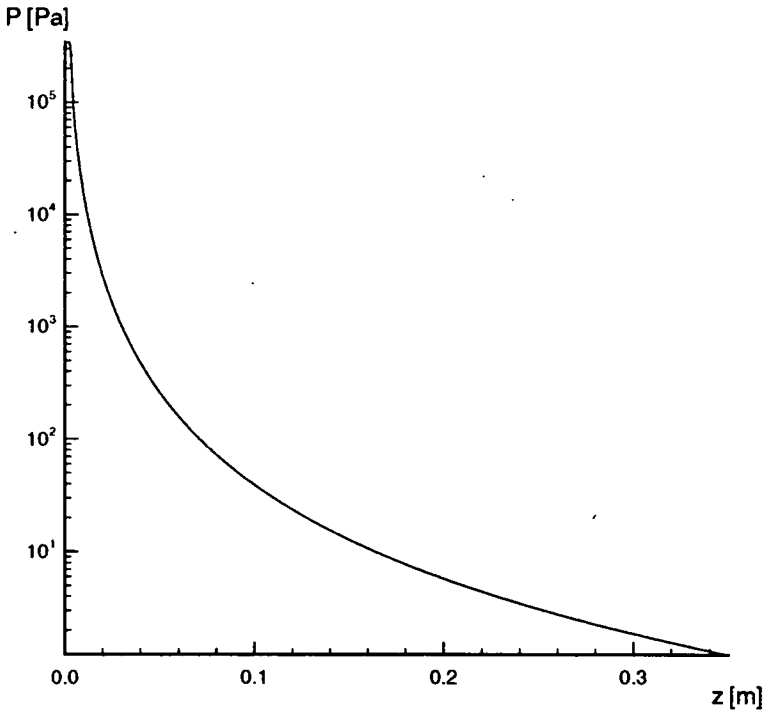


Figure 2.7. One-dimensional Model: Pressure vs Distance.

These values are then used as the centerline values for the two-dimensional viscous flow problem. They are extrapolated toward the nozzle wall. At the wall itself, the velocities are set equal to zero to satisfy the no-slip condition. The density and the translational-rotational temperature values are set to satisfy their specified boundary conditions. The vibrational temperature is considered to be in equilibrium with the translational-rotational temperature before the throat, so T_v is set equal to T_{rt} . After the throat, T_v is assumed to be frozen and is set equal to the centerline T_{rt} value at the throat. This frozen behavior is somewhat contrived, since the actual behavior of the vibrational temperature is unknown. Also, even if freezing is the actual behavior, the frozen temperature and the distance of the 'freezing' point from the throat are unknown.

CHAPTER 3

NUMERICAL METHODS

3.1 Introduction

The governing equations are the system of non-linear partial differential equations

$$\frac{\partial U}{\partial t} + \frac{\partial F}{\partial x} + \frac{\partial G}{\partial y} + H = 0, \quad (3.1)$$

where t is understood to be t^* , the scaled time and U , F , G , and H are the vectors previously defined by equations (2.57), (2.58), (2.59), (2.60), and (2.64). The steady-state solution to this system is desired when x and y are restricted to the computational domain, $0 \leq x \leq 1$ and $0 \leq y \leq 1$. It is not possible to generate a closed, analytic solution, so a numerical solution is necessary. Many numerical methods attempt to accurately represent the differential system as a system of linear algebraic equations. This is achieved by replacing derivatives with finite differences.

For the solution variables, an initial set of values, U^0 , is assumed which represent the system variables at time t . Then for some time increment, Δt , a solution set, U^1 , is derived from the system of equations evaluated at time $t + \Delta t$. The time dependant problem considers the discrete set of solutions, $\{U^n : n = 0, 1, 2, \dots\}$, where U^n is derived from the equations evaluated at time $t + n\Delta t$. The temporal

derivatives of the equations can be eliminated by using the finite difference:

$$\frac{\partial U^{n+1}}{\partial t} = \frac{U^{n+1} - U^n}{\Delta t} + O(\Delta t), \quad (3.2)$$

which is first order accurate. By substitution into equation (3.1), an explicit method can be developed of the form

$$U^{n+1} = F[U^n], \quad (3.3)$$

where F is some function which advances a given solution at time $t + n\Delta t$ to a new solution at time $t + (n + 1)\Delta t$. Methods of the form

$$U^{n+1} = F[U^n, U^{n+1}] \quad (3.4)$$

are implicit and require different solution techniques depending upon the function F .

To replace the spatial derivatives, the solution domain is discretized into a grid of points consisting of $n + 1$ rows and $m + 1$ columns. For every grid point (i, j) there is a corresponding solution set $U_{i,j}^n$. The points in rows 0 and n , or columns 0 and m , are boundary points, and the remaining points are interior points. The spacing between rows and columns varies to allow finer resolution near the throat and in the boundary layer. In the axial direction the grid is divided into four regions in which the spacing increases. The grid is divided into three regions in the radial direction, and the spacing is decreasing. This forms a total of twelve separately spaced regions. Using the coordinate transformation, equation (2.62), the solution grid is transformed into a computational grid, as in figure 3.1. From Taylor series

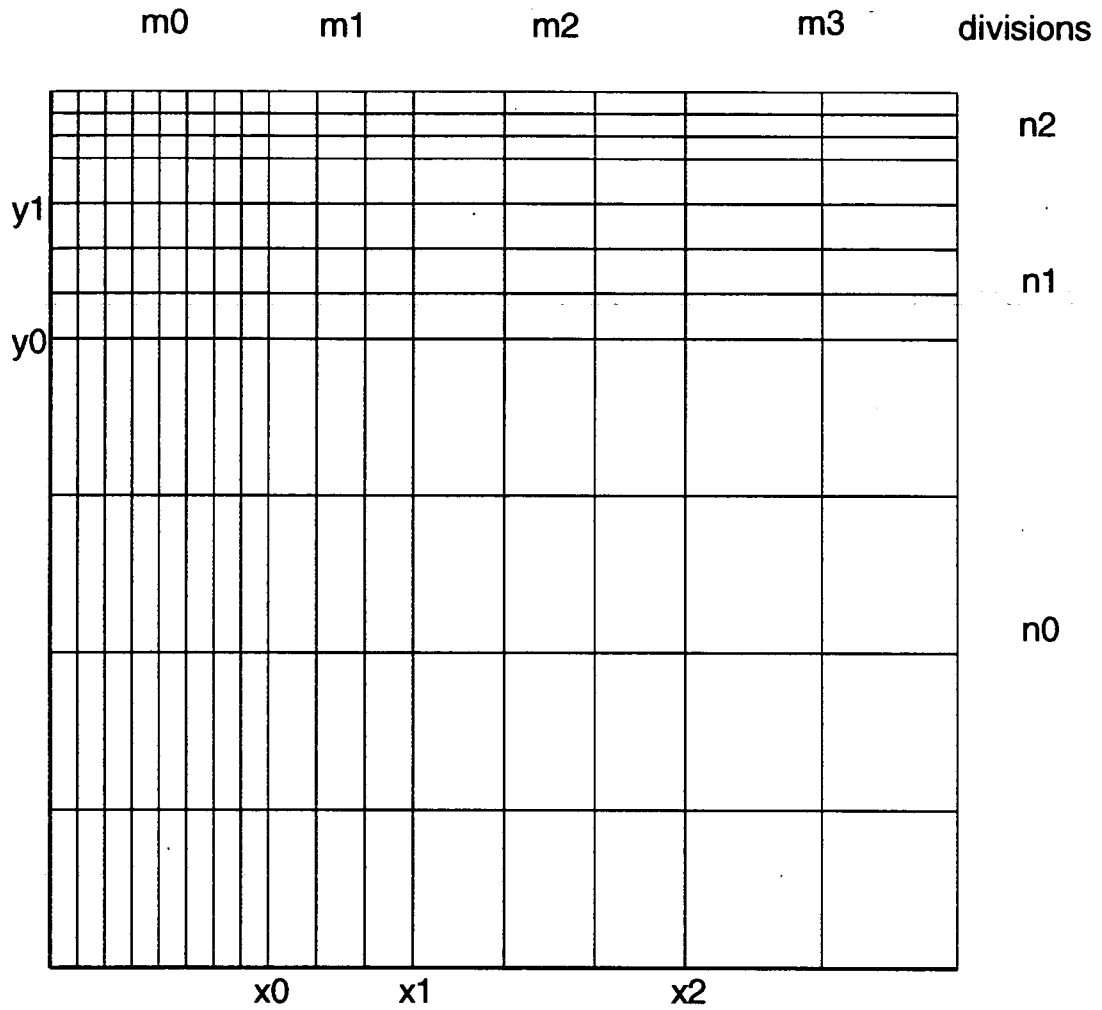


Figure 3.1. Generalized Grid Structure.

expansions of neighboring points, simple finite difference formulas are derived.

Those using downstream data points are forward differences:

$$\frac{\partial U_{i,j}^n}{\partial x} = \frac{U_{i+1,j}^n - U_{i,j}^n}{h1} + O(h1), \quad \frac{\partial U_{i,j}^n}{\partial y} = \frac{U_{i,j+1}^n - U_{i,j}^n}{k1} + O(k1). \quad (3.5)$$

Formulas using upstream values are backward differences:

$$\frac{\partial U_{i,j}^n}{\partial x} = \frac{U_{i,j}^n - U_{i-1,j}^n}{h2} + O(h2), \quad \frac{\partial U_{i,j}^n}{\partial y} = \frac{U_{i,j}^n - U_{i,j-1}^n}{k2} + O(k2), \quad (3.6)$$

where $k1$, $k2$, $h1$, and $h2$ are the grid spacings defined in figure 3.2.

For the Navier-Stokes equations, a popular time-dependent method is the explicit MacCormack predictor/corrector method which was first developed in 1969, reference [8]. Each time iteration requires two explicit time steps of the form:

Predictor :

$$U_{i,j}^{n+1} = U_{i,j}^n - \frac{\Delta t}{h1}(F_{i+1,j}^n - F_{i,j}^n) - \frac{\Delta t}{k1}(G_{i,j+1}^n - G_{i,j}^n) - \Delta t H_{i,j}^n, \quad (3.7)$$

Corrector :

$$U_{i,j}^{n+1} = \frac{1}{2}(U_{i,j}^n + U_{i,j}^{n+1} - \frac{\Delta t}{h2}(F_{i,j}^n - F_{i-1,j}^n) - \frac{\Delta t}{k2}(G_{i,j}^n - G_{i,j-1}^n) - \Delta t H_{i,j}^n). \quad (3.8)$$

Explicit methods change variables locally so that information at a grid point can not be allowed to travel past the next grid point in one time step. Thus a restriction must be placed upon the Δt time step value. This method provides a stable numerical solution when Δt satisfies the Courant-Friedrichs-Lewy (CFL) condition defined by

$$\Delta t \leq \frac{.9(\Delta t)_{CFL}}{1 + 2/Re_{\Delta}}, \quad (3.9)$$

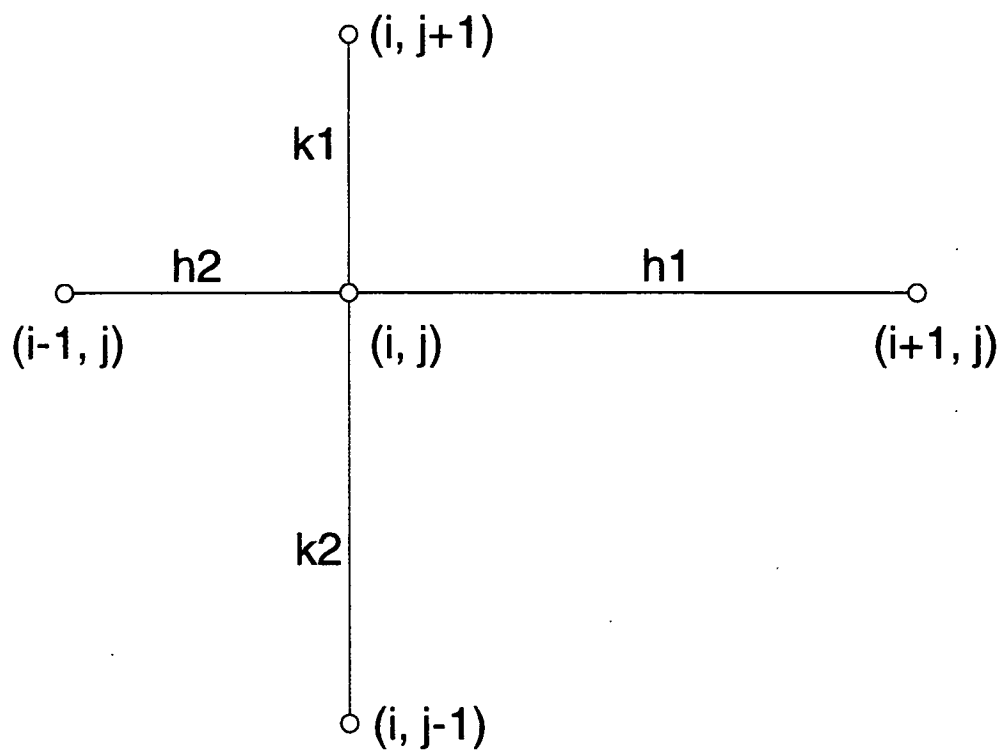


Figure 3.2. Lengths for Irregular Grid Spacings.

where

$$\Delta t_{CFL} = \left(\frac{|V_x|}{\Delta x} + \frac{|V_y|}{\Delta y} + a \sqrt{\frac{1}{(\Delta x)^2} + \frac{1}{(\Delta y)^2}} \right)^{-1}, \quad (3.10)$$

$$Re_{\Delta} = \min\left(\frac{\rho|V_x|\Delta x}{\eta}, \frac{\rho|V_y|\Delta y}{\eta}\right), \quad (3.11)$$

and a is the local sound speed [16]. For a nozzle with large axial velocity and finely resolved grids, the necessary Δt value is unreasonably small. This results in long computer run times. To avoid the CFL restriction, an implicit solution method is used.

3.2 Beam and Warming Method

The most notable implicit method is that of Beam and Warming [17]. The temporal derivative is replaced by a more accurate, trapezoidal, time differencing formula:

$$\Delta U^{n+1} = \frac{1}{2}\Delta t \frac{\partial \Delta U^{n+1}}{\partial t} + \frac{1}{2}\Delta t \frac{\partial U^n}{\partial t} + O(\Delta t^3), \quad (3.12)$$

where

$$\Delta U^{n+1} = U^{n+1} - U^n. \quad (3.13)$$

This allows the method to be second order accurate in time. In terms of ΔU , equation (3.1) becomes,

$$\frac{\partial(\Delta U^{n+1})}{\partial t} = \frac{\partial(U^{n+1} - U^n)}{\partial t} = -\frac{\partial(F^{n+1} - F^n)}{\partial x} - \frac{\partial(G^{n+1} - G^n)}{\partial y} - (H^{n+1} - H^n). \quad (3.14)$$

In order to simplify equation (3.14), observe that the Taylor series expansion of F with respect to time is

$$F^{n+1} = F^n + \frac{\partial F}{\partial t} \Delta t + \frac{\partial^2 F}{\partial t^2} (\Delta t)^2 + \dots \quad (3.15)$$

Since Δt is small, terms $O((\Delta t)^2)$ and smaller can be neglected. Also F is a function of the conservative variables, U , so the chain rule can be applied to $\frac{\partial F}{\partial t}$ to produce

$$F^{n+1} = F^n + \frac{\partial F}{\partial U} \frac{\partial U}{\partial t} \Delta t. \quad (3.16)$$

By letting $A = \frac{\partial F}{\partial U}$ and using equation (3.2), equation (3.16) becomes

$$F^{n+1} = F^n + A\Delta U^{n+1}. \quad (3.17)$$

Likewise,

$$G^{n+1} = G^n + \frac{\partial G}{\partial U} \frac{\partial U}{\partial t} \Delta t = G^n + B\Delta U^{n+1}. \quad (3.18)$$

and

$$H^{n+1} = H^n + \frac{\partial H}{\partial U} \frac{\partial U}{\partial t} \Delta t = H^n + C\Delta U^{n+1}, \quad (3.19)$$

where $B = \frac{\partial G}{\partial U}$ and $C = \frac{\partial H}{\partial U}$. The quantities $\frac{\partial F}{\partial U}$, $\frac{\partial G}{\partial U}$, and $\frac{\partial H}{\partial U}$ are the Jacobian matrices. Substituting these expansions into equation (3.14) yields

$$\frac{\partial(\Delta U^{n+1})}{\partial t} = -\frac{\partial}{\partial x}(A\Delta U^{n+1}) - \frac{\partial}{\partial y}(B\Delta U^{n+1}) - C\Delta U^{n+1}. \quad (3.20)$$

The derivatives in equation (3.12) can be replaced, using equations (3.1) and (3.20), resulting in

$$\begin{aligned} \Delta U^{n+1} = & \frac{1}{2}\Delta t \left(-\frac{\partial}{\partial x}(A\Delta U^{n+1}) - \frac{\partial}{\partial y}(B\Delta U^{n+1}) - C\Delta U^{n+1} \right) + \\ & + \frac{1}{2}\Delta t \left(-\frac{\partial F^n}{\partial x} - \frac{\partial G^n}{\partial y} - H^n \right). \end{aligned} \quad (3.21)$$

By introducing the operator notation:

$$\left(\frac{\partial A}{\partial x} \right) \Delta U^{n+1} = \frac{\partial(A\Delta U^{n+1})}{\partial x}, \quad \left(\frac{\partial B}{\partial y} \right) \Delta U^{n+1} = \frac{\partial(B\Delta U^{n+1})}{\partial y}, \quad (3.22)$$

equation (3.21) can be expressed as

$$\left(I + \frac{1}{2}\Delta t \frac{\partial A}{\partial x} + \frac{1}{2}\Delta t \frac{\partial B}{\partial y} + \frac{1}{2}\Delta t C\right)\Delta U^{n+1} = \frac{1}{2}\Delta t \left(-\frac{\partial F^n}{\partial x} - \frac{\partial G^n}{\partial y} - H^n\right). \quad (3.23)$$

In the computational domain, there are mn of these equations which must be solved simultaneously. To achieve this requires the inversion of a block pentadiagonal matrix. To simplify the required computation, the operators of equation (3.23) are factored:

$$\left(I + \frac{1}{2}\Delta t \frac{\partial A}{\partial x}\right)\left(I + \frac{1}{2}\Delta t \frac{\partial B}{\partial y} + \frac{1}{2}\Delta t C\right)\Delta U^{n+1} = \frac{1}{2}\Delta t \left(-\frac{\partial F^n}{\partial x} - \frac{\partial G^n}{\partial y} - H^n\right). \quad (3.24)$$

This equation can then be solved stepwise as follows:

$$\left(I + \frac{1}{2}\Delta t \frac{\partial A}{\partial x}\right)\Delta V^{n+1} = \frac{1}{2}\Delta t \left(-\frac{\partial F^n}{\partial x} - \frac{\partial G^n}{\partial y} - H^n\right), \quad (3.25)$$

$$\left(I + \frac{1}{2}\Delta t \frac{\partial B}{\partial y} + \frac{1}{2}\Delta t C\right)\Delta U^{n+1} = \Delta V^{n+1}. \quad (3.26)$$

Each step now requires the inversion of a block tridiagonal matrix. However, equations (3.23) and (3.24) are not equivalent. If the factors are multiplied, the terms $\frac{1}{4}(\Delta t)^2 \frac{\partial A}{\partial x} \frac{\partial B}{\partial y} + \frac{1}{2}(\Delta t)^2 \frac{\partial A}{\partial x} C$ arise in addition to those in the original operator. This produces an error proportional to $\frac{(\Delta t)^2}{\Delta x \Delta y} \|A\| \|B\|$, which is insignificant for small Δt .

Thus, a restriction on the Δt value is still required [8].

3.3 Steger-Warming Flux Vector Splitting Method

To this basic form, the flux vector splitting developed by Steger and Warming, reference [9], is incorporated which considers the one-dimensional Euler equations

$$\frac{\partial U}{\partial t} + \frac{\partial F}{\partial x} = 0 \quad (3.27)$$

where $F = [\rho V_x, V_x^2/\rho + P, (e + P)V_x]^T$. The vector F is considered to be a homogeneous function of degree one since it has the property

$$F(cU) = cF(U), \quad (3.28)$$

for any scalar c . From the previous development, equation (3.27) can be written as

$$\frac{\partial U}{\partial t} + A \frac{\partial U}{\partial x} = 0, \quad (3.29)$$

where A is the Jacobian matrix associated with F and which, for simplicity, is assumed to be constant. Since F is homogeneous it also has the property that $F = AU$. Since equation (3.29) is hyperbolic, the eigenvalues of the equation, λ_n , are real. Also a similarity transformation exists of the form $S^{-1}AS = E$, where E is the diagonal eigenvalue matrix. Using this transformation and defining $U' = S^{-1}U$, equation (3.29) can be written as an eigenvalue problem

$$\frac{\partial U'}{\partial t} + \lambda_n \frac{\partial U'}{\partial x} = 0. \quad (3.30)$$

If a backward difference is substituted for the spatial derivative, the solution of equation (3.30) is stable only if the corresponding eigenvalue is positive. Conversely, if a forward difference is used, the solution is stable only for negative eigenvalues.

Neither difference scheme, or any other, is stable for both positive and negative eigenvalues [9]. Thus directing the finite differences in the direction in which the information is propagated increases the stability of the system.

This knowledge can then be applied to the present system of equations. The Navier-Stokes equations, however, do not exhibit purely hyperbolic behavior nor are the functions F and G homogeneous. To this end the functions F , and G are split into homogeneous functions, F_h and G_h , and non-homogeneous functions, F_v and G_v , such that

$$F = F_h + F_v, \quad G = G_h + G_v, \quad (3.31)$$

and

$$F_h = \frac{L}{b} \begin{bmatrix} \rho^* V_z^* \\ \rho^* V_r^* V_z^* \\ \rho^* V_z^* V_z^* + P^* \\ (E_{rt}^* + P^*) V_z^* \\ E_v^* V_z^* \end{bmatrix} \quad (3.32)$$

$$F_v = \frac{L}{b} \begin{bmatrix} 0 \\ -\frac{L^2}{\delta^2} \frac{1}{Re} \tau_{rz}^* \\ -\frac{L^2}{\delta^2} \frac{1}{Re} \tau_{zz}^* \\ -V_r^* \frac{1}{Re} \tau_{rz}^* - V_z^* \frac{1}{Re} \tau_{zz}^* + q_{rtz}^* \\ + q_{vz}^* \end{bmatrix} \quad (3.33)$$

$$G_h = \frac{\delta}{f(xb)} \begin{bmatrix} \rho^* V_r^* \\ \rho^* V_r^* V_r^* + \frac{L^2}{\delta^2} P^* \\ \rho^* V_r^* V_z^* \\ (E_{rt}^* + P^*) V_r^* \\ E_v^* V_r^* \end{bmatrix} - \frac{Lyf'(xb)}{f(xb)} \begin{bmatrix} \rho^* V_z^* \\ \rho^* V_r^* V_z^* \\ \rho^* V_z^* V_z^* + P^* \\ (E_{rt}^* + P^*) V_z^* \\ E_v^* V_z^* \end{bmatrix} \quad (3.34)$$

$$G_v = \frac{\delta}{f(xb)} \begin{bmatrix} 0 \\ -\frac{L^2}{\delta^2} \frac{1}{Re} \tau_{rr}^* \\ -\frac{L^2}{\delta^2} \frac{1}{Re} \tau_{rz}^* \\ -V_r^* \frac{1}{Re} \tau_{rr}^* - \frac{L^2}{\delta^2} V_z^* \frac{1}{Re} \tau_{rz}^* + q_{tr}^* \\ q_{vr}^* \end{bmatrix} - \frac{Lyf'(xb)}{f(xb)} \begin{bmatrix} 0 \\ -\frac{L^2}{\delta^2} \frac{1}{Re} \tau_{rz}^* \\ -\frac{1}{Re} \tau_{zz}^* \\ -V_r^* \frac{1}{Re} \tau_{rz}^* - V_z^* \frac{1}{Re} \tau_{zz}^* + q_{rtz}^* \\ q_{vz}^* \end{bmatrix}. \quad (3.35)$$

Also define $A_h = \frac{\partial F_h}{\partial U}$, $B_h = \frac{\partial G_h}{\partial U}$, $A_v = \frac{\partial F_v}{\partial U}$, $B_v = \frac{\partial G_v}{\partial U}$, and note that $A = A_h + A_v$ and $B = B_h + B_v$. The vector H and matrix C are not altered.

To implement the vector splitting for matrix A_h , the eigenvalues of A_h are calculated numerically. From these the diagonal eigenvalue matrix E is formed. Also, the matrix S and its inverse S^{-1} of the similarity transformation are calculated such that $A_h = SES^{-1}$. Next, the diagonal matrix E is split by $E = E^+ + E^-$, where E^+ contains the positive eigenvalues and E^- contains the negative eigenvalues. Finally, the flux matrix A_h is split by $A_h = A^+ + A^-$ where

$$A^+ = SE^+S^{-1}, \quad A^- = SE^-S^{-1}. \quad (3.36)$$

Similarly, the flux matrix B_h is split using its respective eigenvalues such that $B_h = B^+ + B^-$. This allows equation (3.24) to be written as

$$\begin{aligned}
 (I + \frac{1}{2}\Delta t(\frac{\partial A^+}{\partial x} + \frac{\partial A^-}{\partial x} + \frac{\partial A_v}{\partial x}))(I + \frac{1}{2}\Delta t(\frac{\partial B^+}{\partial y} + \frac{\partial B^-}{\partial y} + \frac{\partial B_v}{\partial y}) + \frac{1}{2}\Delta t C)\Delta U^{n+1} \\
 = \frac{1}{2}\Delta t(-\frac{\partial F}{\partial x} - \frac{\partial G}{\partial y} - H)|^n. \tag{3.37}
 \end{aligned}$$

This is equivalent to

$$(I + \frac{1}{2}\Delta t(\frac{\partial A^+}{\partial x} + \frac{\partial A^-}{\partial x} + \frac{\partial A_v}{\partial x})\Delta V^{n+1} = \frac{1}{2}\Delta t(-\frac{\partial F}{\partial x} - \frac{\partial G}{\partial y} - H)|^n, \tag{3.38}$$

$$(I + \frac{1}{2}\Delta t(\frac{\partial B^+}{\partial y} + \frac{\partial B^-}{\partial y} + \frac{\partial B_v}{\partial y}) + \frac{1}{2}\Delta t C)\Delta U^{n+1} = \Delta V^{n+1}. \tag{3.39}$$

Since A^+ and B^+ represent the homogeneous contributions of the system with positive eigenvalues, backward differences are used for $\frac{\partial A^+}{\partial x}$ and $\frac{\partial B^+}{\partial y}$. Likewise, forward differences are used for $\frac{\partial A^-}{\partial x}$ and $\frac{\partial B^-}{\partial y}$. The non-homogeneous matrices A_v and B_v are not affected by flux splitting. They are primarily viscous terms and central differences are used for $\frac{\partial A_v}{\partial x}$ and $\frac{\partial B_v}{\partial y}$ since they do not create dispersive instabilities [14]. For the given grid structure, the central differences are

$$\frac{\partial A_{vi,j}}{\partial x} = \frac{1}{h1 + h2} [\frac{h2}{h1} A_{vi+1,j} + (\frac{h1}{h2} - \frac{h2}{h1}) A_{vi,j} - \frac{h1}{h2} A_{vi-1,j}] + O(h^2), \tag{3.40}$$

and

$$\frac{\partial B_{vi,j}}{\partial y} = \frac{1}{k1 + k2} [\frac{k2}{k1} B_{vi,j+1} + (\frac{k1}{k2} - \frac{k2}{k1}) B_{vi,j} - \frac{k1}{k2} B_{vi,j-1}] + O(k^2), \tag{3.41}$$

where $h = \max(h1, h2)$ and $k = \max(k1, k2)$. Since the errors associated with these formulae are quadratic, they provide more accuracy than the forward or backward differences. For this reason, spatial derivatives that are evaluated in the Jacobian

matrices as well as the F, G, and H matrices are also central differenced when possible. By replacing the derivatives in equation (3.38) and equation (3.39) by the appropriate difference formulae, the equation for $\Delta U_{i,j}^{n+1}$ becomes

$$\begin{aligned} & \Delta V_{i,j}^{n+1} + \frac{1}{2}\Delta t \left(\frac{1}{h2}(A_{i,j}^+ \Delta V_{i,j}^{n+1} - A_{i-1,j}^+ \Delta V_{i-1,j}^{n+1}) + \frac{1}{h1}(A_{i+1,j}^- \Delta V_{i+1,j}^{n+1} - A_{i,j}^- \Delta V_{i,j}^{n+1}) \right) \\ & + \frac{1}{h1+h2} \left[\frac{h2}{h1} A_{vi+1,j} \Delta V_{i+1,j}^{n+1} + \left(\frac{h1}{h2} - \frac{h2}{h1} \right) A_{vi,j} \Delta V_{i,j}^{n+1} - \frac{h1}{h2} A_{vi-1,j} \Delta V_{i-1,j}^{n+1} \right] = r h s (3.38), \end{aligned} \quad (3.42)$$

$$\begin{aligned} & \Delta U_{i,j}^{n+1} + \frac{1}{2}\Delta t \left(\frac{1}{k2}(B_{i,j}^+ \Delta U_{i,j}^{n+1} - B_{i,j-1}^+ \Delta U_{i,j-1}^{n+1}) + \frac{1}{k1}(B_{i,j-1}^- \Delta U_{i,j-1}^{n+1} - B_{i,j}^- \Delta U_{i,j}^{n+1}) \right) \\ & + \frac{1}{k1+k2} \left[\frac{k2}{k1} B_{vi,j+1} \Delta U_{i,j+1}^{n+1} + \left(\frac{k1}{k2} - \frac{k2}{k1} \right) B_{vi,j} \Delta U_{i,j}^{n+1} - \frac{k1}{k2} B_{vi,j-1} \Delta U_{i,j-1}^{n+1} \right] = \Delta V_{i,j}^{n+1}. \end{aligned} \quad (3.43)$$

Rearranging terms yields

$$\begin{aligned} & \frac{1}{2} \left(\frac{1}{h1} A_{i+1,j}^- + \frac{h2}{h1(h1+h2)} A_{vi+1,j} \right) \Delta V_{i+1,j}^{n+1} \\ & + \left(1 + \frac{1}{2}\Delta t \left(\frac{1}{h2} A_{i,j}^+ - \frac{1}{h1} A_{i,j}^- + \frac{1}{h1+h2} \left(\frac{h1}{h2} - \frac{h2}{h1} \right) A_{vi,j} \right) \right) \Delta V_{i,j}^{n+1} \\ & + \frac{1}{2}\Delta t \left(-\frac{1}{h2} A_{i-1,j}^+ - \frac{h1}{h2(h1+h2)} A_{vi-1,j} \right) \Delta V_{i-1,j}^{n+1} = r h s (3.38), \end{aligned} \quad (3.44)$$

$$\begin{aligned} & \frac{1}{2} \left(\frac{1}{k1} B_{i,j+1}^- + \frac{k2}{k1(k1+k2)} B_{vi,j+1} \right) \Delta U_{i,j+1}^{n+1} \\ & + \left(1 + \frac{1}{2}\Delta t \left(\frac{1}{k2} B_{i,j}^+ - \frac{1}{k1} B_{i,j}^- + \frac{1}{k1+k2} \left(\frac{k1}{k2} - \frac{k2}{k1} \right) B_{vi,j} \right) \right) \Delta U_{i,j}^{n+1} \\ & + \frac{1}{2}\Delta t \left(-\frac{1}{k2} B_{i,j-1}^+ - \frac{k1}{k2(k1+k2)} B_{vi,j-1} \right) \Delta U_{i,j-1}^{n+1} = \Delta V_{i,j}^{n+1}. \end{aligned} \quad (3.45)$$

This system of equations has the matrix form:

$$[C_1][\Delta V^{n+1}] = [r h s], \quad (3.46)$$

$$[C_2][\Delta U^{n+1}] = [\Delta V^{n+1}], \quad (3.47)$$

where $[C_1]$ and $[C_2]$ are $(5n)$ square coefficient matrices and $[\Delta V^{n+1}]$, $[\Delta U^{n+1}]$, and $[rhs]$ are column vectors of length $5n$. The matrices $[C_1]$ and $[C_2]$ are block tridiagonal and can be readily inverted. Figure 3.3 shows the non-zero entries of the matrices $[C_1]$ and $[C_2]$, where each element is a 5×5 matrix.

For some values of i and j , the ΔV^{n+1} and ΔU^{n+1} values associated with boundary points are required. In cases where the boundary values remain constant, $\Delta V^{n+1} = 0$ and $\Delta U^{n+1} = 0$, and the form of equations (3.44) and (3.45) do not change. However, for complicated boundary conditions, the form can be significantly changed so that $[C_1]$ and/or $[C_2]$ are no longer tridiagonal. To avoid this problem, the boundary points are treated explicitly. In the implicit step, backward or forward differences are chosen at near boundary points so that the boundary points are not required. This preserves the tridiagonal nature of the matrices $[C_1]$ and $[C_2]$. The boundary points are only used in the explicit step. Since every time step is restricted by Δt , the variable changes at one time step are assumed to be nearly equal to the changes at the previous time step, so $\Delta V^{n+1} \approx \Delta V^n$ and $\Delta U^{n+1} \approx \Delta U^n$. Thus, boundary value changes can be calculated from known information and can be moved to the right hand sides of equations (3.46) and (3.47). To insure that the boundary conditions are satisfied, the boundary values are updated after each solution of the system.

The system can then be solved numerically and the set of ΔU^{n+1} values obtained. Using

$$U^{n+1} = U^n + \Delta U^{n+1}, \quad (3.48)$$

the variable values at the next time step are found by updating the previous values.

3.4 Implicit MacCormack Method

Another implicit method that is easily implemented is the implicit MacCormack method. As in the other implicit methods, the Taylor expansion of the governing equations resulted in equation (3.20), Using equation (3.1), this equation can be written as

$$\Delta U^{n+1} + \Delta t \left(\frac{\partial}{\partial x} (A \Delta U^{n+1}) + \frac{\partial}{\partial y} (B \Delta U^{n+1}) + C \Delta U^{n+1} \right) = \Delta t \left(-\frac{\partial F^n}{\partial x} - \frac{\partial G^n}{\partial y} - H^n \right). \quad (3.80)$$

This equation is then solved in the following sequence: Predictor step:

$$(\Delta U_{i,j})_{Explicit} = -\Delta t \left(\frac{\Delta_x E_{ij}^n}{\Delta x} + \frac{\Delta_y F_{ij}^n}{\Delta y} + H_{ij}^n \right) \quad (3.81)$$

$$\left(I + \Delta t \frac{\Delta_x \cdot A}{\Delta x} + \Delta t \frac{\Delta_y \cdot B}{\Delta y} + \Delta t C \right) \Delta U_{ij}^{*n+1} = (\Delta U_{ij}^n)_{Explicit}, \quad (3.82)$$

$$U_{ij}^{*n+1} = U_{ij}^n + \Delta U_{ij}^{*n+1} \quad (3.83)$$

Corrector step:

$$(\overline{\Delta U}_{ij})_{Explicit} = -\Delta t \left(\frac{\nabla_x (E^*)_{ij}^n}{\Delta x} + \frac{\nabla_y (F^*)_{ij}^n}{\Delta y} + (H^*)_{ij}^n \right) \quad (3.84)$$

$$\left(I + \Delta t \frac{\nabla_x \cdot A}{\Delta x} + \Delta t \frac{\nabla_y \cdot B}{\Delta y} + \Delta t C \right) \Delta U_{ij}^{n+1} = (\overline{\Delta U}_{ij}^n)_{Explicit} \quad (3.85)$$

$$U_{ij}^{n+1} = \frac{1}{2} [U_{ij}^n + (U^*)_{ij}^{n+1} \Delta U_{ij}^{n+1}] \quad (3.86)$$

Here Δ_x and Δ_y represent forward differences as in equation (3.5), and ∇_x and ∇_y are backward differences similar to equation (3.6).

The solution of these equations requires solving block tridiagonal matrices which are either upper or lower tridiagonal [figure 3.4]. This, however, causes no problem in implementation. The boundary points are treated explicitly. Since every time step is restricted by Δt , the variable changes at one time step are assumed to be nearly equal to the changes at the previous time step, so $\Delta U^{n+1} \approx \Delta U^n$. Thus, boundary value changes can be calculated from known information and can be moved to the right hand sides of equations (3.82) and (3.85). To insure that the boundary conditions are satisfied, the boundary values are updated after each solution of the system.

The major differences between this method and the Steger-Warming method is that the Jacobian matrices are not split, so convergence is assumed to be slower. In both methods, each iteration requires two 'sweeps'. The implicit MacCormack method sweeps in the downstream direction and then the upstream direction. The Steger-Warming method sweeps in the x-direction and then the y-direction. This difference may have some effect on the results.

3.5 Numerical Implementation of Boundary Conditions

To insure that the boundary conditions are satisfied, the boundary point values are updated after every iteration. The conditions specified in chapter two are converted from differential to algebraic equations using finite differencing.

Along the centerline, $j=0$, the conditions are of the form $\frac{\partial U}{\partial r} = 0$, which are equivalent to $\frac{\partial U}{\partial y} = 0$. This is implemented by replacing $\frac{\partial U}{\partial y}$ by a simple forward

difference

$$\frac{U_{i,1} - U_{i,0}}{k_1} + O(k_1) = 0. \quad (3.87)$$

The numerical boundary condition then becomes

$$U_{i,0} = U_{i,1} + O((k_1)^2). \quad (3.88)$$

Due to symmetry, $V_r = 0$, so $U_{2,i,0}$ is simply set equal to zero.

Along the far field boundary, $i=m$, the extrapolation conditions are of the form

$\frac{\partial U}{\partial x} = 0$. A backward difference is used to formulate the numerical condition

$$U_{m,j} = U_{m-1,j} + O((h_2)^2). \quad (3.89)$$

At the inflow boundary, $i=0$, all of the variables are kept at their initial values except the density which is extrapolated using the linear extrapolation similar to that used on the far field boundary,

$$U_{1,0,j} = U_{1,1,j} + O((h_1)^2). \quad (3.90)$$

On the nozzle wall boundary, $j=n$, the no-slip conditions are enforced and

$$U_{2,i,n} = U_{3,i,n} = 0. \quad (3.91)$$

The temperatures at the wall are extrapolated linearly,

$$T_{i,n} = T_{i,n-1} + O((k_1)^2), \quad (3.92)$$

where T is either $T_{r,t}$ or T_v . Using equation (2.74), the wall condition, $\frac{\partial P}{\partial n} = 0$, can be written as

$$\frac{\partial P}{\partial x} = \frac{b(1 + (f'(xb))^2)}{f(xb)f'(xb)} \frac{\partial P}{\partial y} = \alpha \frac{\partial P}{\partial y}. \quad (3.93)$$

Replacing $\frac{\partial P}{\partial y}$ with the second order backward difference

$$\frac{3P_{i,j} - 4P_{i,j-1} + P_{i,j-2}}{2k^2} + O((k^2)^2), \quad (3.94)$$

and $\frac{\partial P}{\partial x}$ by the backward difference

$$\frac{P_{i,j} - P_{i-1,j}}{h^2} + O(h^2),$$

equation (3.93) yields the numerical condition

$$P_{i,j} = \alpha^{-1} \left[-\frac{1}{h^2} P_{i-1,j} + \alpha (4P_{i,j-1} - P_{i,j-2}) \right] + O(\max(\frac{k^2(h^2)^2}{k^2 + h^2}, \frac{(k^2)^3 h^2}{k^2 + h^2})). \quad (3.95)$$

Since k^2 is usually smaller than h^2 at the wall, the error term is at most $O((h^2)^2)$, therefore it is of the same order as the rest. The density can then be calculated from the wall pressure and temperature using the ideal gas equation.

3.6 Conclusion

These methods require a certain amount of bookkeeping to be implemented. They are second order accurate in time and first order in space [16]. The use of the implicit method removes the CFL restriction on the time step. However, restrictions on the time step and grid spacings are still required, to keep the computational error small. Flux vector splitting is added to increase the stability of the numerical method. The boundary points are handled explicitly in order to maintain the structure of the matrix equations to be solved.

CHAPTER 4

NUMERICAL RESULTS

4.1 Introduction

To discover the effects of thermal nonequilibrium on nozzle flow, a test case is solved numerically using the methods discussed in the previous chapter. The test case had a stagnation pressure of 50 psi and a stagnation temperature of 3000 degrees K. Since there is assumed to be an initial velocity at the entrance of the nozzle, the term 'stagnation condition' is a misnomer. However, this velocity is comparatively small to any characteristic velocity, so these initial conditions are nearly the stagnation conditions. Also, some preliminary considerations must be investigated.

4.2 Validity of the Navier Stokes Equations

Rapidly expanding flows are characterized by a significant decrease in the density of the gas beyond the throat. For flows with low stagnation pressures, the exit densities can be extremely low. If the gas is very rarefied, it may no longer be a continuous fluid. In this case, the Navier-Stokes equations would no longer accurately represent the flow. In that case, the rarefied gas flow would usually be solved using Monte-Carlo techniques.

In order to determine the amount of continuity in the gas, the Knudsen number, K_n , is employed. The Knudsen number is a dimensionless quantity defined as $K_n = \frac{\lambda}{L}$, where λ is a mean free path and L is a characteristic length of the flow. For nitrogen gas, the maximum mean free path is approximately

$$\lambda_{max}(cm) \approx \frac{1}{n\pi\sigma^2}, \quad (4.1)$$

where $\sigma^2 = 14.9(10)^{-16}cm^2$ and n is the density of the gas in *molecules/cm³* [11]. The maximum mean free path of nitrogen versus the gas density is represented in figure 4.1. The choice of a characteristic length is nonspecific, so the radius of the nozzle is selected. Since the nozzle radius is not a constant, the local Knudsen number at some distance z from the nozzle entrance is defined as the mean free path evaluated at the centerline point at z divided by the radius of the nozzle at z . From the one-dimensional model, the mean free path can be estimated for the two-dimensional test case. The local Knudsen number is calculated, and is plotted for all points throughout the nozzle in figure 4.2.

According to Bird, [18], the Navier-Stokes equations can be used for flows which have Knudsen numbers of 0.1 or lower. For flows with greater Knudsen numbers, the Navier-Stokes equations break down and do not accurately represent the flow. Therefore, there is a lower limit as to what inlet density can be used. From figure 4.2 it can be seen that the test case lies within this region of usability, and the low stagnation pressure should not cause any significant problem. At most, the results obtained at the nozzle exit plane would be suspect.

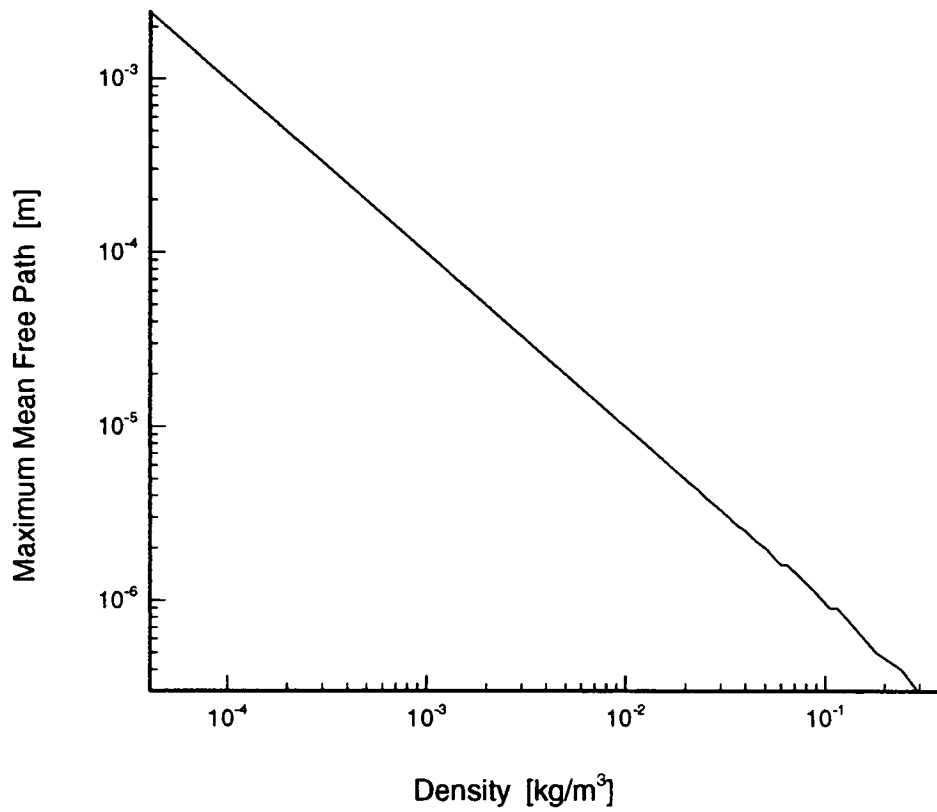


Figure 4.1. Maximum Mean Free Path for Nitrogen vs Distance from Inlet.

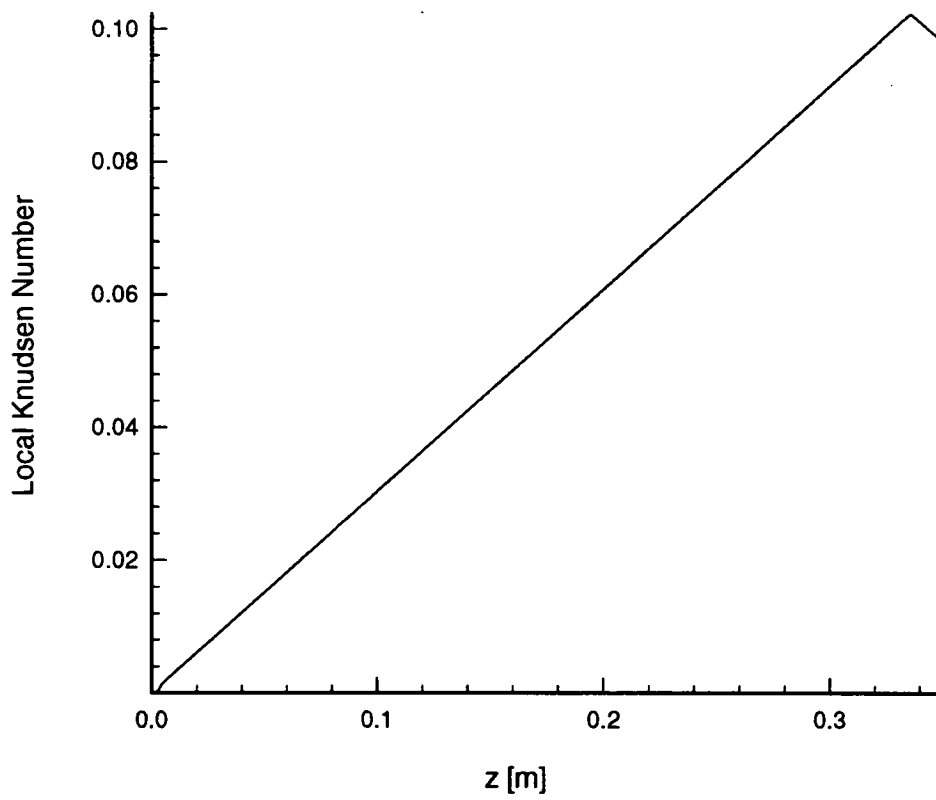


Figure 4.2. Local Knudsen Number vs Distance from Inlet.

4.3 Boundary Layer and Turbulence

Another consideration is the size of the boundary layer and the existence of turbulent behavior in the boundary layer. Boundary layers exist for viscous flows but the width of this layer is a function of the flow characteristics. The width, δ_{bl} , can be approximated by

$$\delta_{bl} \approx \left(\frac{C\mu}{\rho V} \right)^{\frac{1}{2}} = \frac{C}{(Re)^{\frac{1}{2}}}, \quad (4.2)$$

where C is a characteristic length [19]. Using the same argument as for Knudsen number, a local boundary layer width can be found as a function of position in the z -direction. As before, the radius of the nozzle is used for the characteristic length. Density, velocity, and viscosity values are evaluated at the centerline. Figure 4.3 represents the size of the boundary layer at all points along the nozzle. From this it can be seen that the width of the boundary layer is relatively small. Therefore, behavior in this region should be relatively isolated and should not have a pronounced effect on the majority of the flow.

Since turbulent behavior occurs in the boundary layer, turbulence modeling is not included in the model. The benefit of increased accuracy in the description of the flow, in such a small region, is not great enough to warrant the added complexity of the numerical model. However, it should be noted that Korte et al. found that not resolving the behavior at the throat affected the downstream Mach number (velocity) values [20]. Properly resolving this region, however, requires using a grid structure at the throat which is finer than usually used. Since the grid structure

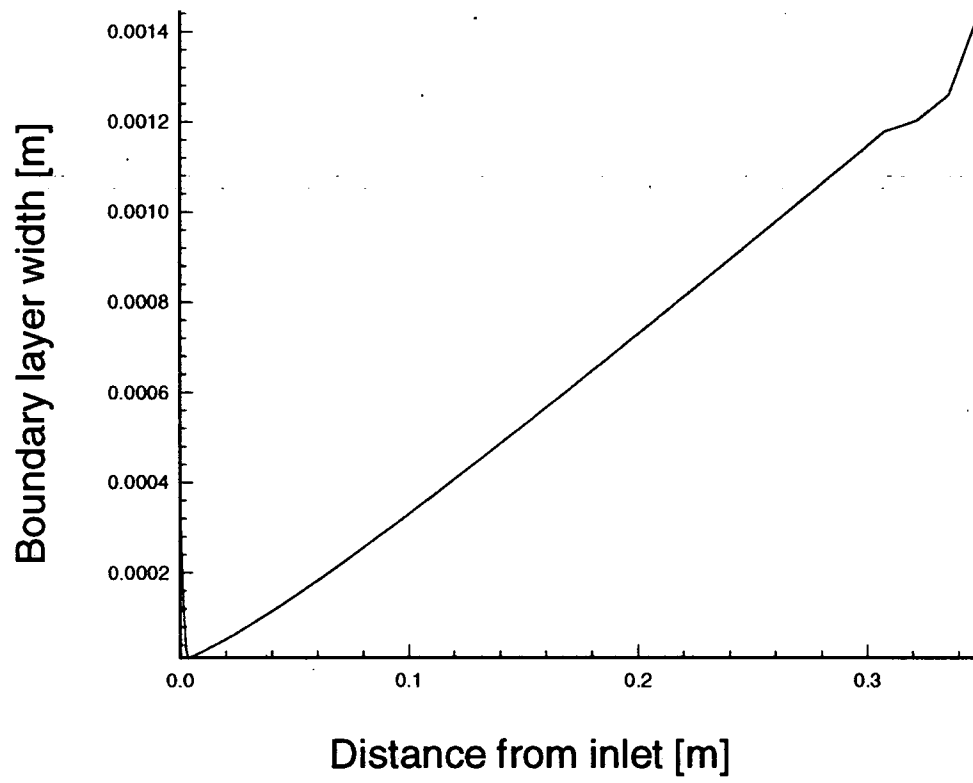


Figure 4.3. Boundary Layer Width vs Distance from Inlet.

in figure 3.1 has the greatest resolution at the throat, this may limit the growth of this problem.

Since the region outside the 'turbulent region' is usually treated as non-turbulent, and only matched to the turbulent region, it can be assumed that the overall effect on the near-centerline values is minimal. In terms of wind tunnel flow, it is not as much the behavior of the turbulent region that is of interest, but the spatial limits of the section with uniform flow.

4.4 Numerical Solutions

The solution of the test flow was determined for three separate cases. The first case was solved on a 81×41 grid (3321 points) using the implicit MacCormack method. Case two used a 81×41 grid and the Steger-Warming flux vector splitting method. The third case also used vector splitting but used a different wall boundary condition for the vibrational temperature. These three cases were compared with each other and with the solution of the one temperature, equilibrium model.

The first case, using the implicit MacCormack method, was run for 7000 iterations using a scaled time step of 1.0×10^{-3} . This translates to a total time of 7.0×10^{-7} s. Figures 4.4 through 4.15 are the set of contours for the set of six primitive variables. They also include enhancements of the throat region. Values stated below are centerline values.

In figures 4.4 and 4.5, the density is seen to fall off greatly from $.373 \text{ km}/\text{m}^3$ to $3.26 \times 10^{-5} \text{ km}/\text{m}^3$. This mirrors the pressure drop of 3.3×10^5 Pa (50 psi) to

1.08 Pa [figures 4.6 and 4.7]. The ratio of exit pressure to initial pressure is small enough so that a shock should not occur between the throat and the exit plane.

The radial velocity contours, figures 4.8 and 4.9, match intuitive expectations. The V_r values are negative before the throat (converging section) and positive after the throat (diverging section). The values are considerably less in magnitude compared to the axial velocity values, so they would not affect the vector value of total velocity. The absence of turbulence is also noticeable. This, however, is due to restrictions placed upon V_r in the numerical routine. Since the ΔU^{n+1} value calculated in the solution routine for V_r usually called for at least a 10^6 percent change in the V_r value, instabilities would arise not only in the boundary layer but also outside the boundary layer. Since the V_r values were relatively small, the need for numerical stability outweighed resolving the exact behavior of the V_r contours. Therefore, the V_r values were not allowed to change more than one hundred percent per iteration. This, of course, would limit the growth of turbulence.

The axial velocity contours, figures 4.10 and 4.11, showed that the velocity increased from 6 m/s to 2837 m/s. The flow is uniform with almost linear contours throughout most of the nozzle, and then rapidly decreasing in the boundary layer to satisfy the no-slip condition. The size of the boundary layer is small as expected, and causes no apparent problems.

The translational-rotational temperature falls sharply after the throat which is expected since the pressure is also dropping [figures 4.12 and 4.13]. At the far field boundary, the exit temperature is $112.07^\circ K$. This, along with the low pressure,

still represents gaseous nitrogen. Boundary behavior is very noticeable. It is the same size as the boundary layer seen the V_z contour. The temperature is increasing to the wall. To understand why this occurs, note the equilibrium energy equation

$$\rho \frac{\partial e}{\partial t} + \rho V \cdot \nabla e + P \nabla \cdot V + \nabla \cdot q + \Phi = 0. \quad (4.3)$$

For the values at the wall, the no-slip condition makes $V_r = V_z = 0$, so the viscous dissipation terms and pressure drop terms are zero. Equation (4.3) then becomes

$$\rho \frac{\partial e}{\partial t} = -\nabla \cdot q. \quad (4.4)$$

Since $\nabla \cdot q = -\nabla \cdot (K \nabla T)$, where K is the thermal conductivity, equation (4.4) can be written as

$$\frac{\partial e}{\partial t} = \nabla \cdot (K \nabla T). \quad (4.5)$$

If it is assumed that the equilibrium temperature, T , decreases at the wall, then ∇T is negative, so the internal energy would decrease. This would imply that the temperature would also decrease. However, the translational-rotational energy equation from the nonequilibrium model at the wall boundary, differs due to the coupling term,

$$\rho \frac{\partial e_{rt}}{\partial t} = \nabla \cdot (K \nabla T) - \rho C_{vv} X. \quad (4.6)$$

This can be written as

$$\rho \frac{\partial e_{rt}}{\partial t} = \nabla \cdot (K \nabla T) - \rho \left(\frac{e_v(T) - e_v(T_v)}{T} \right). \quad (4.7)$$

Since $T < T_v$ and $T > 0$, the difference in the last term of equation (4.7) is negative, so

$$\rho \frac{\partial e_{rt}}{\partial t} = \nabla \cdot (K \nabla T) + \rho |C_{vv} X|. \quad (4.8)$$

The coupling term increases the internal energy. If this term dominated the heat loss term, then one should see an increase in the internal energy and, therefore, an increase in the translational-rotational temperature. This would cause the gradient of T in the r direction to be positive and $\nabla \cdot (K \nabla T)$ would not necessarily be negative or at least would be less negative. Thus, numerically, one effect would create and encourage the other. Physically, this effect is still meaningful. As the gas slows at the wall, there is more time for the gas to relax. More relaxation translates into a greater transfer of vibrational to translational-rotational energy. This would cause an increase in the translational-rotational temperature.

The most notable feature of the vibrational temperature contours, figures 4.14 and 4.15, is the freezing of the vibrational temperature downstream of the throat. Also, the flow is not in equilibrium before the throat, as other authors have suggested reference [2]. The translational-rotational temperature drops much faster in the converging section than the vibrational temperature. Therefore, the assumption of equilibrium flow before the throat should not be used. In the boundary layer, the vibrational temperature decreases at the wall up to the 'freezing point'. After this point, the temperature freezes and the boundary behavior disappears. The decrease occurs due to the slow speed, which allows the vibrational temperature to relax and move closer to the translational-rotational temperature. The fact that this behavior

stops farther downstream may mean that the translational-rotational temperature is increasing faster than the vibrational temperature is decreasing.

Case two produced similar results. Using the Steger-Warming flux vector splitting, the shape and the values of the contours were nearly the same. The densities, figure 4.16, dropped from 0.371 kg/m^3 to $3.27 \times 10^{-5} \text{ kg/m}^3$. The pressure dropped from $3.3 \times 10^5 \text{ Pa}$ to 1.08 Pa [figure 4.17].

The radial and axial velocity contours, figures 4.18 and 4.19, also were nearly identical. The same restriction was applied to the V_r changes as in case one. The axial velocity increased to 2836 m/s , which differed case one by only one m/s .

The translational-rotational temperature [figure 4.20] dropped to $112.2 \text{ }^\circ \text{K}$. The vibrational temperature behaved similarly to case one [figure 4.21]. The vibrational temperature was in nonequilibrium before the throat and freezing occurred downstream of the throat as in case one. The freezing temperature was exactly the same as in case one. The only difference was the point of freezing, which was slightly further downstream.

Overall, the behavior was similar enough to validate the results in case one. This case also produced uniform flow. The freezing of the vibrational temperature in the boundary layer downstream of the throat reaffirms the idea that the translational-rotational temperature is increasing faster than the vibrational temperature is decreasing.

To remove the problems encountered in cases one and two, a third case is examined using different boundary conditions. The stagnation conditions and boundary

conditions were the same as the previous cases except at the wall boundary. At this boundary, only the condition on the vibrational temperature was changed. Since the gas is not moving at the wall, the energy must be in equilibrium. Therefore, the translational-rotational temperature and the vibrational temperature must be the same. To enforce this statement, the vibrational temperature is explicitly set equal to the translational-rotational temperature.

The contours for density [figure 4.22] showed that the density dropped from $.371 \text{ kg/m}^3$ to $3.25 \times 10^{-5} \text{ kg/m}^3$. The pressure [figure 4.23] dropped equivalently from $3.3 \times 10^5 \text{ Pa}$ to 1.08 Pa .

A main difference in this case was the radial velocity [figure 4.24], which showed some turbulent behavior. This turbulence begins at the nozzle throat within the boundary layer region. Downstream the effects are less noticeable. This is the behavior that was expected for the boundary layer region.

The axial velocity [figure 4.25] contours were similar to cases one and two. The velocities rise steadily from 6 m/s to 2850 m/s , which was higher than the other cases. The contours are uniform throughout the nozzle.

The translational-rotational temperature [figure 4.26] drops from $3000 \text{ }^\circ \text{K}$ to $112.1 \text{ }^\circ \text{K}$. In the boundary layer region, the temperature still increases, but much less severely. The vibrational temperature [figure 4.27] freezes at the same frozen temperature as in cases one and two, but the boundary layer behavior is different. The vibrational temperature drops to the value of the translational-rotational temperature on the wall boundary. Thus, the boundary behavior which stops at the

throat for the other cases, now continues to the nozzles exit plane. This is the result that was expected. Therefore, the change in boundary conditions significantly improved the results.

For comparison purposes, the results of the three cases were compared to the results of a nitrogen flow with the same stagnation conditions but with the unrealistic assumption of forced thermal equilibrium [21]. Figure 4.28 shows the difference between the centerline values for the equilibrium temperature compared to the centerline values for the two temperatures found in case one. The actual measurements of T_v are difficult in a laboratory situation, since the gas would equilibrate upon contact with a temperature sensor. Therefore, it would be useful to convert the translational-rotational temperature and the vibrational temperature into a single temperature that could actually be measured. Park suggested a geometric average $T_{rt}^\alpha T_v^{\alpha-1} = T_{avg}$, where $0 \leq \alpha \leq 1$, in order to calculate reaction rates [22]. This is just a rough estimate, so it is not used here.

Other differences between case one and the equilibrium model results were the absence of boundary layer behavior for temperature, and an increased axial velocity for the equilibrium model. In this model, the exit velocity was 2900 m/s. This increased value may have been due to an improperly imposed conservation of mass flow condition in that program. That model also predicted uniform flow.

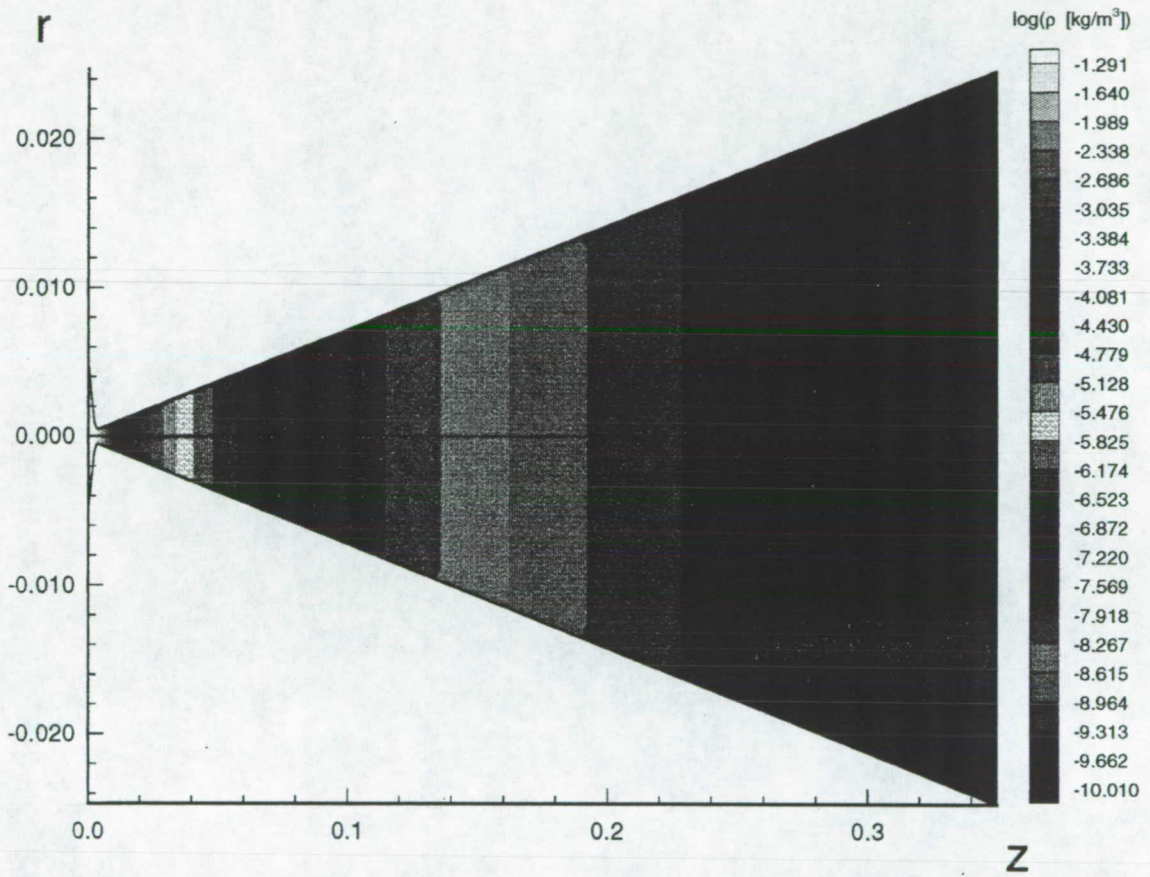


Figure 4.4. Case One: Logarithm of Density Contours.

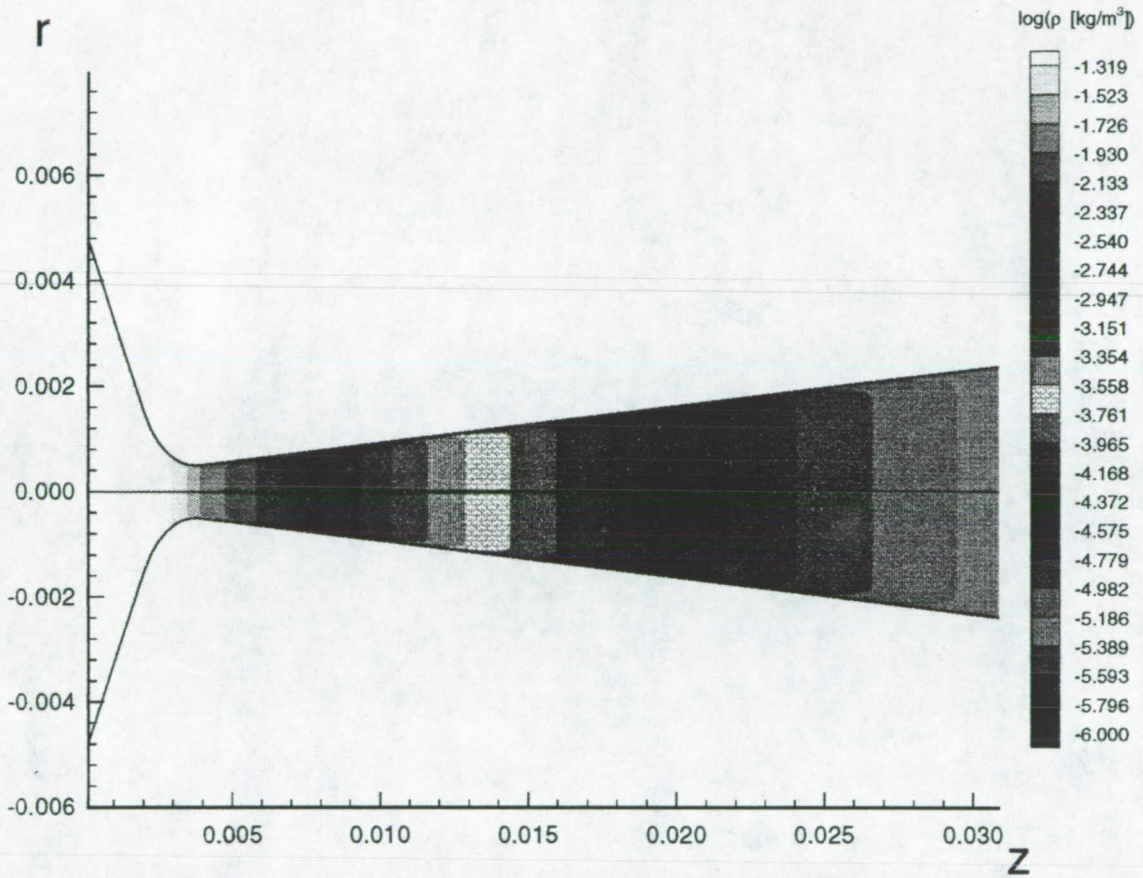


Figure 4.5. Case One: Logarithm of Density Contours (throat region).

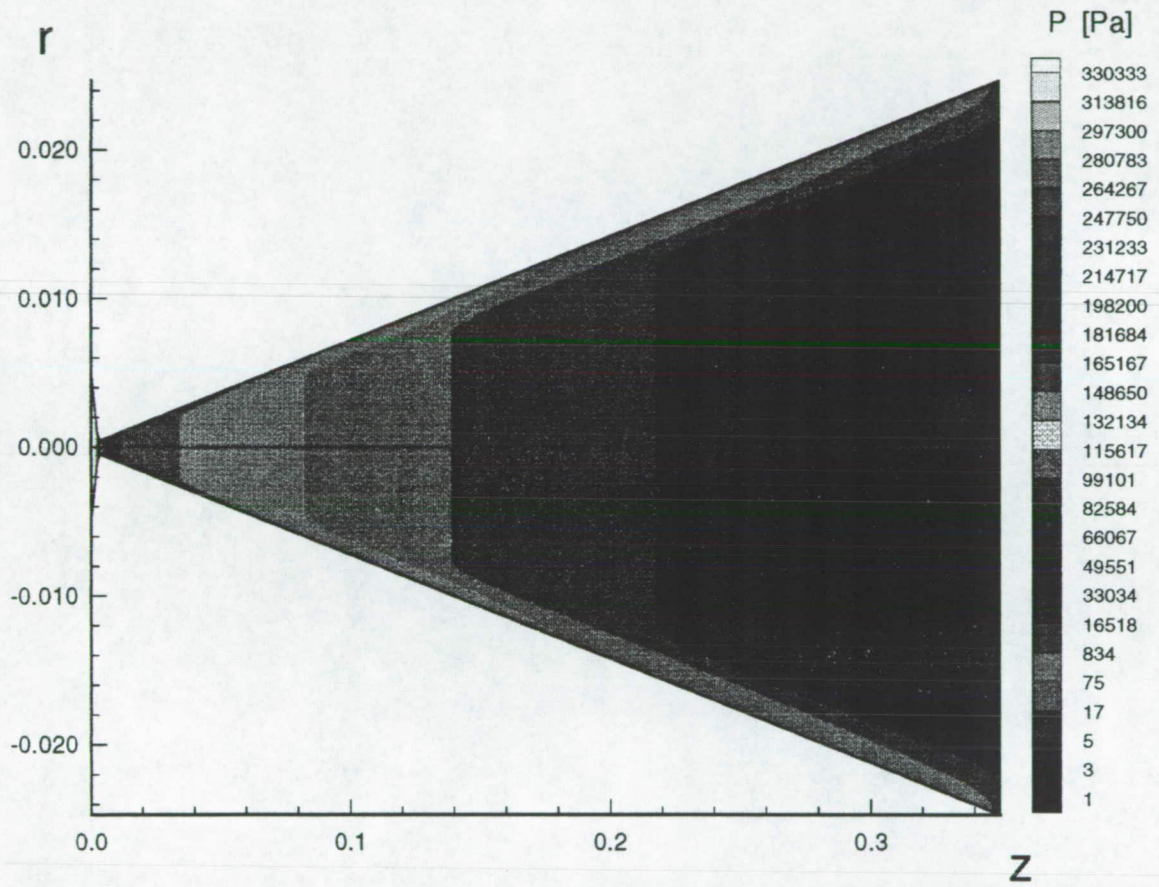


Figure 4.6. Case One: Pressure Contours.

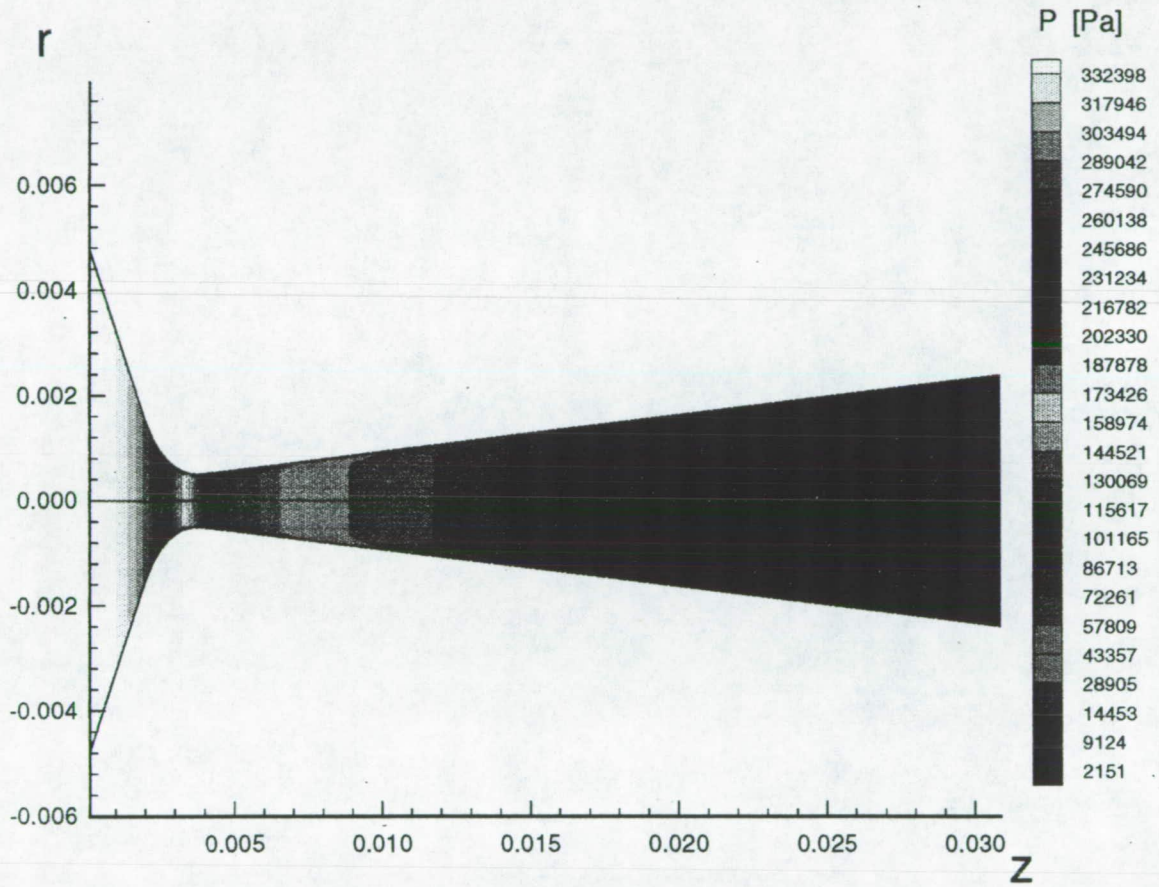


Figure 4.7. Case One: Pressure Contours (throat region).

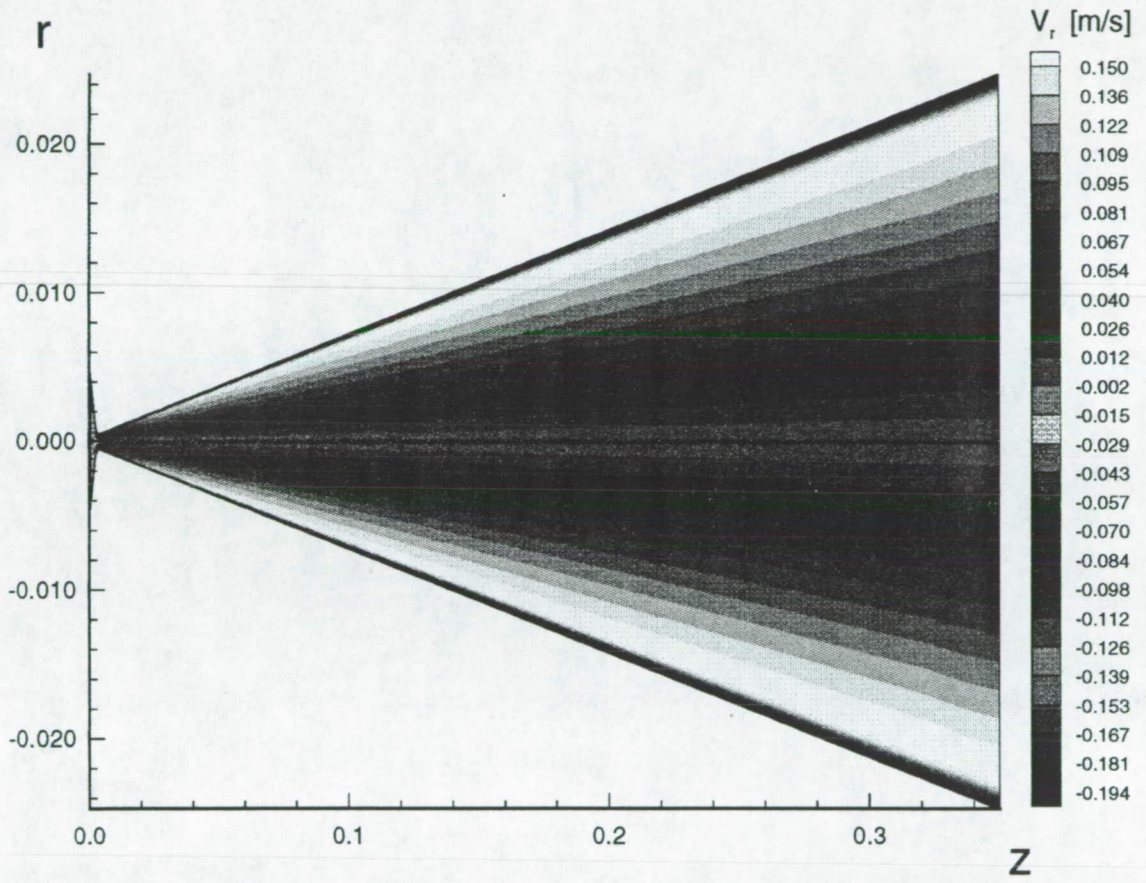


Figure 4.8. Case One: Radial Velocity Contours.

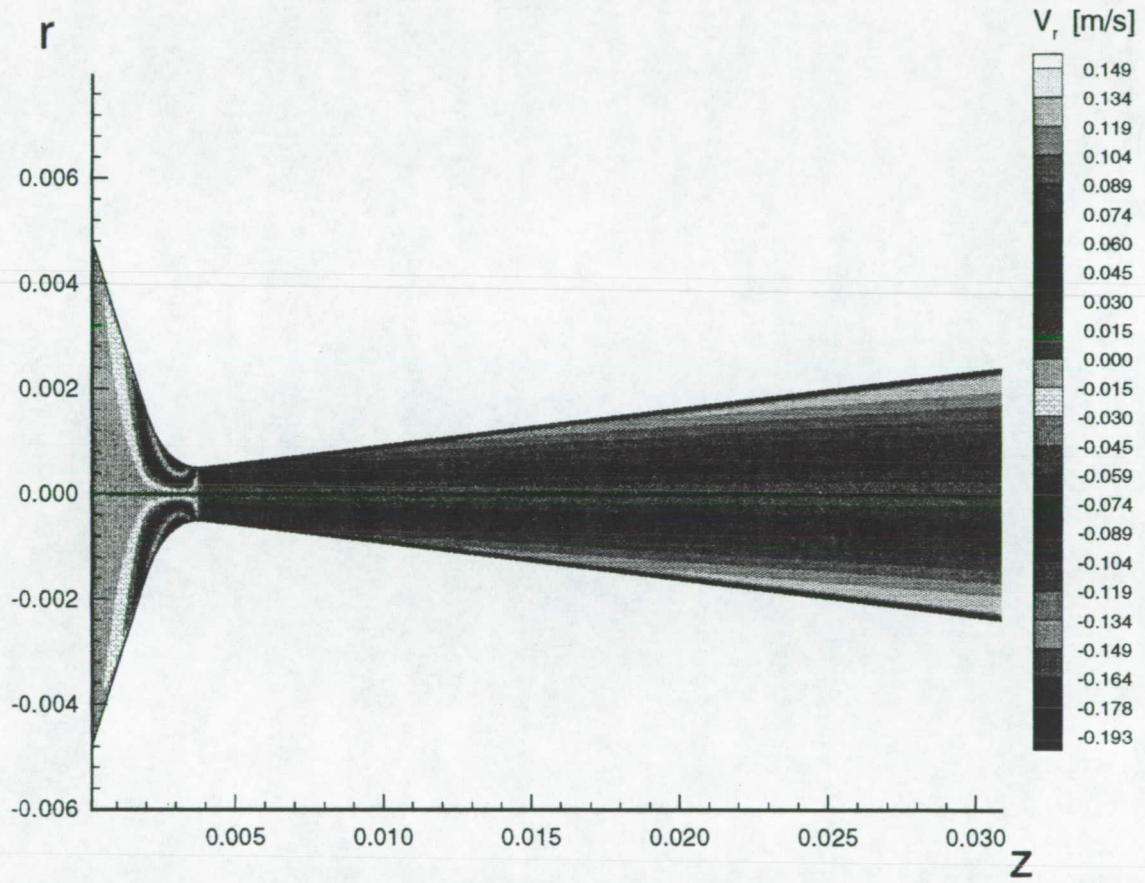


Figure 4.9. Case One: Radial Velocity Contours (throat region).

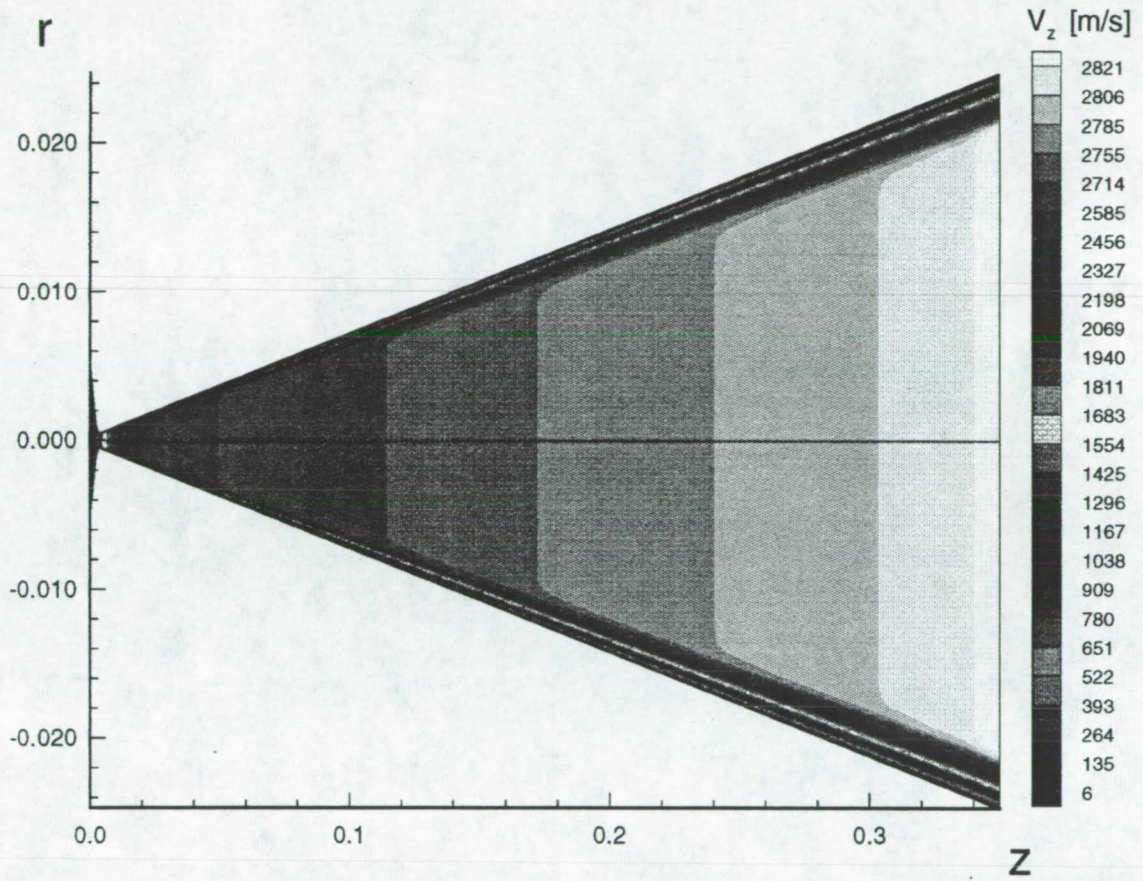


Figure 4.10. Case One: Axial Velocity Contours.

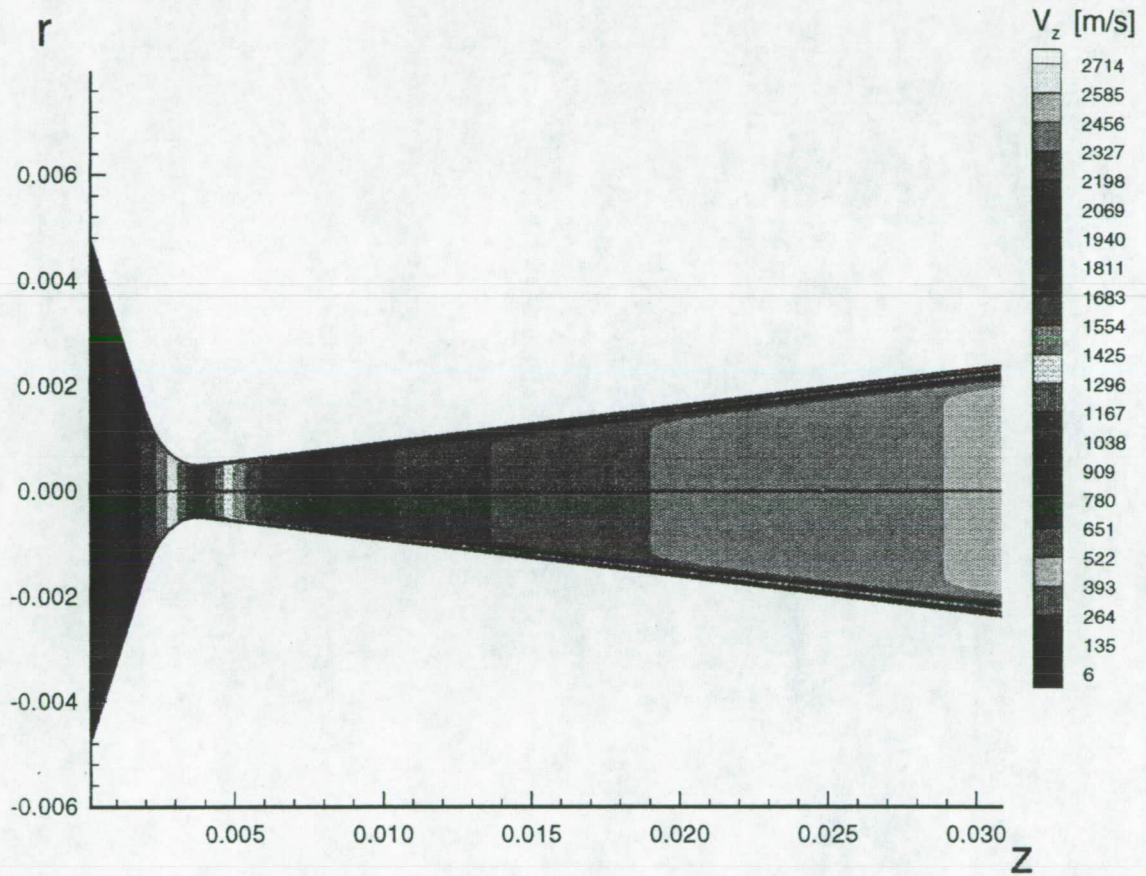


Figure 4.11. Case One: Axial Velocity Contours (throat region).

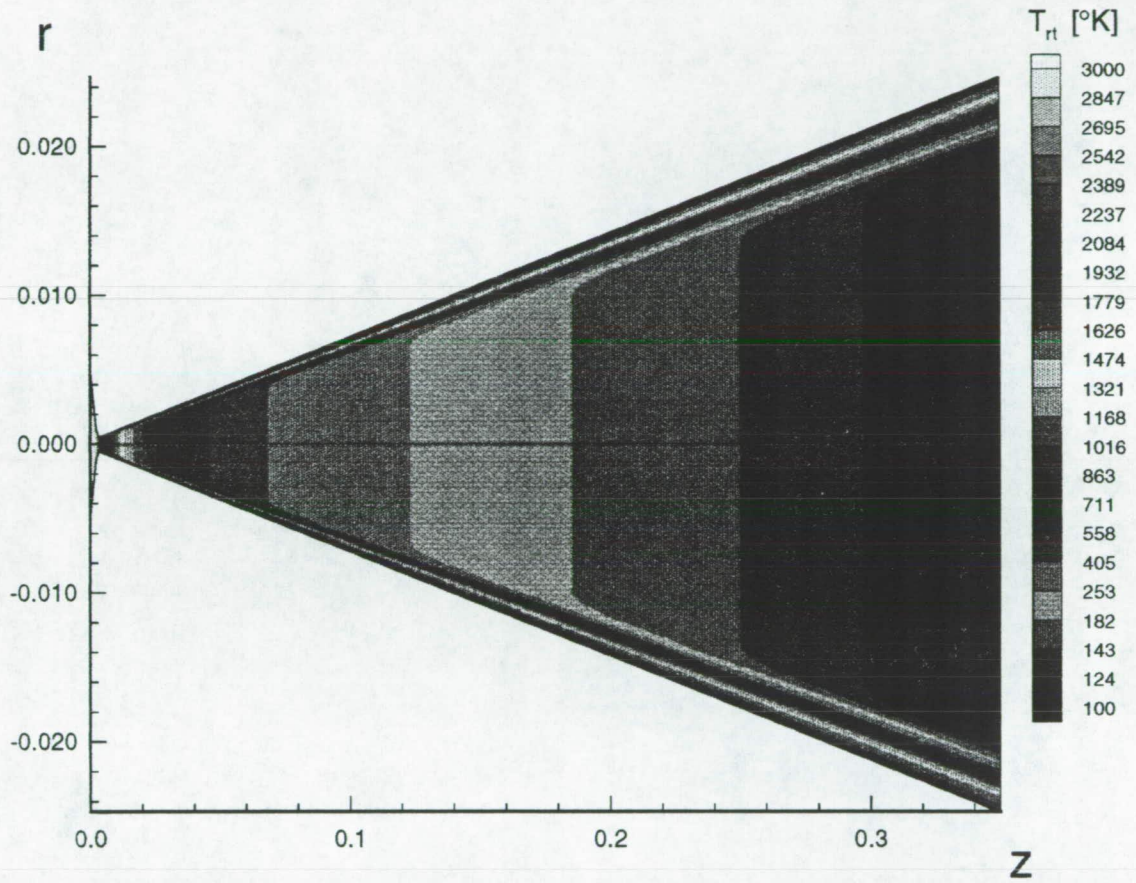


Figure 4.12. Case One: Translational-rotational Temperature Contours.

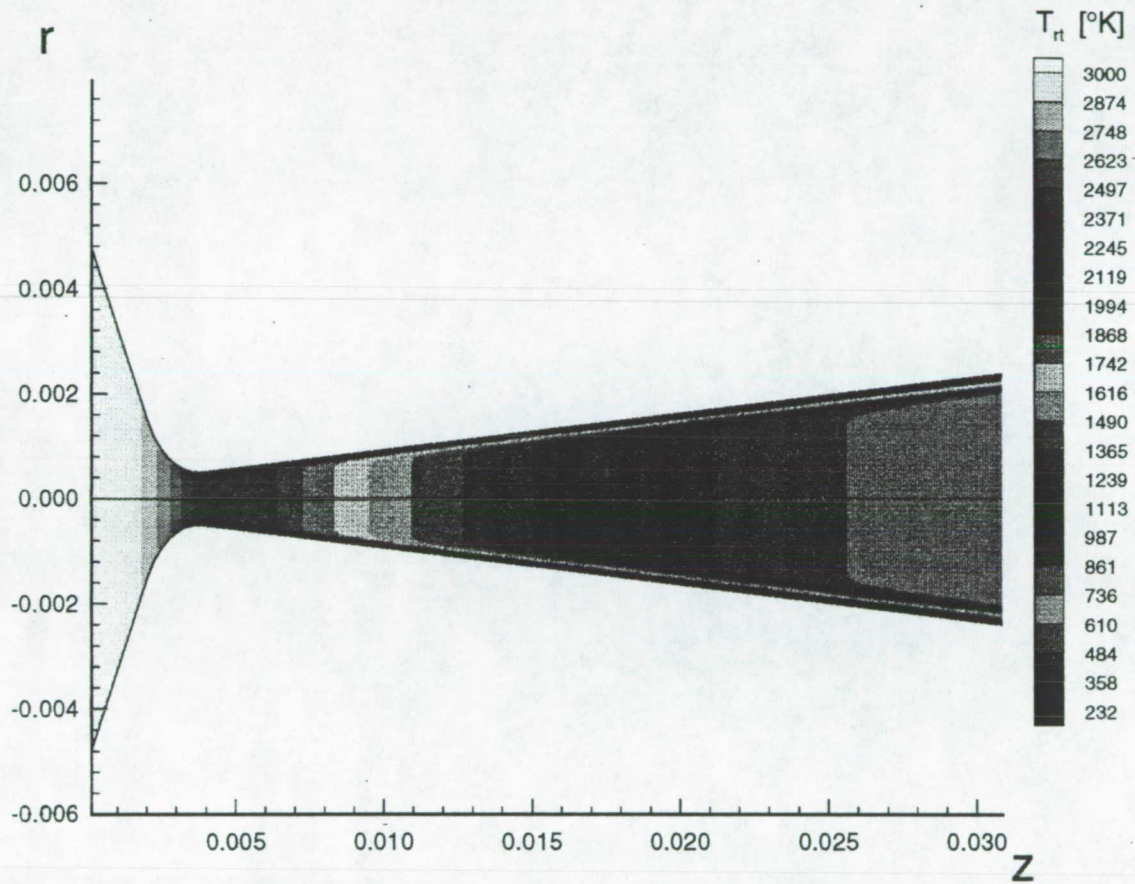


Figure 4.13. Case One: Translational-rotational Temperature Contours (throat region).

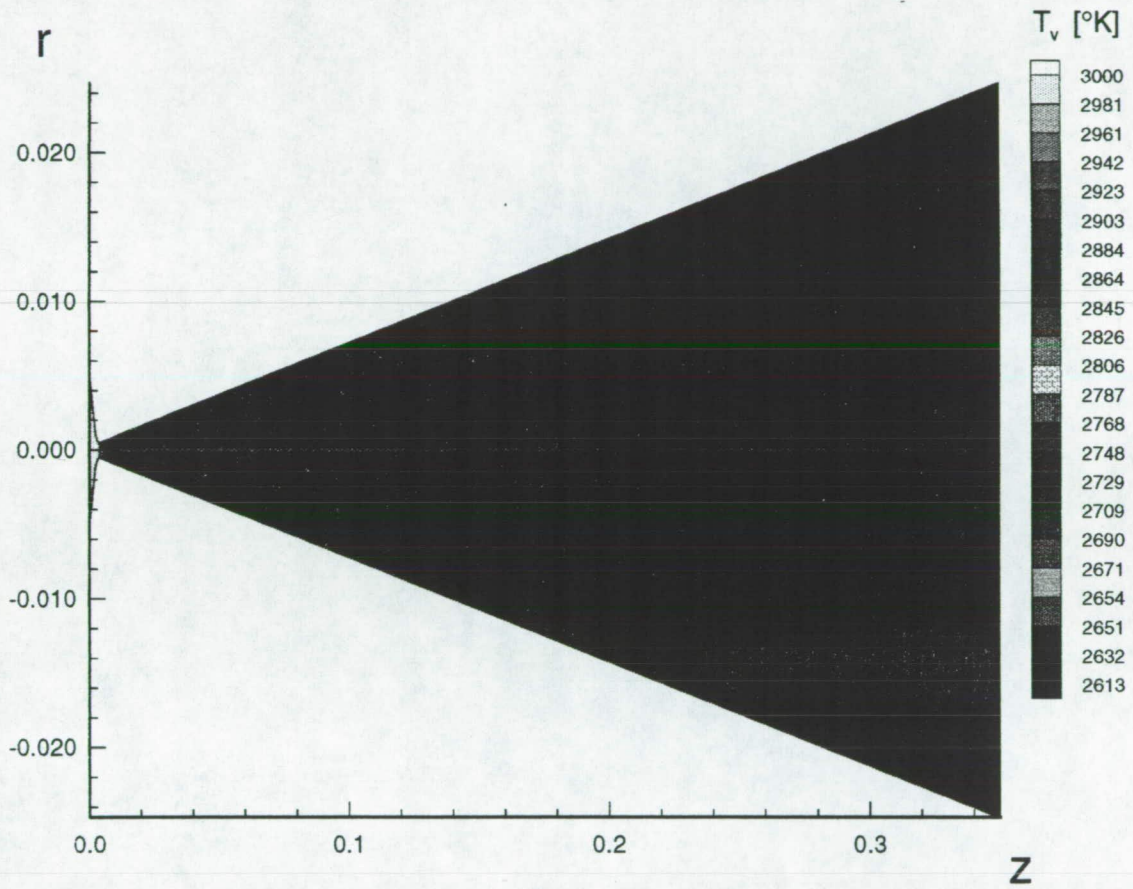


Figure 4.14. Case One: Vibrational Temperature Contours.

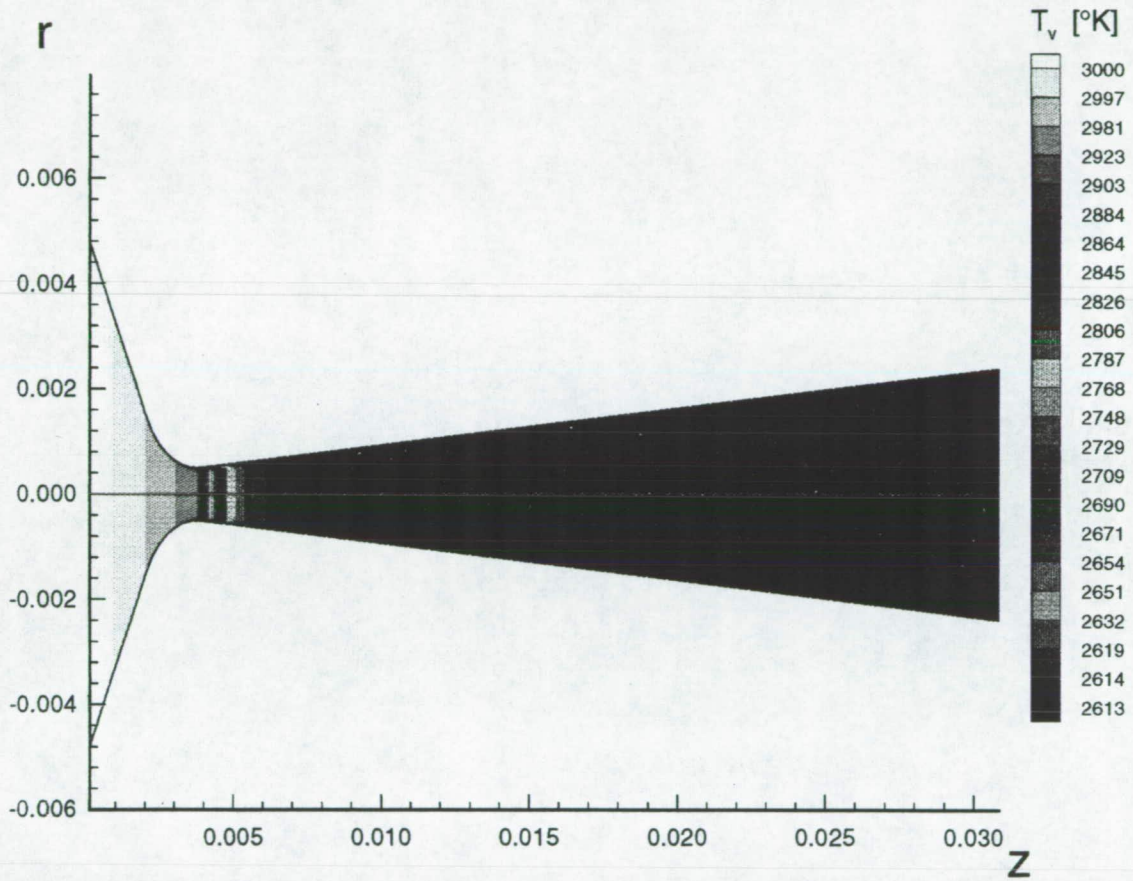


Figure 4.15. Case One: Vibrational Temperature Contours (throat region).

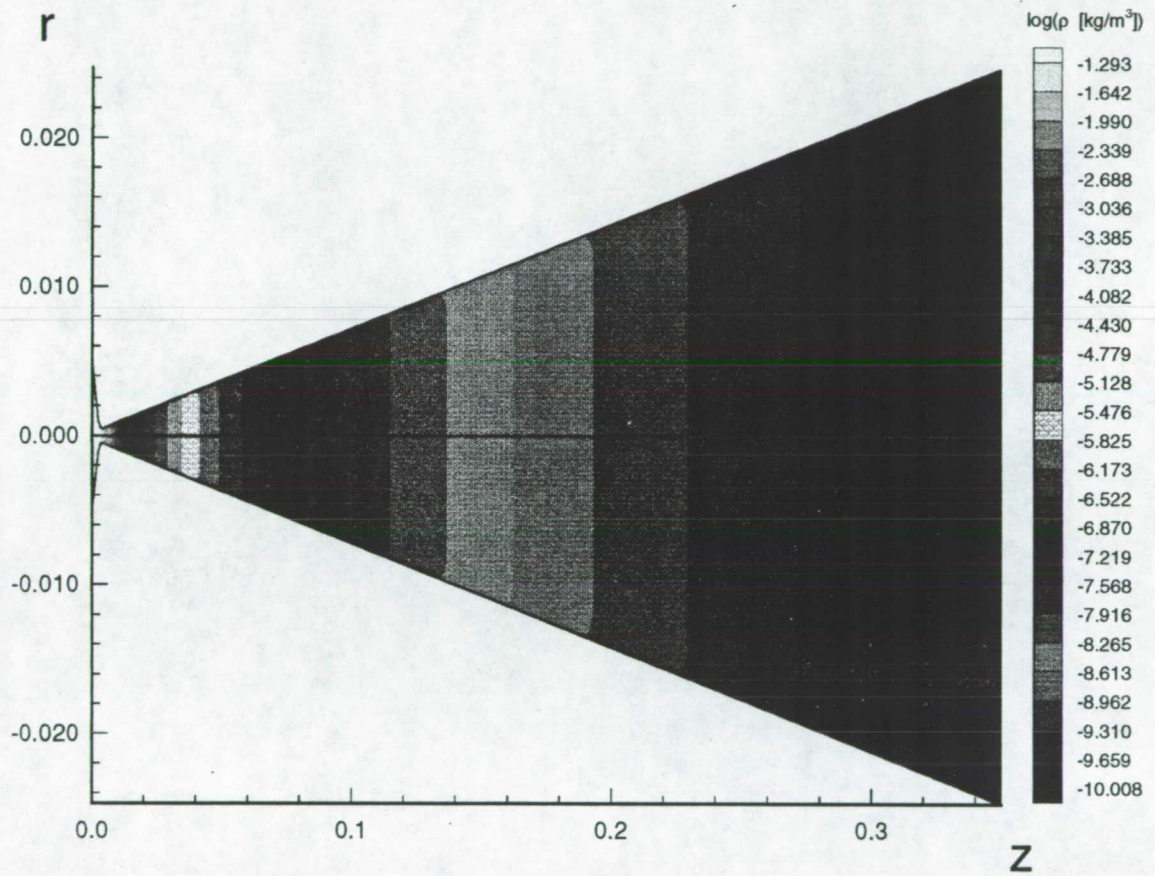


Figure 4.16. Case Two: Logarithm of Density Contours.

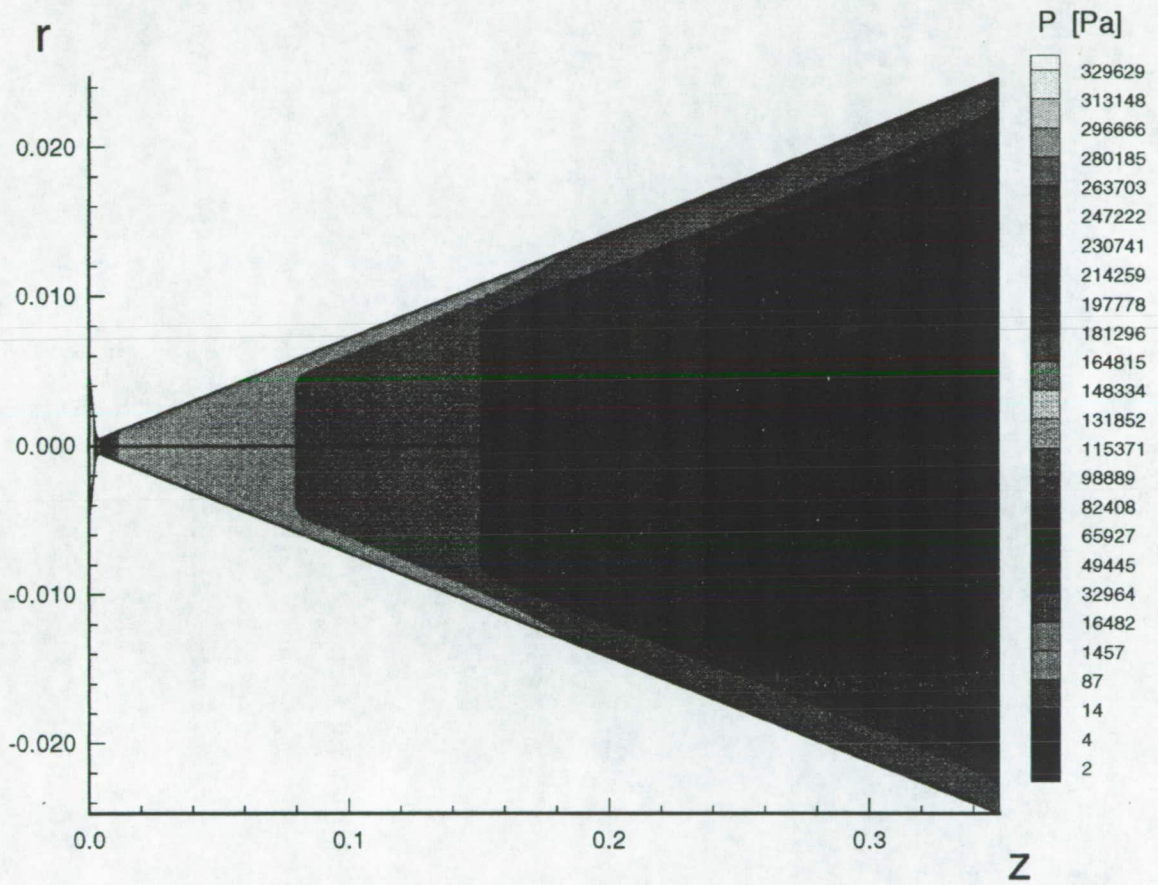


Figure 4.17. Case Two: Pressure Contours.

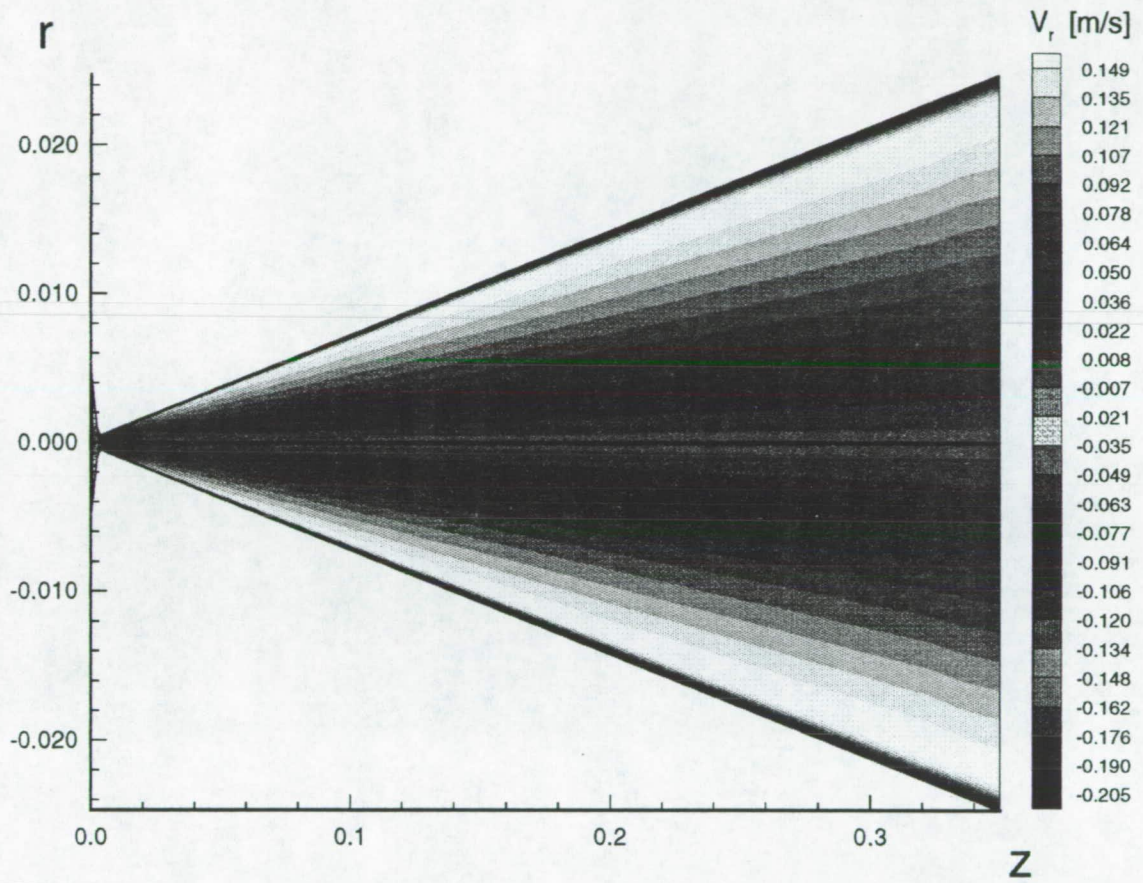


Figure 4.18. Case Two: Radial Velocity Contours.

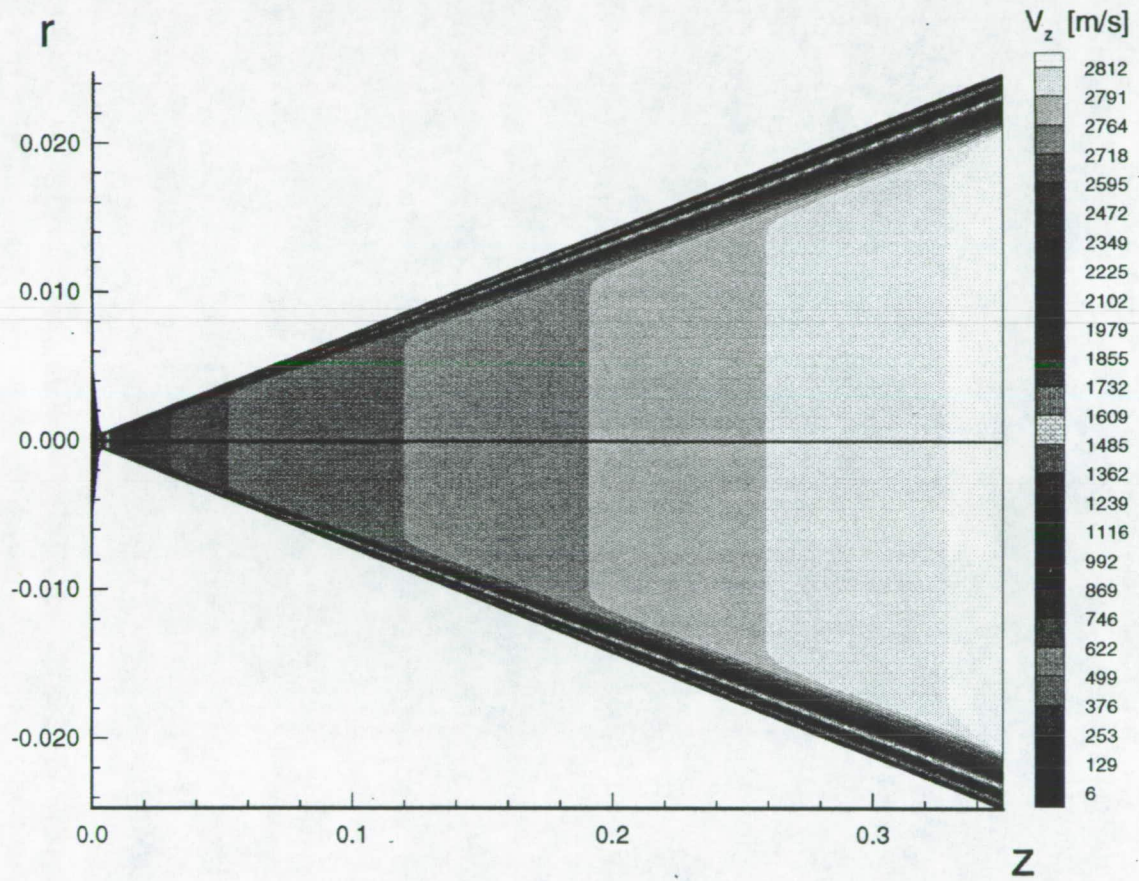


Figure 4.19. Case Two: Axial Velocity Contours.

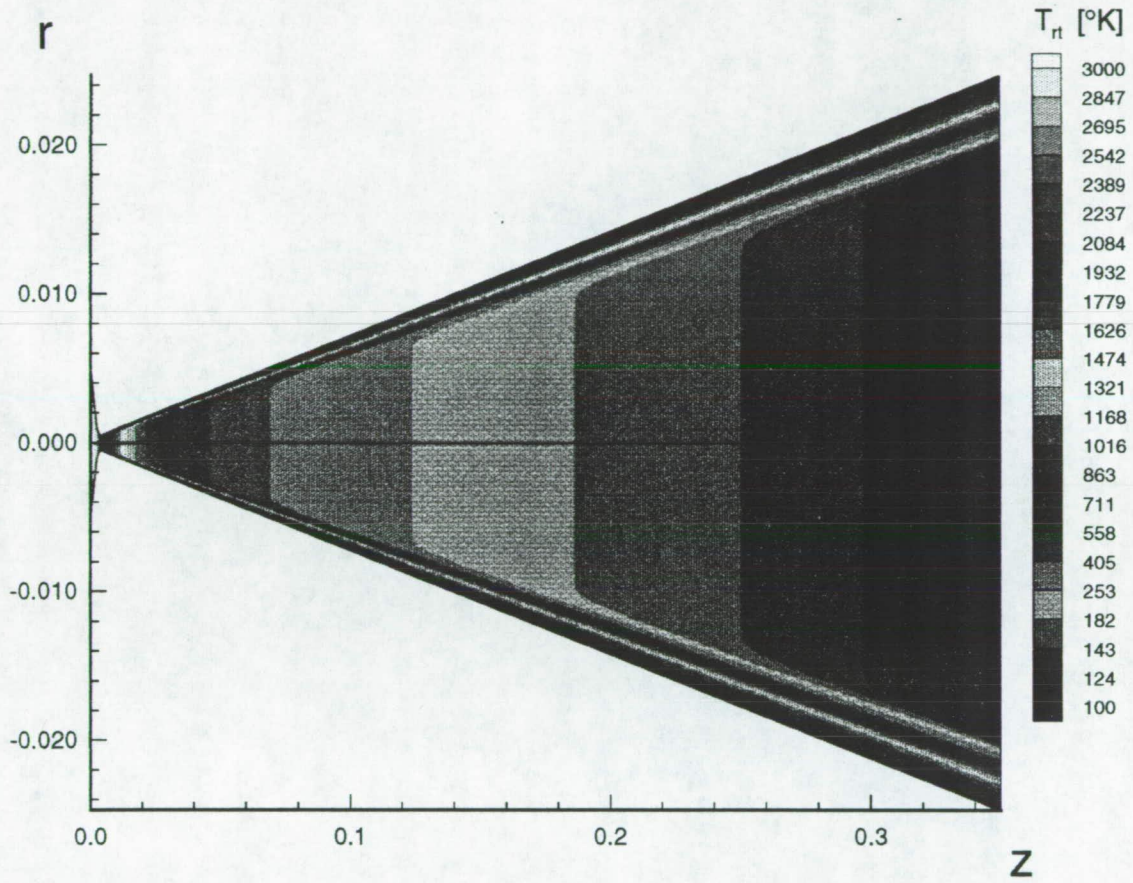


Figure 4.20. Case Two: Translational-rotational Temperature Contours.

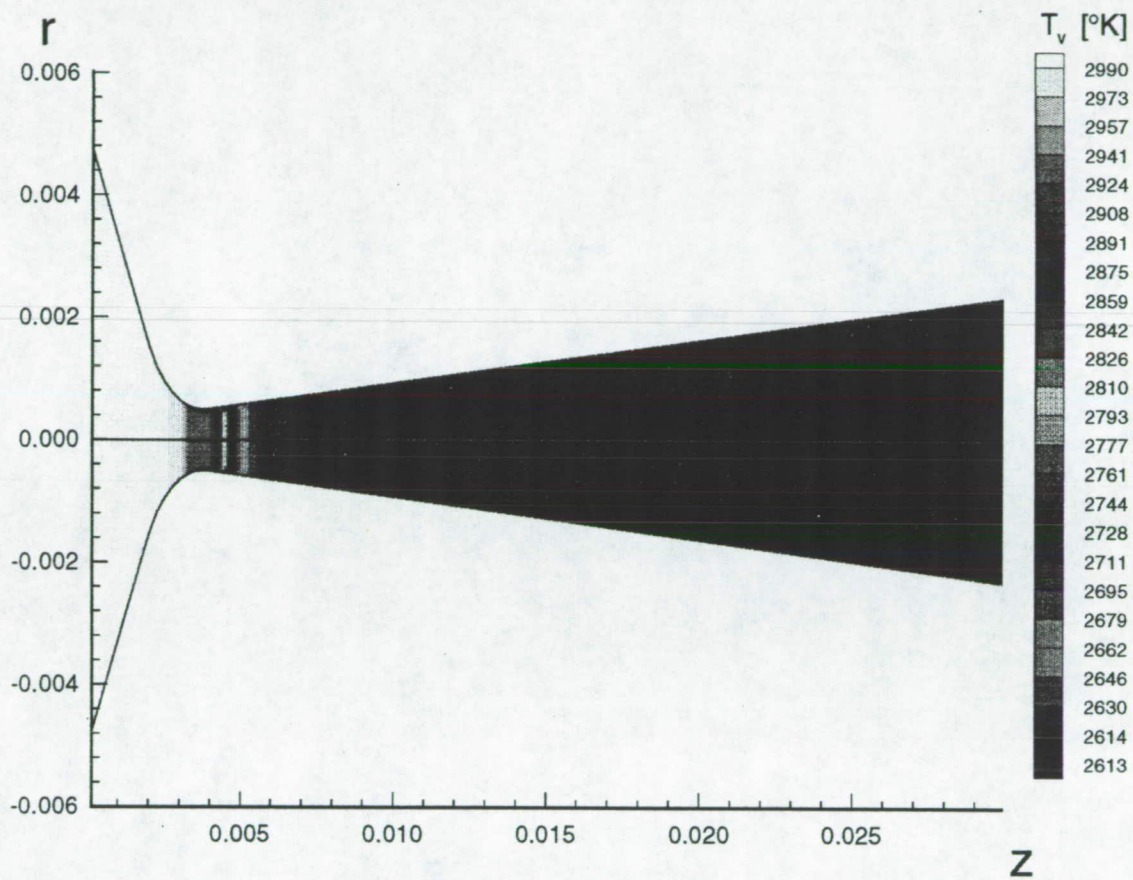


Figure 4.21. Case Two: Vibrational Temperature Contours (throat region).

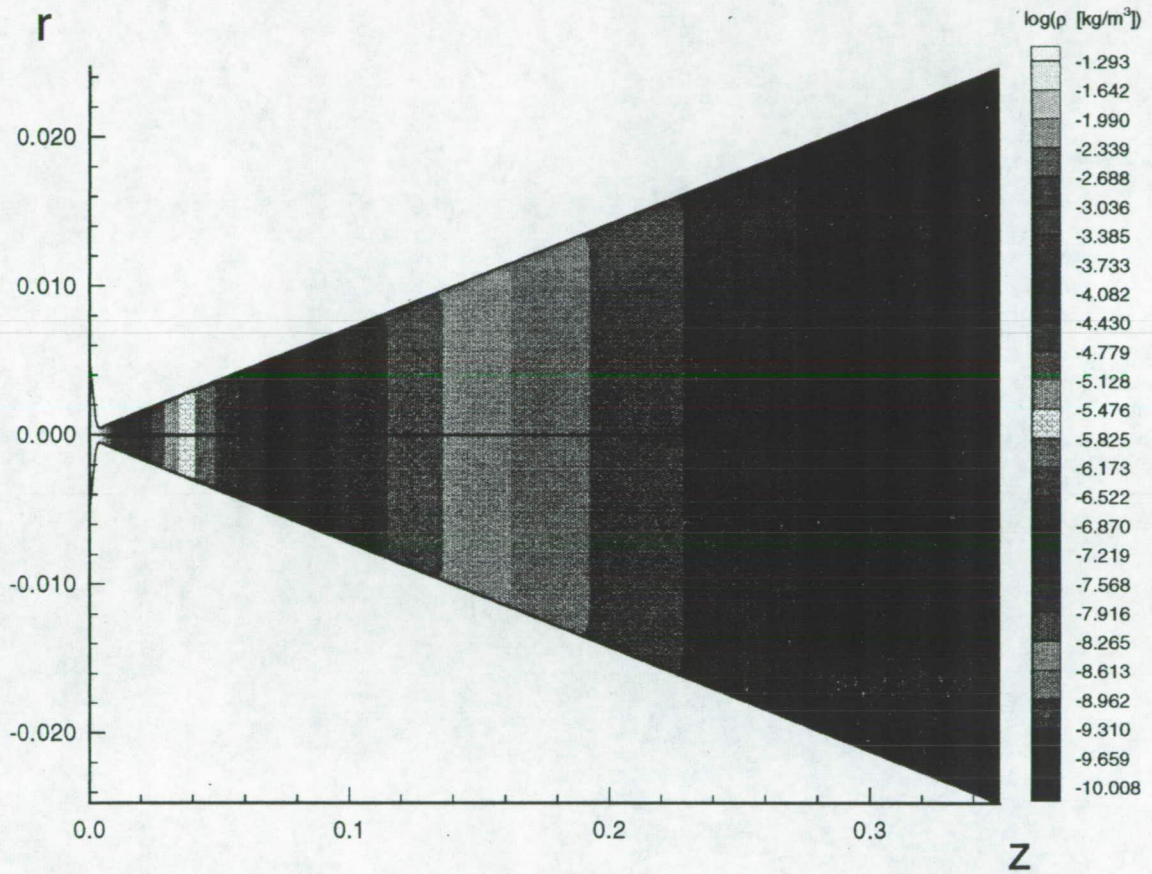


Figure 4.22. Case Three: Logarithm of Density Contours.

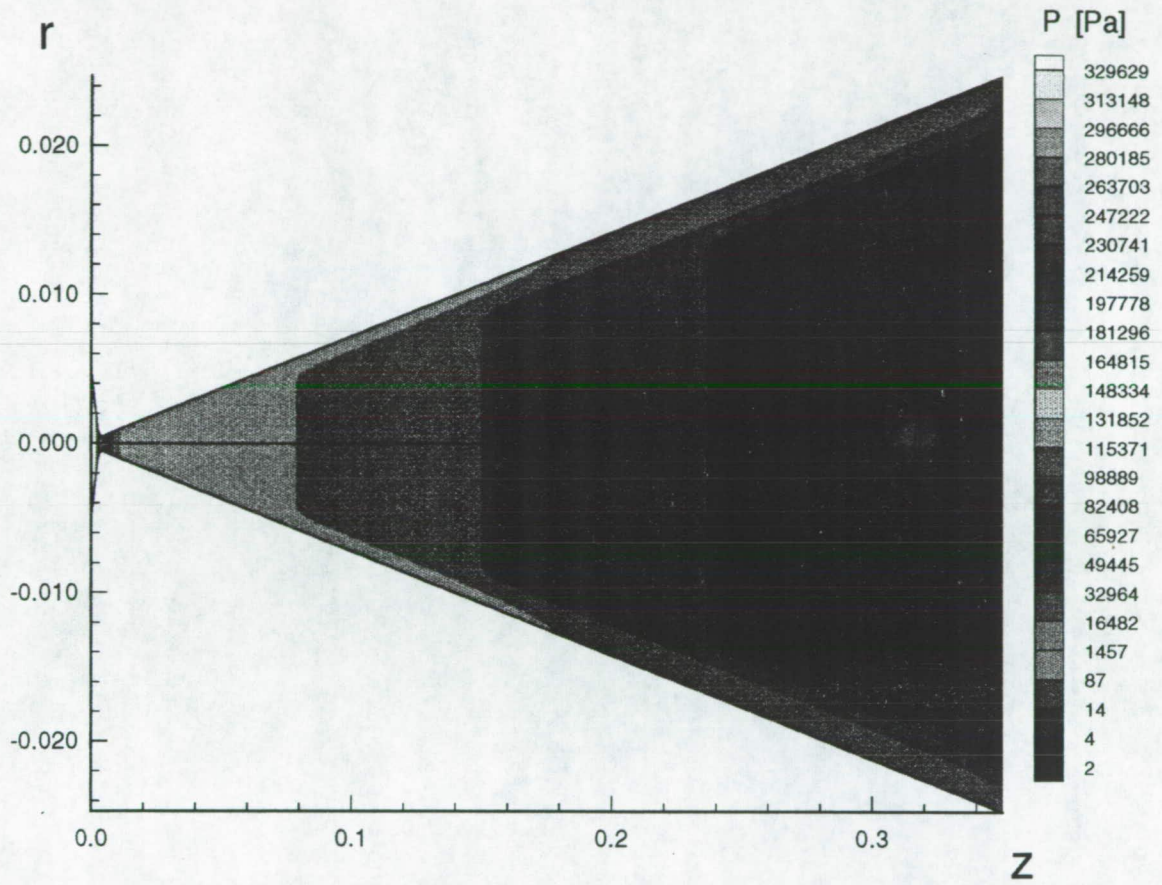


Figure 4.23. Case Three: Pressure Contours.

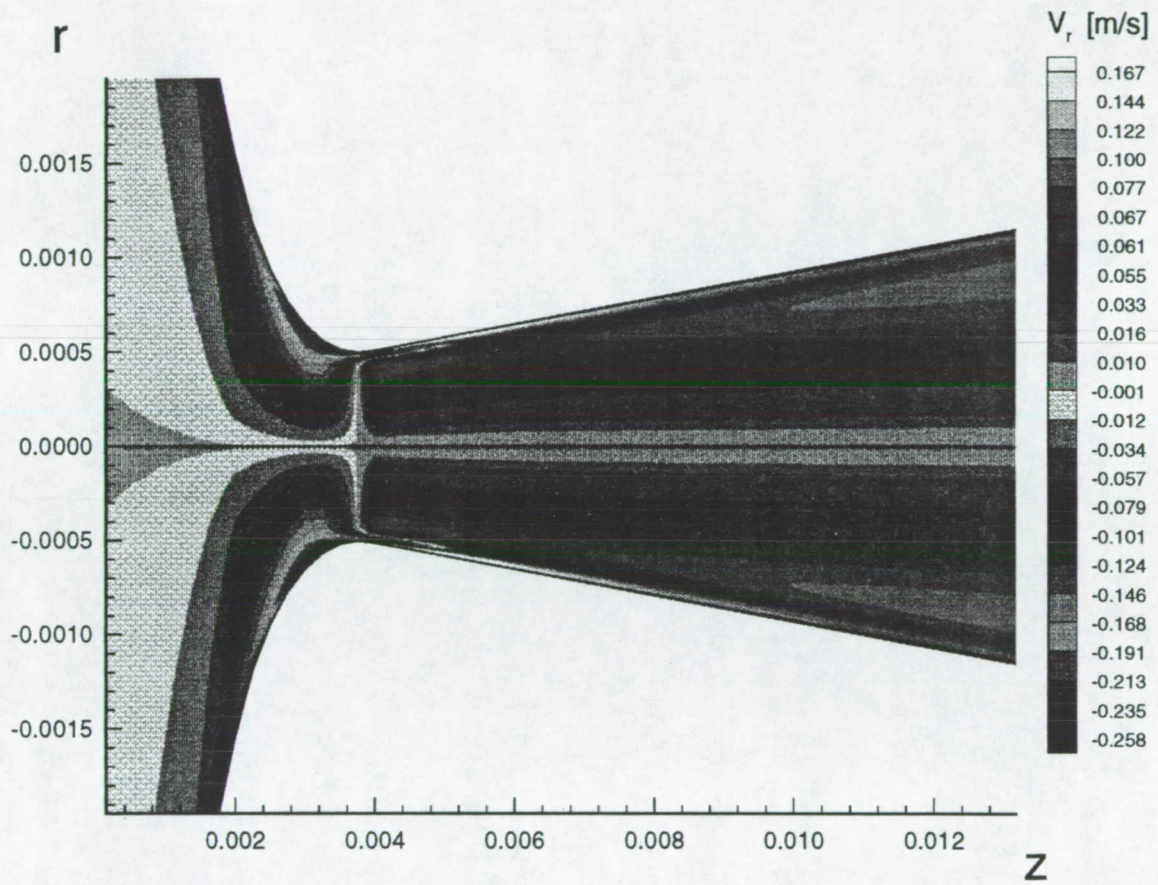


Figure 4.24. Case Three: Radial Velocity Contours (throat region).

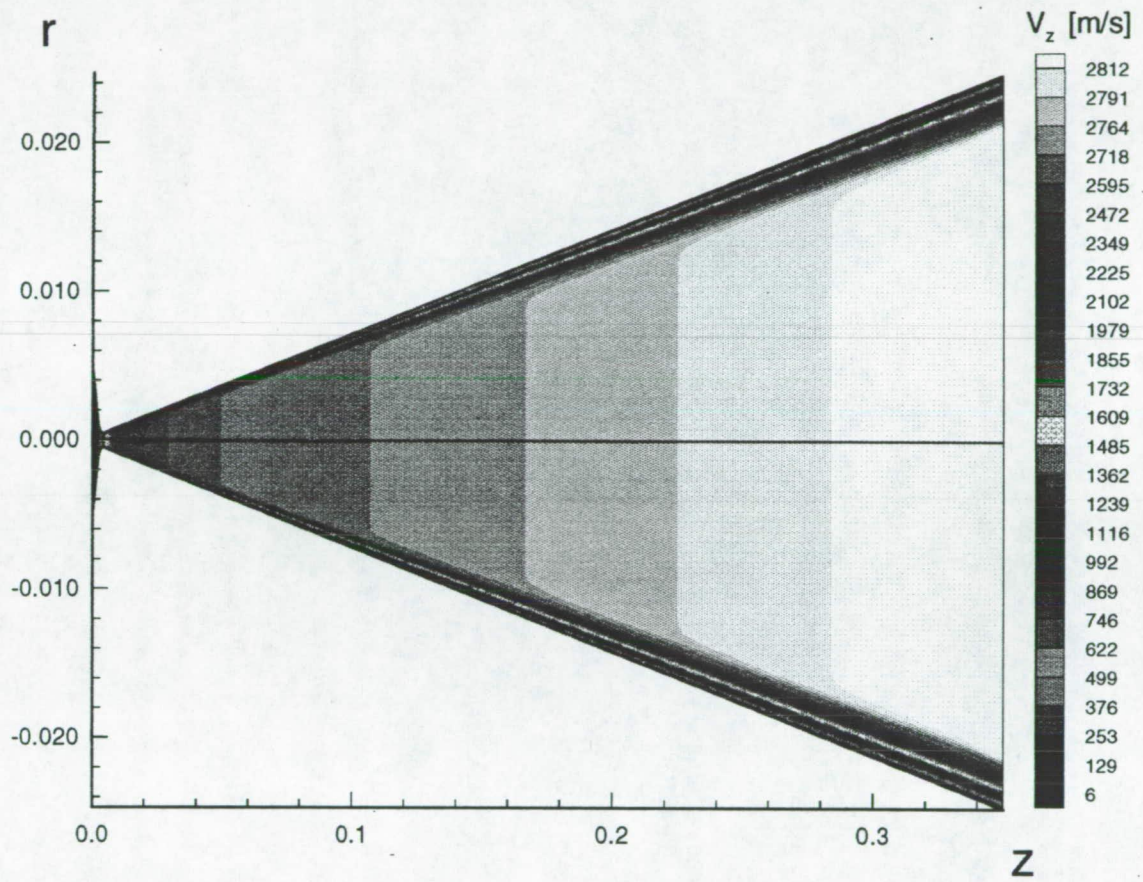


Figure 4.25. Case Three: Axial Velocity Contours.

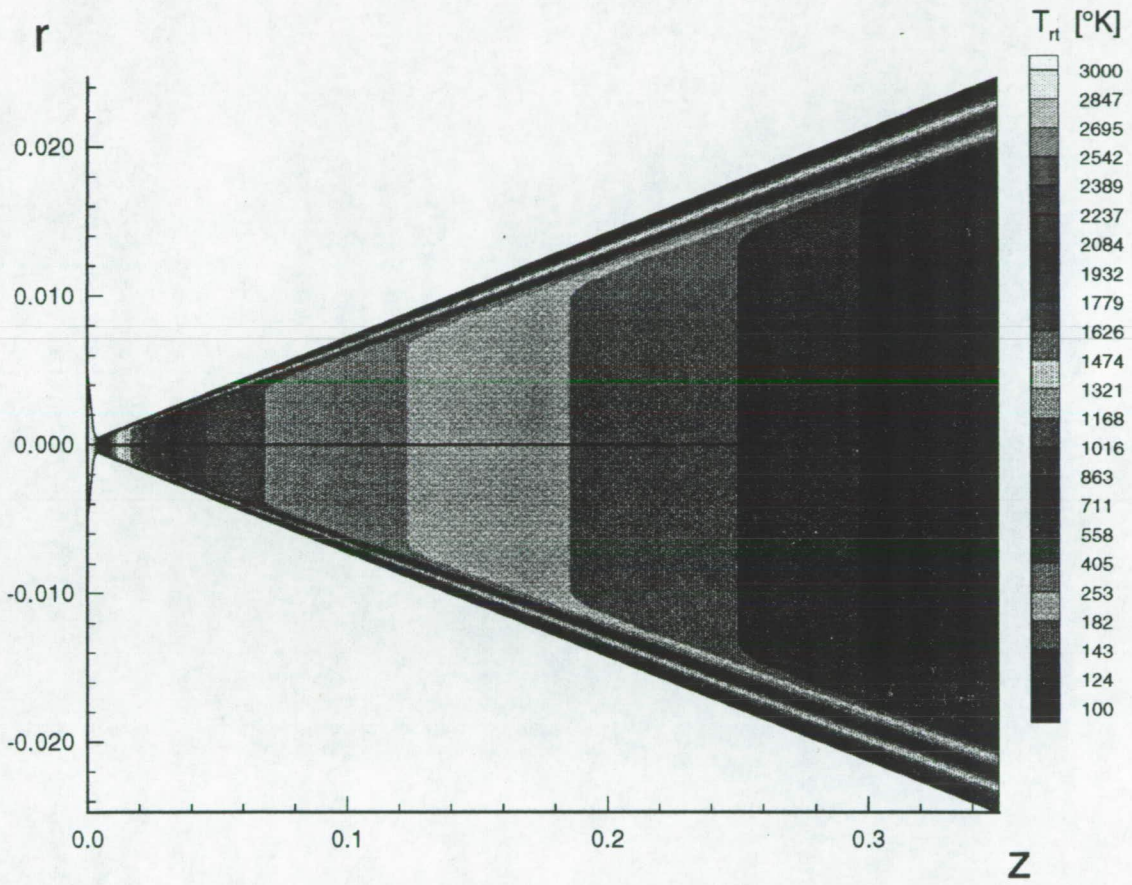


Figure 4.26. Case Three: Translational-rotational Temperature Contours.

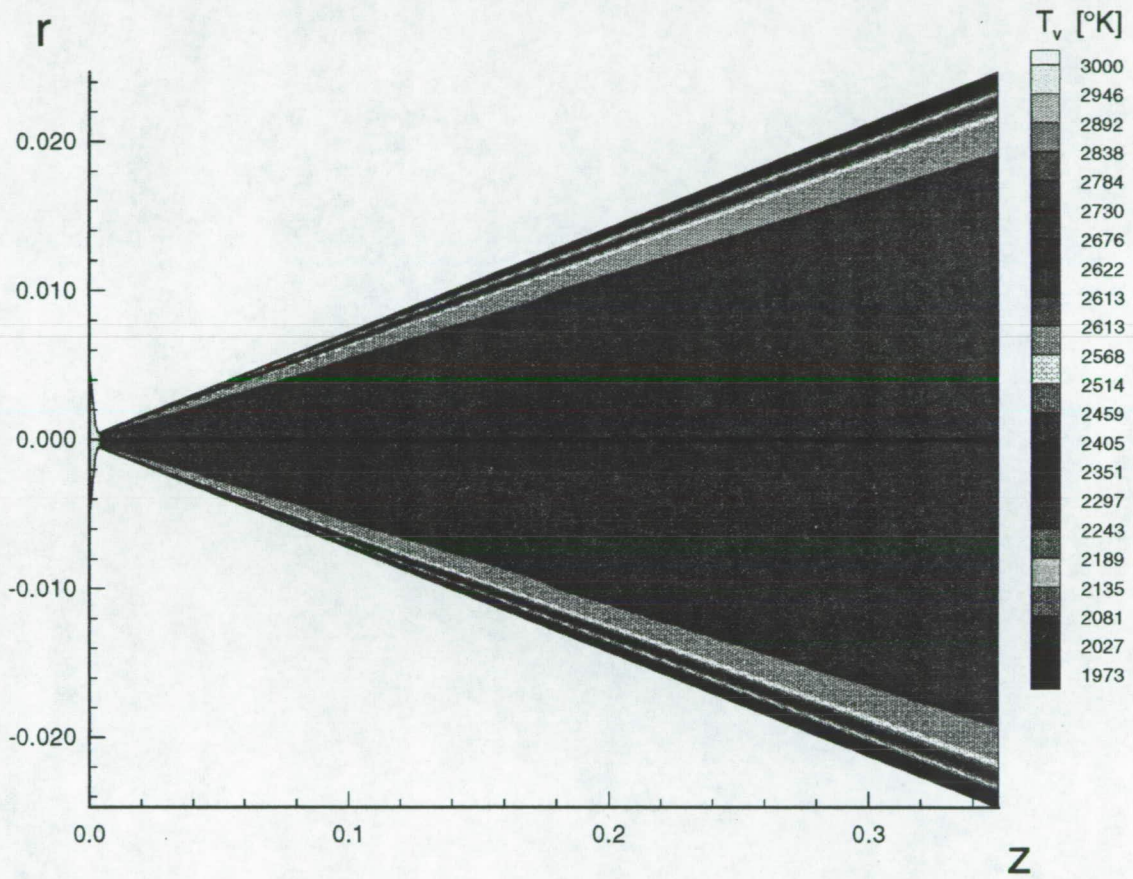


Figure 4.27. Case Three: Vibrational Temperature Contours.

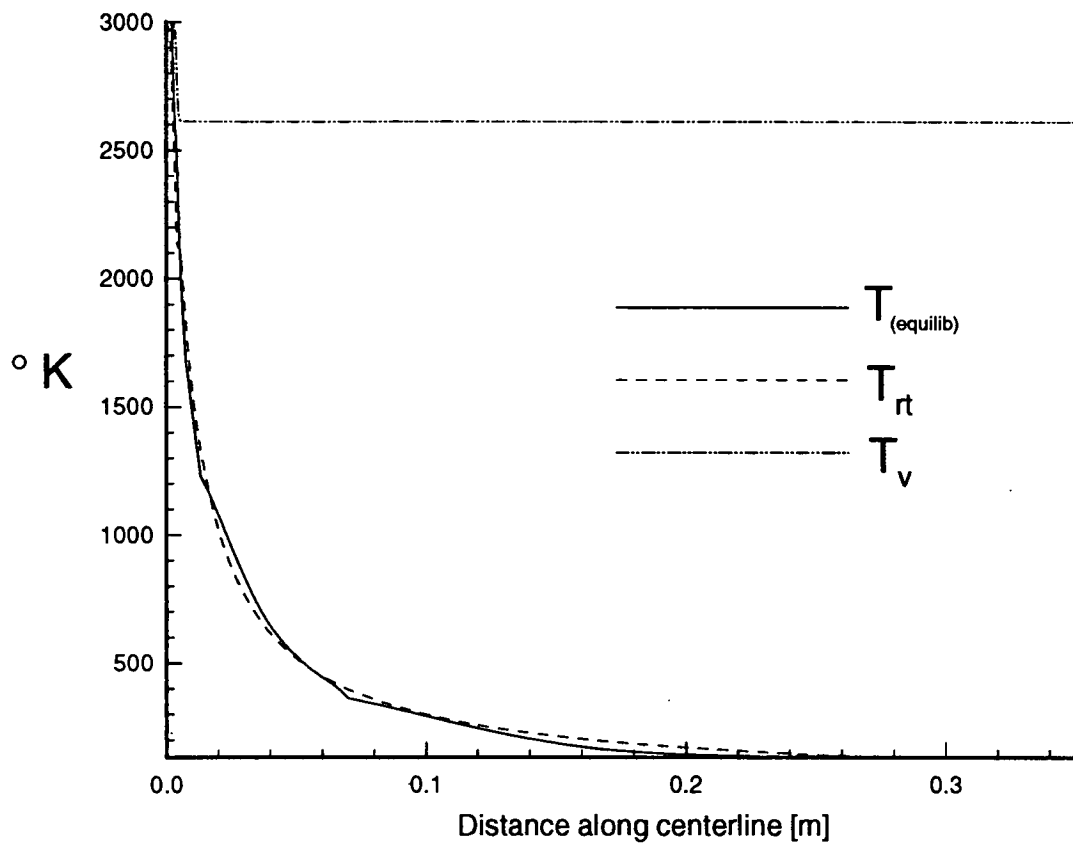


Figure 4.28. Centerline Equilibrium and Nonequilibrium Temperatures.

CHAPTER 5

CONCLUSIONS

The modeling of nozzle flow is a complicated problem. A wide variety of possible conditions and assumptions lead to a variety of flow characteristics, which makes general comparisons and prediction less meaningful. However, for specific cases, computer simulations are cost-effective tools for nozzle and wind tunnel research.

The governing equations for fluid flow were derived for a gas in thermal nonequilibrium. The internal energy is split into the energy from the translational and rotational degrees of freedom and the energy from the vibrational degree of freedom. Each energy is assumed to be a function of a separate temperature. The two-dimensional viscous Navier-Stokes equations were modified to include two energy equations coupled by means of the relaxation time. The relaxation time was derived from a new expression which was more realistic for the low temperatures that are characteristic of high-expansion nozzles. The other thermal properties were defined to be physically realistic and a function of temperature.

The continuous system of nonlinear partial differential equations were replaced by difference equations and were solved over a discrete grid. The implicit MacCormack method and the Steger-Warming flux vector splitting method were

applied to the equations. A set of boundary conditions were used which were physically meaningful, and gave a unique solution.

To test the effects of vibrational nonequilibrium, the solution of low pressure nitrogen gas flow through the given nozzle was tested. A stagnation pressure of 50 psi and stagnation temperature of $3000\text{ }^\circ\text{K}$ defined the test case. Results were found using both methods. The results showed that uniform flow existed for all cases, except in the boundary layer region. The axial velocities increased from 6 m/s to approximately 2837 m/s. Translational-rotational temperatures fell from $3000\text{ }^\circ\text{K}$ to $112\text{ }^\circ\text{K}$, except in the boundary layer which saw a marked increase in temperature. This was due to the addition of the coupling term to the translational-rotational energy equation. Properly defining the vibrational temperature boundary conditions reduced the negative numerical results.

A low pressure nitrogen wind tunnel would be a viable research tool, as it should produce mainly uniform flow. Since turbulent behavior was restricted, the actual behavior, and the extent to which it disrupts the flow is still not known. Based upon the relatively small radial velocities and the predicted size of the boundary layer, it is doubtful that turbulence would have had a pronounced effect on the flow.

The translational-rotational temperature falls throughout the nozzle, especially after the throat. In the boundary layer, the translational-rotational temperature increased significantly. The surplus was due to the vibrational relaxation, which is more complete in the boundary layer. Proper boundary conditions must be used to insure that the temperature does not increase unrealistically. Also, some of the

surplus energy may be due to turbulence. Proper turbulence modeling may have accounted for some of the excess energy and limited the growth of this temperature.

In the diverging section of the nozzle, the gas was found to be in nonequilibrium. The vibrational temperature remains higher than the translational-rotational temperature. This means that the assumption of thermal equilibrium before the throat is incorrect.

Downstream of the throat, the vibrational temperature freezes. This 'frozen' behavior extends from the centerline to the boundary layer. In the boundary layer, the vibrational temperature decreases to the value of the translational-rotational temperature.

A point in question is the formulation of the vibrational model. It is somewhat questionable as to whether the thermal properties can be split into two components as easily as was done here. Also, one would expect that the equation of state would be a function of the two temperatures. Finally, a reasonable relationship between the two temperatures and a physically meaningful single temperature would be useful for comparison purposes. These questions are areas for further research.

BIBLIOGRAPHY

- [1] Pierce F.J., *Microscopic Thermodynamics*, International Textbook Company, 1968.
- [2] Gnoffo P.A., "Application of Program Laura to Thermochemical nonequilibrium Flow through a nozzle", *Hypersonic Flows for Reentry Problems*, Vol.2, Springer-Verlag, 1145-1158, 1991.
- [3] Canupp P., Candler G., Perkins J., Erikson W., "Analysis of Hypersonic Nozzles Including Vibrational Nonequilibrium and Intermolecular Force Effects", 30th Aerospace Sciences Meeting, AIAA 92-0330, January 1992.
- [4] Gökçen T., "Computation of Nonequilibrium Viscous Flows in Arc-Jet Wind Tunnel Nozzles", 32nd Aerospace Sciences Meeting, AIAA-94-0254, Jan. 1994.
- [5] Millikan R.C., White D.R., "Systematics of Vibrational Relaxation", *Journal of Chemical Physics*, Vol. 39, No. 12, 3209-3213, December 1963.
- [6] Meador W.E., Williams M.D., Miner G.A., "Scaling of Vibrational Relaxation in Nitrogen Gases", (Submitted for NASA Technical Report), March 1995.
- [7] Walters R.W., Cinnella P., Slack D., Halt D., "Characteristic-Based Algorithms for Flows in Thermochemical Nonequilibrium", *AIAA Journal*, Vol. 30, No. 5, 1304-1313, May 1992.
- [8] MacCormack R.W., "Current Status of Numerical Solutions of the Navier-Stokes Equations", AIAA 23rd Aerospace Sciences Meeting, AIAA-85-0032, Jan, 1985.

- [9] Steger J.L., Warming R.F., "Flux Vector Splitting of the Inviscid Gasdynamic Equations with Applications to Finite-Difference Methods", *Journal of Computational Physics* 40, 263-293, 1981.
- [10] Benedict R.P., *Fundamentals of Gas Dynamics*, John Wiley and Sons, Inc., 1983.
- [11] Kauzmann W., *Kinetic Theory of Gases*, W. A. Benjamin, Inc., 1966.
- [12] Hirschfield J.O., Curtis C.F., Bird R.B., *Molecular Theory of Gases and Solids*, John Wiley and Sons, 1954.
- [13] Shang, J.S., "An Assessment of Numerical Solutions of the Compressible Navier-Stokes Equations", AIAA 17th Fluid Dynamics, Plasma Dynamics and Lasers Conference, AIAA 84-1549, June 1984.
- [14] Hoffman K.A., Chang S.T., *Computational Fluid Dynamics for Engineers*, Vol 1. and Vol. 2, Engineering Education System, Wichita, Kansas, 1993.
- [15] Thomas P.D., "Boundary Conditions for Implicit Solutions to the Compressible Navier-Stokes Equations in Finite Computational Domains", AIAA Computational Fluid Dynamics Conference, AIAA 79-1447, July, 1979, Williamsburg, Va.
- [16] Anderson D.A., Tannehill J.C., Pletcher R.H., *Computational Fluid Mechanics and Heat Transfer*, Hemisphere Publishing Co., 1984.

- [17] Beam R.M., Warming R.F., "An Implicit Factored Scheme for the Compressible Navier-Stokes Equations", *AIAA Journal*, Vol. 16, No. 4, 393-402, April 1978.
- [18] Bird G.A., "Direct Simulation of Gas Flows at the Molecular Level", *Communications in Applied Numerical Methods*, Vol. 4, 165-172, 1988.
- [19] Stewartson K., *The Theory of Laminar Boundary Layer in Computational Fluids*, Oxford, 1964.
- [20] Korte J.J., Hedlund E., Anandakrishnan S., "A comparison of Experimental data with CFD for the NSWC Hypervelocity Wind Tunnel #9 Mach 14 Nozzle", *AIAA 17th Aerospace Ground Testing Conference*, AIAA-92-4010, July 1992.
- [21] Heinbockel J.H., Landry J.G., "Nozzle Flow with Vibrational Nonequilibrium", *Final Report, NASA Research Grant NAG-1-1424*, August 1995.
- [22] Hassan B., Candler G., Olynick D., "Thermo-Chemical Nonequilibrium Effects on the Aerothermodynamics of Aerobraking Vehicles", *Journal of Spacecraft and Rockets*, Vol. 30, No. 6, 647-655, November-December 1993.

APPENDIX A

LIST OF SYMBOLS

a	Speed of Sound	[m/s]
A	Cross sectional area	[m^2]
b	Nozzle length	[m]
C	Characteristic length	[m]
C_v, C_{vrt}, C_{vv}	Specific heat at constant volume	[$J/Kg K$]
D	Diffusion constant	
$\frac{D}{Dt} = \frac{\partial}{\partial t} + \vec{V} \cdot \nabla$	Material or substantial derivative	
e, e_{rt}, e_v	Energy per unit mass	[J/Kg]
f	function: radius of nozzle	[m]
h	Planck's constant	[$J s$]
h	Enthalpy	[$J/m^3 s$]
$h1, h2, k1, k2$	Irregular grid spacings	
k	Boltzmann's constant	[J/K]
K, K_{rt}, K_v	Thermal conductivities	[$W/m K$]
K_n	Knudsen number	
L, δ	Scaling lengths	[m]

m	Number of grid points in axial direction
M	Mach number
n	Number of grid points in radial direction
N_i	Population densities [$1/m^3$]
$\vec{q}, \vec{q}_{rt}, \vec{q}_v$	Heat input per unit volume [$J/m^3 s$]
P	Pressure [N/m^2]
Pr	Prandtl number
R	Gas Constant [$J/Kg K$]
Re	Reynolds number
r, z	Physical coordinates
s	Entropy per unit volume [$J/m^3 s K$]
Sc	Schmidt number
t	Time [s]
T, T_{rt}, T_v	Temperatures [K]
\vec{V}	Velocity [m/s]
V_r, V_θ, V_z	Velocity components [m/s]
W	Molecular weight of N_2 [Kg]
X	Coupling term [K/s]
x, y	Computational coordinates

η	Viscosity coefficient	$[Kg/m\ s]$
λ	Second coefficient of viscosity	$[Kg/m\ s]$
λ_{max}	Maximum mean free path	$[m]$
ρ	Density	$[Kg/m^3]$
τ	Relaxation time	$[s]$
δ_{bl}	Boundary layer width	$[m]$
Δ_x, Δ_y	Forward difference operators	
∇_x, ∇_y	Backward difference operators	
ϵ_i	Energy states	$[J]$
σ_{ij}	Stress tensor	$[N/m^2]$
τ_{ij}	Shear stress tensor	$[N/m^2]$
ϕ, θ, ξ	Characteristic temperatures	$[K]$
Φ	Viscous dissipation function	$[N/m^2\ s]$
ν	Frequency	$[s^{-1}]$
$\gamma = \frac{C_p}{C_v}$	Ratio of specific heats	

APPENDIX B

NOZZLE DESIGN

The nozzle used in this study had a length, b , of 350 millimeters. The domain used in the simulations was the top half the a cross-section of the nozzle cut by the plane $\theta = 0$, see figure B1. The equation representing the nozzle shape was actually four separate equations which represent a section of the nozzle. Starting from $z = 0$, the sections are described by a straight line, a circle, a cubic spline, and another straight line. The location of the divisions are the points a_1 , a_2 , and a_3 [figure B1].

The equation of the nozzle is the equation of the radius, r , in meters, which is a function of the axial distance z , in millimeters. The equations for each section are as follows:

$$0 \leq z \leq a_1, \quad r = f(z) = 10^{-3} * (m_1 * (z - a_2) - a_0 + R - 3 - \sqrt{R^2 - 3})$$

$$a_1 \leq z \leq a_2, \quad r = f(z) = 10^{-3} * (a_0 + R - \sqrt{R^2 - (z - a_2)^2})$$

$$a_2 \leq z \leq a_3, \quad r = f(z) = 10^{-3} * \left(\frac{-(z - a_2)^3}{12R^2m_2} + \frac{(z - a_2)^2}{2R} + a_0 \right)$$

$$a_3 \leq z \leq b, \quad r = f(z) = 10^{-3} * (a_4 + m_2 * (z - a_3))$$

where

$$m_1 = -\tan 60^\circ$$

$$m_2 = \tan \theta \quad a_1 = \frac{5 - a_0 - R + \sqrt{R^2 - 3}}{\sqrt{3}}$$

$$\theta = 4^\circ \quad a_2 = a_1 + \sqrt{3}R/2$$

$$a_0 = 0.5 \text{ mm} \quad a_3 = a_2 + 2Rm_2$$

$$R = 2.0 \text{ mm} \quad a_4 = a_0 + \frac{4Rm_2^2}{3}$$

$$r_0 = 5.0 \text{ mm.}$$

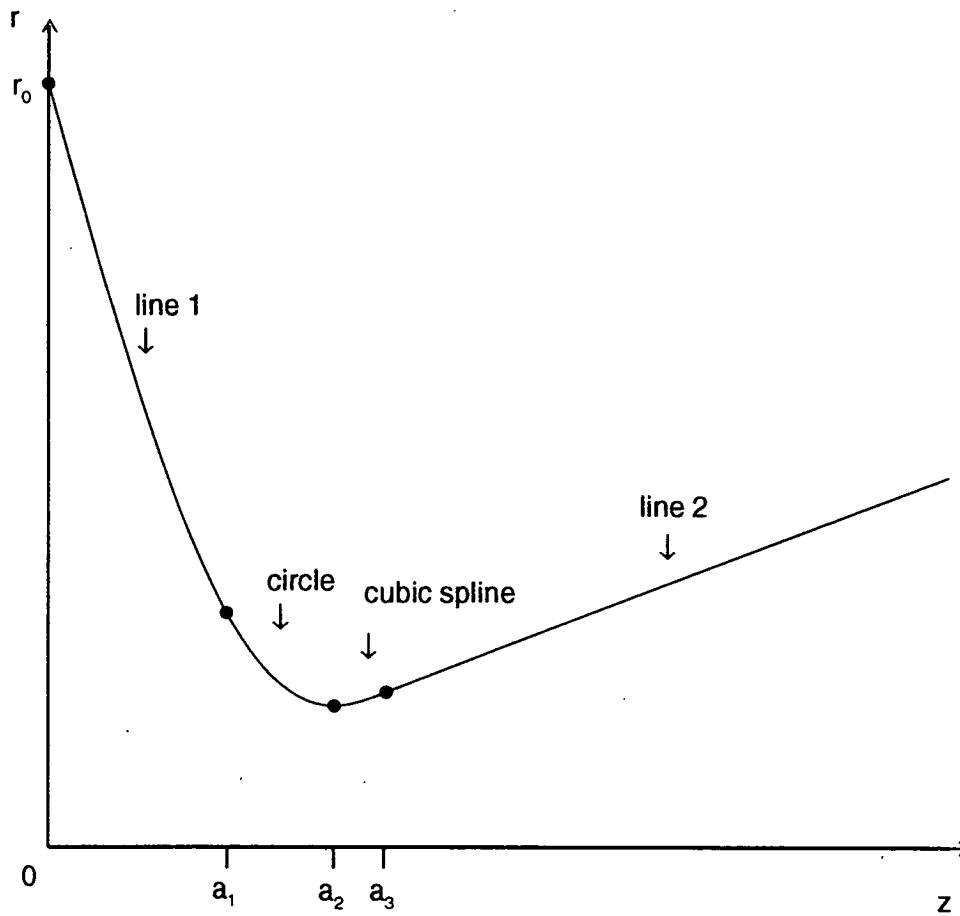


Figure B1. Nozzle Design

AUTOBIOGRAPHICAL STATEMENT

1. Date of Birth

[REDACTED]

2. Place of Birth

[REDACTED]

3. Education

Bachelor of Science, Chemistry: Lawrence Institute of Technology, 1988.

Bachelor of Science, Math and Computer Science:

Lawrence Technological University, 1989.

Master of Arts, Mathematics: University of Detroit, 1991.